

# Safety Reports Series

## No. 85

### Ground Motion Simulation Based on Fault Rupture Modelling for Seismic Hazard Assessment in Site Evaluation for Nuclear Installations

# IAEA SAFETY STANDARDS AND RELATED PUBLICATIONS

## IAEA SAFETY STANDARDS

Under the terms of Article III of its Statute, the IAEA is authorized to establish or adopt standards of safety for protection of health and minimization of danger to life and property, and to provide for the application of these standards.

The publications by means of which the IAEA establishes standards are issued in the **IAEA Safety Standards Series**. This series covers nuclear safety, radiation safety, transport safety and waste safety. The publication categories in the series are **Safety Fundamentals**, **Safety Requirements** and **Safety Guides**.

Information on the IAEA's safety standards programme is available on the IAEA Internet site

<http://www-ns.iaea.org/standards/>

The site provides the texts in English of published and draft safety standards. The texts of safety standards issued in Arabic, Chinese, French, Russian and Spanish, the IAEA Safety Glossary and a status report for safety standards under development are also available. For further information, please contact the IAEA at: Vienna International Centre, PO Box 100, 1400 Vienna, Austria.

All users of IAEA safety standards are invited to inform the IAEA of experience in their use (e.g. as a basis for national regulations, for safety reviews and for training courses) for the purpose of ensuring that they continue to meet users' needs. Information may be provided via the IAEA Internet site or by post, as above, or by email to [Official.Mail@iaea.org](mailto:Official.Mail@iaea.org).

## RELATED PUBLICATIONS

The IAEA provides for the application of the standards and, under the terms of Articles III and VIII.C of its Statute, makes available and fosters the exchange of information relating to peaceful nuclear activities and serves as an intermediary among its Member States for this purpose.

Reports on safety in nuclear activities are issued as **Safety Reports**, which provide practical examples and detailed methods that can be used in support of the safety standards.

Other safety related IAEA publications are issued as **Emergency Preparedness and Response** publications, **Radiological Assessment Reports**, the International Nuclear Safety Group's **INSAG Reports**, **Technical Reports** and **TECDOCs**. The IAEA also issues reports on radiological accidents, training manuals and practical manuals, and other special safety related publications.

Security related publications are issued in the **IAEA Nuclear Security Series**.

The **IAEA Nuclear Energy Series** comprises informational publications to encourage and assist research on, and the development and practical application of, nuclear energy for peaceful purposes. It includes reports and guides on the status of and advances in technology, and on experience, good practices and practical examples in the areas of nuclear power, the nuclear fuel cycle, radioactive waste management and decommissioning.

GROUND MOTION SIMULATION  
BASED ON FAULT RUPTURE  
MODELLING FOR  
SEISMIC HAZARD ASSESSMENT  
IN SITE EVALUATION  
FOR NUCLEAR INSTALLATIONS

The following States are Members of the International Atomic Energy Agency:

AFGHANISTAN	GERMANY	PAKISTAN
ALBANIA	GHANA	PALAU
ALGERIA	GREECE	PANAMA
ANGOLA	GUATEMALA	PAPUA NEW GUINEA
ANTIGUA AND BARBUDA	GUYANA	PARAGUAY
ARGENTINA	HAITI	PERU
ARMENIA	HOLY SEE	PHILIPPINES
AUSTRALIA	HONDURAS	POLAND
AUSTRIA	HUNGARY	PORTUGAL
AZERBAIJAN	ICELAND	QATAR
BAHAMAS	INDIA	REPUBLIC OF MOLDOVA
BAHRAIN	INDONESIA	ROMANIA
BANGLADESH	IRAN, ISLAMIC REPUBLIC OF	RUSSIAN FEDERATION
BELARUS	IRAQ	RWANDA
BELGIUM	IRELAND	SAN MARINO
BELIZE	ISRAEL	SAUDI ARABIA
BENIN	ITALY	SENEGAL
BOLIVIA, PLURINATIONAL STATE OF	JAMAICA	SERBIA
BOSNIA AND HERZEGOVINA	JAPAN	SEYCHELLES
BOTSWANA	JORDAN	SIERRA LEONE
BRAZIL	KAZAKHSTAN	SINGAPORE
BRUNEI DARUSSALAM	KENYA	SLOVAKIA
BULGARIA	KOREA, REPUBLIC OF	SLOVENIA
BURKINA FASO	KUWAIT	SOUTH AFRICA
BURUNDI	KYRGYZSTAN	SPAIN
CAMBODIA	LAO PEOPLE'S DEMOCRATIC REPUBLIC	SRI LANKA
CAMEROON	LATVIA	SUDAN
CANADA	LEBANON	SWAZILAND
CENTRAL AFRICAN REPUBLIC	LESOTHO	SWEDEN
CHAD	LIBERIA	SWITZERLAND
CHILE	LIBYA	SYRIAN ARAB REPUBLIC
CHINA	LIECHTENSTEIN	TAJIKISTAN
COLOMBIA	LITHUANIA	THAILAND
CONGO	LUXEMBOURG	THE FORMER YUGOSLAV REPUBLIC OF MACEDONIA
COSTA RICA	MADAGASCAR	TOGO
CÔTE D'IVOIRE	MALAWI	TRINIDAD AND TOBAGO
CROATIA	MALAYSIA	TUNISIA
CUBA	MALI	TURKEY
CYPRUS	MARSHALL ISLANDS	UGANDA
CZECH REPUBLIC	MAURITANIA	UKRAINE
DEMOCRATIC REPUBLIC OF THE CONGO	MAURITIUS	UNITED ARAB EMIRATES
DENMARK	MEXICO	UNITED KINGDOM OF GREAT BRITAIN AND NORTHERN IRELAND
DJIBOUTI	MONACO	UNITED REPUBLIC OF TANZANIA
DOMINICA	MONGOLIA	UNITED STATES OF AMERICA
DOMINICAN REPUBLIC	MONTENEGRON	URUGUAY
ECUADOR	MOROCCO	UZBEKISTAN
EGYPT	MOZAMBIQUE	VANUATU
EL SALVADOR	MYANMAR	VENEZUELA, BOLIVARIAN REPUBLIC OF
ERITREA	NAMIBIA	VIET NAM
ESTONIA	NEPAL	YEMEN
ETHIOPIA	NETHERLANDS	ZAMBIA
FIJI	NEW ZEALAND	ZIMBABWE
FINLAND	NICARAGUA	
FRANCE	NIGER	
GABON	NIGERIA	
GEORGIA	NORWAY	
	OMAN	

The Agency's Statute was approved on 23 October 1956 by the Conference on the Statute of the IAEA held at United Nations Headquarters, New York; it entered into force on 29 July 1957. The Headquarters of the Agency are situated in Vienna. Its principal objective is "to accelerate and enlarge the contribution of atomic energy to peace, health and prosperity throughout the world".

IAEA SAFETY REPORTS SERIES No. 85

GROUND MOTION SIMULATION  
BASED ON FAULT RUPTURE  
MODELLING FOR  
SEISMIC HAZARD ASSESSMENT  
IN SITE EVALUATION  
FOR NUCLEAR INSTALLATIONS

INTERNATIONAL ATOMIC ENERGY AGENCY  
VIENNA, 2015

## COPYRIGHT NOTICE

All IAEA scientific and technical publications are protected by the terms of the Universal Copyright Convention as adopted in 1952 (Berne) and as revised in 1972 (Paris). The copyright has since been extended by the World Intellectual Property Organization (Geneva) to include electronic and virtual intellectual property. Permission to use whole or parts of texts contained in IAEA publications in printed or electronic form must be obtained and is usually subject to royalty agreements. Proposals for non-commercial reproductions and translations are welcomed and considered on a case-by-case basis. Enquiries should be addressed to the IAEA Publishing Section at:

Marketing and Sales Unit, Publishing Section  
International Atomic Energy Agency  
Vienna International Centre  
PO Box 100  
1400 Vienna, Austria  
fax: +43 1 2600 29302  
tel.: +43 1 2600 22417  
email: sales.publications@iaea.org  
<http://www.iaea.org/books>

© IAEA, 2015

Printed by the IAEA in Austria  
November 2015  
STI/PUB/1689

### IAEA Library Cataloguing in Publication Data

Ground motion simulation based on fault rupture modelling for seismic hazard assessment in site evaluation for nuclear installations. — Vienna : International Atomic Energy Agency, 2015.

p. ; 24 cm. — (Safety reports series, ISSN 1020-6450 ; no. 85)

STI/PUB/1689

ISBN 978-92-0-102315-5

Includes bibliographical references.

1. Nuclear facilities — Safety measures. 2. Nuclear facilities — Location.
3. Earthquake hazard analysis. 4. Earthquake simulators. 5. Earthquake prediction.
- I. International Atomic Energy Agency. II. Series.

IAEAL

15-01000

## **FOREWORD**

IAEA Safety Standards Series No. SSG-9, Seismic Hazards in Site Evaluation for Nuclear Installations, issued in 2010, covers all aspects relating to seismic hazards. One of major revisions in SSG-9 is a recommendation to use fault rupture modelling for ground motion simulation in cases where nearby faults contribute significantly to the seismic hazard for nuclear installations. The overall process of the methodology is described in SSG-9; however, more detailed guidance was desired by Member States.

At a donors meeting of the International Seismic Safety Centre's Extrabudgetary Programme (ISSC-EBP) in January 2011, it was decided to develop detailed guidelines under the project on seismic hazards. Two months after this decision, the Great East Japan Earthquake and Tsunami of 11 March 2011 occurred. The fault length and width of slip were more than 400 km and 200 km, respectively. Hence, the point source assumption at the hypocentre was not applicable. Ground motion estimation is the key issue in the seismic hazard, and is estimated with empirical ground motion prediction equations (GMPEs). The GMPEs were determined by the statistical analysis of observed records; therefore, they are reliable in the area where many observations were recorded. However, in the area closest to the rupture fault, the records were quite rare, and the rupture process of the fault strongly influences the characteristics of the ground motion. The ground motion simulation based on fault rupture modelling is therefore more appropriate than using GMPEs in the short distance from the fault rupture.

The purpose of this publication is to provide the state of the art and current practices of ground motion simulation based on fault rupture modelling, in order to support Member States in implementing the provisions of SSG-9 in seismic hazard assessment and reassessment for nuclear installations.

The detailed guidelines and practical tools presented here will be of value to researchers, operating organizations, regulatory bodies, vendors and technical support organizations in the areas of seismic hazard evaluation of nuclear installations. The information will be of great importance in support of post Fukushima hazard assessments.

The contributions of all those who were involved in the drafting and review of this publication are greatly appreciated. K. Irikura (Japan) is acknowledged for his leadership in the project and C.J. Wu (Japan) for his leadership in the development of this publication. The IAEA officer responsible for this publication was Y. Fukushima of the Division of Nuclear Installation Safety.

## *EDITORIAL NOTE*

*Although great care has been taken to maintain the accuracy of information contained in this publication, neither the IAEA nor its Member States assume any responsibility for consequences which may arise from its use.*

*This publication does not address questions of responsibility, legal or otherwise, for acts or omissions on the part of any person.*

*Guidance provided here, describing good practices, represents expert opinion but does not constitute recommendations made on the basis of a consensus of Member States.*

*The use of particular designations of countries or territories does not imply any judgement by the publisher, the IAEA, as to the legal status of such countries or territories, of their authorities and institutions or of the delimitation of their boundaries.*

*The mention of names of specific companies or products (whether or not indicated as registered) does not imply any intention to infringe proprietary rights, nor should it be construed as an endorsement or recommendation on the part of the IAEA.*

*The IAEA has no responsibility for the persistence or accuracy of URLs for external or third party Internet web sites referred to in this publication and does not guarantee that any content on such web sites is, or will remain, accurate or appropriate.*

## CONTENTS

1. INTRODUCTION .....	1
1.1. Background .....	1
1.2. Objective .....	2
1.3. Scope .....	3
1.4. Structure .....	3
2. DEFINITIONS AND TERMINOLOGY .....	3
2.1. Earthquake categories .....	3
2.2. Identified fault .....	4
2.3. Fault rupture modelling .....	4
3. CHARACTERISTICS AND EVALUATION METHODS OF GROUND MOTIONS .....	4
3.1. Physical process affecting strong ground motion hazard assessment .....	5
3.1.1. Summary of concepts used in strong ground motion simulation methods .....	7
3.1.2. Use of the elastodynamic representation theorem .....	9
3.1.3. Earthquake source rupture processes .....	11
3.1.4. Seismic wave propagation processes .....	16
3.2. Overview of strong motion simulation procedures .....	17
3.2.1. Stochastic method .....	18
3.2.2. Asperity source model .....	20
3.2.3. Hybrid source model .....	26
3.2.4. Composite source model .....	31
3.3. Validation of simulated ground motions .....	33
3.4. Features of near source ground motions: Rupture directivity and fling step .....	36
3.4.1. Introduction .....	36
3.4.2. Orientation of dynamic and static near fault ground motions .....	37
3.4.3. Different strike normal and strike parallel components of horizontal dynamic motions .....	39
3.4.4. Incidence of the rupture directivity pulse .....	39
3.4.5. Duration of near fault time histories .....	40

3.4.6. Response spectrum for design and analysis . . . . .	40
3.4.7. Selection of near fault time histories for design and analysis . . . . .	40
3.4.8. Scaling and matching of near fault time histories . . . . .	41
3.4.9. Orientation of components . . . . .	42
<b>4. EXAMPLES OF GROUND MOTION EVALUATION BASED ON HETEROGENEOUS SOURCE MODELS . . . . .</b>	<b>42</b>
4.1. Examples of predicted ground motions based on the SMGA/asperity model . . . . .	42
4.1.1. Crustal earthquake . . . . .	42
4.1.2. Subduction interface earthquake . . . . .	44
4.1.3. Intra-slab earthquake . . . . .	47
4.2. Examples of ground motion evaluation based on the hybrid method . . . . .	49
4.3. Uncertainty in ground motion prediction using fault rupture modelling . . . . .	54
4.4. Examples of uncertainty treatment . . . . .	57
<b>5. CONCLUSIONS . . . . .</b>	<b>59</b>
5.1. Advantages and disadvantages of different approaches . . . . .	59
5.2. Roles of ground motion simulations and GMPEs . . . . .	60
<b>APPENDIX I: ESTIMATION OF FAULT PARAMETERS FOR THE SMGA/ASPERITY MODEL . . . . .</b>	<b>61</b>
<b>APPENDIX II: OPEN ACCESS TO THE SCEC BROADBAND SIMULATION PLATFORM . . . . .</b>	<b>79</b>
<b>REFERENCES . . . . .</b>	<b>81</b>
<b>ANNEX: FAULT DISPLACEMENT HAZARD ANALYSIS . . . . .</b>	<b>93</b>
<b>CONTRIBUTORS TO DRAFTING AND REVIEW . . . . .</b>	<b>125</b>

# 1. INTRODUCTION

## 1.1. BACKGROUND

This Safety Report has been developed as a part of the work undertaken in the International Seismic Safety Centre's Extrabudgetary Programme (ISSC-EBP). Work related to the seismic hazard is addressed as Working Area 1 (WA1) in the ISSC-EBP. The objective of WA1 is to develop guidelines to implement the recommendations of IAEA Safety Standards Series No. SSG-9, Seismic Hazards in Site Evaluation for Nuclear Installations [1]. One of major recommendations made in the revision of SSG-9 [1] is to use fault modelling for seismically active regions. The overall process of fault rupture modelling and ground motion simulation is described in para. 5.14 of SSG-9 [1]. However, more detailed guidance has been desired by the Member States. As such, under WA1, Working Group 1.2 was created to prepare a document on fault rupture modelling to address this need.

In seismic hazard assessments, it is necessary to obtain accurate estimates of the response spectrum and broadband ground motion time histories in the period range of 0.01–10 seconds. Methodologies for assessing ground motions consist of two basic approaches. The first consists of ground motion prediction equations (GMPEs); the second consists of physics based methods for strong ground motion simulation. A GMPE is an equation used to estimate the amplitude of ground motion (usually response spectral amplitude at several periods) from a set of predictor variables (e.g. magnitude, distance and site condition). Most GMPEs are derived from recorded strong ground motions. However, when strong motion recordings are not available, strong motion simulations may be used instead. GMPEs primarily provide ground motion response spectra. Corresponding ground motion time history representations can be obtained from the time histories used to generate the GMPE. Conversely, ground motion time histories are directly provided by the physics based simulations, and these time histories can be used to develop simulation based GMPEs that provide response spectra.

In many regions, especially those with low levels of seismicity, the number of strong ground recordings is not large enough to develop GMPEs based on recorded data. For such regions, such as eastern North America and Australia, GMPEs from other regions have to be adopted and adjusted, or GMPEs can be developed based on strong ground motion simulations using fault rupture and wave propagation modelling.

Recorded ground motions are often too sparse to adequately constrain GMPEs for high magnitudes at short distances that may influence the seismic hazard assessment at nuclear installations. For example, there is only one strong motion record of a magnitude 8 strike-slip earthquake, at a closest distance of less than 10 km (the Pump Station 10 recording of the  $M_W$  7.9 Denali, Alaska, earthquake of 2002). Strong motion simulations can be used to extrapolate GMPEs based on strong motion recordings to closer distances and larger magnitudes than those that are well represented in strong motion databases.

Moreover, specific conditions related to the source geometry (e.g. asperity location, rupture directivity and hanging wall effects) and crustal structure (e.g. 3-D basin effects) can have an influence on the resulting ground motions that is quite strong and difficult to adequately represent using GMPEs based on strong motion recordings because those recordings may not contain the known site specific source and path conditions relevant to the site.

For example, the  $M_W$  7.0 Kobe, Japan, earthquake of 1995 generated strong directivity pulses, amplified by basin edge effects, which caused severe damage to structures in the city of Kobe. This disaster emphasized the need to simulate the time histories by fault rupture modelling for earthquake resistant design of nuclear installations. The need to develop guidelines for fault rupture modelling was also demonstrated by the  $M_W$  9.0 Tohoku, Japan, earthquake of 2011. In the period range of importance to nuclear installations, most of the strong ground motion from this earthquake was generated in several patches on the deep part of the plate interface. In order to estimate the strong ground motions from future  $M_W$  9 earthquakes, it is necessary to understand whether or not this pattern is typical of such earthquakes, and to assess the variability in ground motions that would be generated by alternative source models. Since such large earthquakes occur infrequently, strong motion simulations as well as the 2010 Maule and 2011 Tohoku recordings are required to develop reliable GMPEs for such events.

## 1.2. OBJECTIVE

This Safety Report provides guidance on ground motion simulation using fault rupture modelling for seismic hazard assessment in site evaluation for nuclear installations. It describes the ground motion simulation methods and their application to estimating ground motions and ground displacement near faults.

### **1.3. SCOPE**

The scope of this Safety Report includes relevant definitions and terminology, characteristics and evaluation methods of ground motions, evaluation of fault parameters for heterogeneous source models, and state of the art practices in ground motion simulation based on heterogeneous source models, in order to improve seismic hazard assessment.

### **1.4. STRUCTURE**

Section 2 presents the definitions and terminology used in this Safety Report. Section 3 introduces characteristics and evaluation methods of ground motions. Section 4 shows some examples of ground motion evaluation based on the heterogeneous source models. Section 5 concludes the fault rupture modelling described in this Safety Report.

The practice of evaluation of fault parameters is introduced in Appendix I for the ground motion simulation based on heterogeneous models. In addition, the open access to the platform of the Southern California Earthquake Center (SCEC) is introduced in Appendix II for several strong motion simulation methods. Some state of the art fault displacement hazard analyses are introduced in the Annex.

## **2. DEFINITIONS AND TERMINOLOGY**

### **2.1. EARTHQUAKE CATEGORIES**

Earthquakes are classified into three categories in this Safety Report: crustal, subduction interface and intra-slab. Crustal earthquakes consist of two types of earthquake: one that occurs in stable continental regions and one that occurs on, or near, plate boundaries between two plates. Subduction interface earthquakes occur in active crustal regions on the plate boundaries between continental plates and subducting oceanic plates. Intra-slab earthquakes occur within subducting oceanic plates, called slabs. The intra-slab earthquakes consist of deep earthquakes that usually occur near or landward of the coastline and shallow earthquakes that occur offshore in the outerrise.

## 2.2. IDENTIFIED FAULT

An identified fault is defined as one for which the parameters listed in para. 5.14(a) of SSG-9 [1] can be estimated. Paragraph 5.14(a) of SSG-9 [1] recommends that fault rupture simulation be done for nearby identified faults, especially where they contribute significantly to the hazard.

## 2.3. FAULT RUPTURE MODELLING

Fault rupture modelling involves earthquake rupture parameterization that include, for example:

- Fault length;
- Fault width;
- Slip distribution on the fault;
- Slip time function on the fault;
- Rupture initiation point;
- Rupture propagation mode;
- Rupture propagation velocity.

Fault rupture modelling is used to generate the ground motions and ground displacement near the fault caused by the earthquake. The parameters used in fault rupture modelling are estimated using observed data, empirical relations between parameters and theoretical relations between parameters. The uncertainty in some of these parameters can be quite large, and they need to be dealt with using systematic uncertainty analyses.

## 3. CHARACTERISTICS AND EVALUATION METHODS OF GROUND MOTIONS

This section describes the current techniques that are being used in fault rupture modelling and ground motion simulation, and applied to nuclear installations.

### 3.1. PHYSICAL PROCESS AFFECTING STRONG GROUND MOTION HAZARD ASSESSMENT

Strong motion simulations are based on a rigorous mathematical representation of the earthquake source and seismic wave propagation between the source and the site. Three processes involved in the generation of earthquake ground motion are shown schematically in Fig. 1 [2]. Seismic waves are generated as part of the strain energy released from the rupturing of a fault (earthquake source process). The seismic waves then propagate through the Earth's crust and the mantle (wave propagation or path effect) and approach the surface of the Earth, where they undergo further modifications while propagating through shallow soils (shallow soil response). These processes representing source, wave path, and local site effects are often difficult to be separated.

GMPEs use a simplified model of ground motion generation process in which the effects of the earthquake source are represented primarily by the earthquake magnitude. The effects of wave propagation from the earthquake source to the site are represented primarily by fault distance, although the behaviour of the crustal waveguide and effect of regional attenuation (material damping factor,  $Q$ ) is implicit in the coefficients that are estimated from the recorded time histories. The site effects are specified by a site parameter or category (see Fig. 1), although average near-surface attenuation ( $\kappa_0$ ) may be incorporated to the extent that it influences the empirical coefficients. GMPEs that also include geometrical effects such as rupture directivity and hanging wall effects, as well as basin effects, have been developed [3].

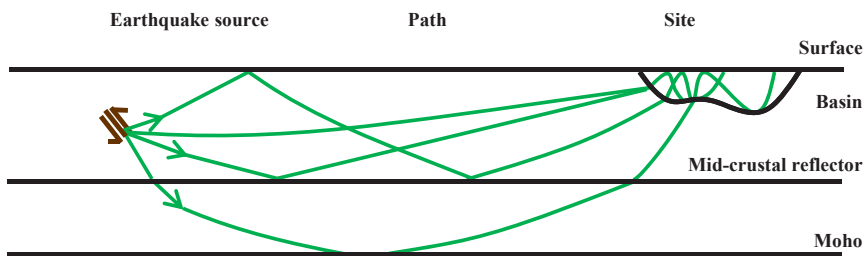


FIG. 1. Schematic diagram of empirical and seismological models of earthquake ground motions (adapted from Ref. [2] with permission).

The GMPE method has been developed by many researchers [4–10]. At low probability levels, applicable to nuclear power plants, the earthquake shaking hazard in many regions of the world is associated with larger earthquake magnitudes and shorter distances than those available in strong ground motion databases. This is particularly true in tectonically stable regions, where strong motion recordings are much too sparse to provide a basis for developing reliable GMPEs, and therefore have to be adopted and adjusted from other regions or developed based on simulations.

As shown in Fig. 1 [11]:

“...the earthquake source is a complex rupture process on a fault. Seismic waves arrive at the site by propagation through a complex waveguide, and complex local geology can have an important influence on the recorded ground motions. Strong motion simulation methods have the advantage of allowing the incorporation of information about earthquake source, seismic wave propagation, and local site characteristics that are specific to the region and to the site in question. These characteristics may include rupture directivity effects, hanging wall/foot wall effects, Moho bounce effects, basin effects, and site effects.”

Consequently, if all parameters are known in sufficient detail, the use of these models to extrapolate low probability events is believed to have the potential to generate more accurate representations of the ground motions than using GMPEs. According to Ref. [11]:

“This is contingent upon the use of simulation methods that have the capability to accurately reproduce the characteristics of recorded ground motions in cases where the earthquake source and seismic velocity structure (and hence wave propagation characteristics) are well known, and upon the availability of reliable information about earthquake source and crustal structure characteristics in the site region.”

It is important to recognize uncertainties in the ability of both GMPEs and physics based simulations to extrapolate to all the situations of interest. As explained in Ref. [11]:

“Even in tectonically active regions of the United States, the ground motions that dominate seismic design are from larger earthquake magnitudes than are abundant in the strong motion database. The Pump Station 10 recording of the 2000 Denali, Alaska earthquake is still the only near-fault recording of a magnitude 8 strike-slip earthquake anywhere

in the world, yet the seismic hazard in many urban regions in California is dominated by such events. For regions where the hazard is dominated by thrust earthquakes having magnitudes as large as 7.5, the database consists mainly of recordings from overseas earthquakes such as the 1999 magnitude 7.6 Chi-Chi, Taiwan event, which was associated with large surface faulting with weak short period ground motions and weak rupture directivity effects. These recordings may not provide an optimal representation of events such as a blind thrust earthquake on the Puente Hills Blind Thrust beneath downtown Los Angeles, with its potential for much stronger short-period ground motions and rupture directivity effects.”

To the extent that these are the only earthquakes on which source models used in simulations can be calibrated, they may be biased if they are not representatives of ‘typical’ earthquakes. However, source models for large earthquakes are to some extent constrained by teleseismic observations, so the uncertainties in physics based methods of generating strong motion synthetics are probably smaller than the uncertainties in extrapolation using GMPEs. This is a strong reason for favouring these methods over GMPEs in these situations.

The focus of this section is on ground motion simulation methods that simulate earthquake source rupture and seismic wave propagation processes and estimate the resulting ground motions at a rock site. Other aspects of ground motion simulation that are not treated in detail here include: the simulation of local wave propagation through the soil and rock sediments at a site to estimate the effects of the sediments on the site ground motions (these methods are usually referred to as site response analyses); and the simulation of wave propagation in two or three dimensional deep sedimentary basins in which a site may be located to estimate the basin response effects on site ground motions.

### **3.1.1. Summary of concepts used in strong ground motion simulation methods**

There is a large variety of ground motion simulation procedures, some of which are purely numerical and have little or no seismological basis. Procedures that use well founded seismological models are expected to produce more realistic ground motions than procedures that lack a seismological basis. For this reason, only well founded and well validated seismological procedures should be used in engineering applications.

Seismologists have studied and developed theoretical models to explain and model, either theoretically or statistically, the effects of the earthquake source and wave propagation on observed ground motions (see Refs [12–15]). These well accepted models have provided the seismological basis for ground motion

simulation procedures. A survey of existing simulation procedures (and their seismological basis) can be found in Ref. [16]. This section describes basic features of seismological models that are essential to a simulation procedure. The following discussions focus on features related to the processes of earthquake source and seismic wave propagation in the crust [17]:

“At long periods (longer than about 1 second), strong ground motions are deterministic in the sense that seismological models are capable of matching not only the spectral amplitudes but also the waveforms of recorded long period ground motions, once the rupture model of the earthquake and the seismic velocity structure of the region surrounding the earthquake are known. At short periods (shorter than about 1 second), strong ground motions become increasingly stochastic in nature. Seismological models are generally capable of matching the spectral amplitudes of the short period ground motions, but are generally not capable of matching the recorded waveforms.”

This is illustrated in the comparison between recorded and simulated ground motions of the 1997 Northridge earthquake recorded at Arleta shown in Fig. 2 [18]. The simulations generally provide a fairly good waveform match to the recorded velocity and displacement time histories in early phases and a poor match to the recorded acceleration time histories.

“The transition from deterministic to stochastic behavior appears to be due to a transition from coherent source radiation and wave propagation conditions at long periods (over long dimensions) to incoherent source radiation and wave propagation conditions at short periods (over short dimensions)” [17].

Source radiation and wave propagation become increasingly incoherent at short periods (see Refs [15, 19]) owing to the existence of small scale heterogeneities in the earthquake source process and crustal properties. Overall, the observed high frequency motions behave stochastically. The period of transition from deterministic to stochastic behaviour is uncertain, but is often taken as about  $T \approx 1$  s [20].

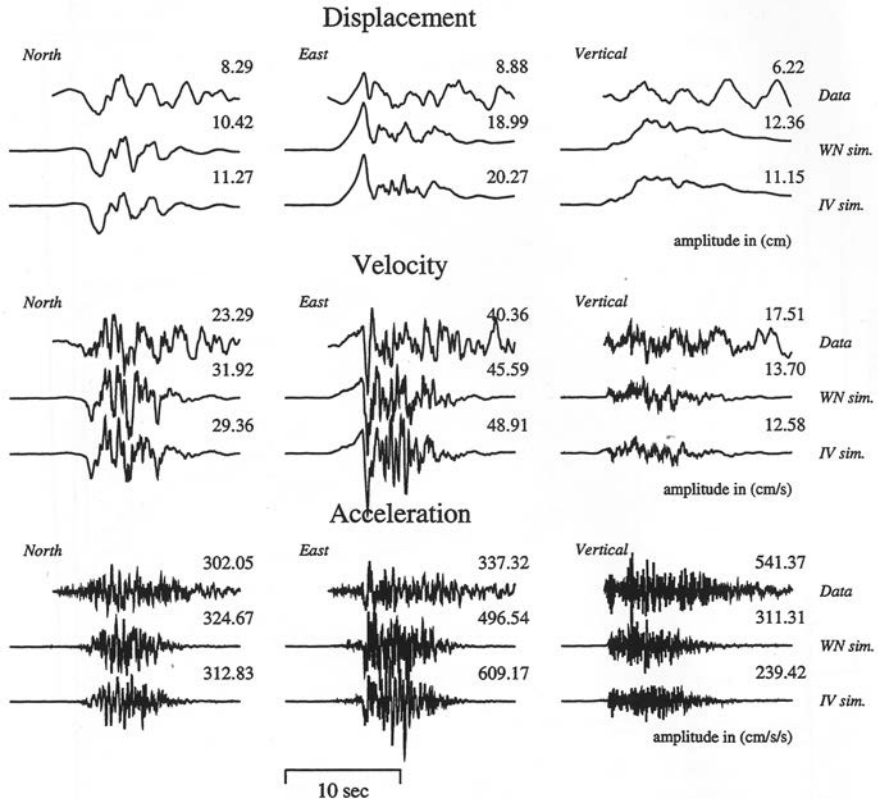


*FIG. 2. Comparison of recorded (top row) and simulated (middle and bottom rows) displacement, velocity and acceleration time histories at Arleta from the 1994 Northridge earthquake, plotted on a common scale, with the peak value given in the top right corner (reproduced from Ref. [18] with permission).*

### 3.1.2. Use of the elastodynamic representation theorem

The elastodynamic representation theorem is used to compute the total ground motion at a site from time functions of slip on the fault that represent faulting and Green's functions that represent seismic wave propagation. Comprehensive discussions of the representation theorem and its use in ground motion simulation are provided in Refs [12, 14, 20].

The representation theorem is a summation over time and a double summation over space on a 2-D grid of point sources on the fault plane (see Fig. 3). In the first summation, multiple time-lagged Green's functions for a given point on the fault are convolved with the time function of slip at that point on the fault. The time lag accounts for delays due to rupture propagation and the

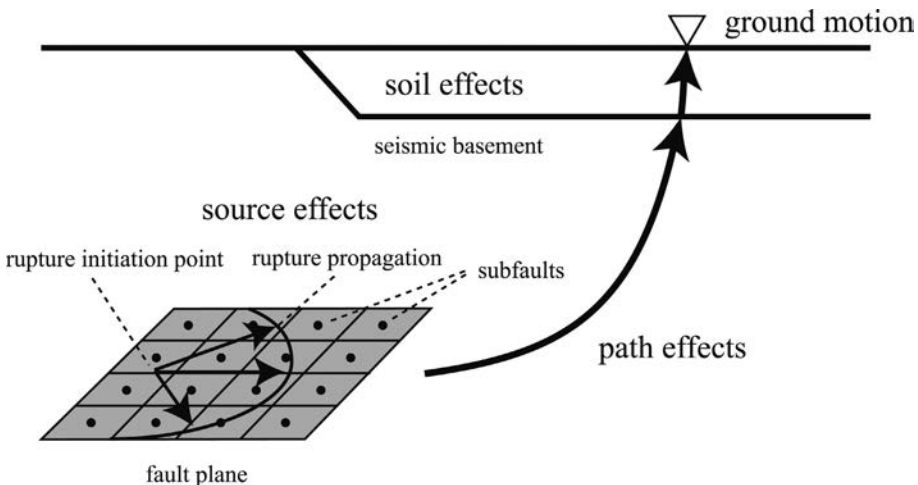


*FIG. 3. Modelling of a propagating earthquake source using fault elements.*

time taken for seismic waves to propagate from a point source on the fault to the site. The double summation over space integrates the contributions from a finite fault that has been discretized into a 2-D grid of subfault areas.

In theoretical methods, the earthquake source, path and site effects are described by physical models based on actual materials and phenomena. The source effects are represented by the fault model, and the path effects and the soil effects are represented by the Green's function. The Green's functions are calculated analytically or numerically, and they are scaled based on the slip time functions on each subfault. The waves are synthesized accordingly to the rupture process shown in Fig. 3. This method is rational because it is based on physical model, but it is difficult to apply this method to assessing short period ground motions, as it is necessary to model the source, the path and the soil in detail. The theoretical method has been developed by many researchers (see Refs [21–24]).

Since calculating the Green's function accurately in the short period range is difficult, semi-empirical methods have been developed. Two semi-empirical methods include the empirical Green's function method and the stochastic Green's function method.

The empirical Green's function method uses small earthquake records as Green's functions needed in the theoretical method to simulate the large ground motion. This method has the advantages that the probability of observing small earthquake ground motions at the target site is much higher than that of observing large earthquake ground motions, and that the small earthquake ground motions include the path effects and the soil effects. In the case that the soil effects are elastic, the synthetic result can be used without any investigation

of the soil. Moreover, the ground motions needed in earthquake resistant design for nuclear installations are predominantly short period ground motions that are affected by the complex rupture at the source and details of the three dimensional heterogeneous structure near the site. Since it is very difficult to reproduce or predict these short period ground motions by the theoretical method, the empirical Green's function method is useful in these cases. As in the theoretical method, it is necessary to model the source in detail, and the predicted ground motions can have large variations when the uncertainty in the fault parameters is taken into account. The empirical Green's function method has been developed by several researchers (see Refs [25–27]).

The stochastic Green's function method utilizes small earthquake motions generated in a computer as the Green's functions. The Fourier amplitudes and the envelop function of the time histories for generating the Green's functions are prescribed, and the soil effects are taken into account by considering amplification of the motions from the seismic basement to the surface. The stochastic Green's function method has been developed by some researchers [28, 29].

In actual practice, a hybrid method is often adopted, where the long period components are predicted by the theoretical method and the short period components are predicted by the semi-empirical method. A matching filter is used in this method (see Refs [30–32]).

### 3.1.3. Earthquake source rupture processes

Seismic waves are generated by abrupt slip on a fault. The elastic rebound theory provides the framework for modern earthquake source models [33, 34]. Fault slip begins at a point on the fault (hypocentre) and quickly spreads across the fault at a rate (rupture velocity) that is typically 80% of the shear velocity of the rock. Each point on the fault starts to slip when the moving rupture front arrives at that point, and it takes a finite amount of time (the rise time) for that point to undergo slip.

Ideally, the source parameters describing an earthquake rupture should be compatible with rupture dynamics: that is, be consistent with initial and boundary conditions that relate to the time varying strength and friction on the fault surface during the earthquake rupture process. Dynamic rupture models are currently the focus of intensive research, and at present are not widely used in quantitative engineering applications. The strong motion simulation procedures currently used in engineering seismology are mostly based on kinematic representations of the earthquake source. These methods prescribe the manner in which rupture evolves on the fault without checking whether that evolution is compatible with rupture dynamics.

The key parameters of a kinematic source model include the fault geometry (length, width, strike and dip), the direction of slip (rake angle), the time history of the fault slip (slip time function), the rupture initiation point (hypocentre) and the rupture velocity. Two important parameters of the slip time function at each point on the fault are the rise time and final amount of slip. When the site is within a few fault lengths of a fault that generates a large earthquake, it is necessary to use an extended fault plane to realistically represent finite fault effects such as rupture directivity effects and hanging wall effects. Otherwise, a finite source can be simplified to a point source in space for the purpose of simulating ground motions.

The fault rupture process is heterogeneous both spatially and temporally [35]. Smooth (coherent) components of the source process affect the generation of long period waves, whereas small scale (incoherent) components control the generation of high frequency waves. The small scale components are too complicated to be represented by a deterministic model, so they may be better treated as random phenomena and characterized by a stochastic model.

To implement such a heterogeneous source process in a simulation procedure, small scale heterogeneity can be imposed on a deterministic (smooth) source. For example, random perturbations to a constant rupture velocity can be used to produce an irregular rupture front, and the resulting accelerations and decelerations of the rupture front efficiently generate high frequency waves [36]. Similar randomization has been applied to other parameters such as the rise time, rake angle and static slip distribution [37–41]. Statistical models are now available to generate random slip distributions for future earthquakes [35, 39, 42]. Parameters for such statistical models are calibrated based on slip distributions from past earthquakes, and are constrained by seismological observations of far field motions.

Asperities are a key feature of earthquake rupture models. The word asperity means roughness: in rock mechanics, an asperity indicates the connecting interface of two rock bodies that controls the strength of the rock system [43]. Kanamori [44] and Lay and Kanamori [45] introduced the concept of the asperity into seismology to indicate a high strength region in order to explain the occurrence pattern of small earthquakes and large earthquakes along subduction zones. Das and Kostrov [46] applied the concept of the asperity to a high stress drop area in an earthquake, simplifying complex fault rupture into two typical areas: asperities of high stress drop and a background of free stress. Somerville et al. [35, 47] identified asperities by determining the area of large slip based on inversion results of slip distribution on the faults. References [48–50] showed that, for shallow crustal earthquakes, the asperities defined by the method

of Somerville et al. [35, 47] also correspond to the strong motion generation areas. However, recent large subduction interface earthquakes showed that the strong motion generation areas were located in the deeper part of the fault, while the large slip areas were located in a shallower part of the fault [51].

From studies of rupture process using waveform inversion of strong ground motion, it is understood that in the frequency range of interest for nuclear installations (0.1–100 Hz), strong ground motion is controlled by slip heterogeneity (asperities) rather than the average slip over the entire rupture area. Somerville et al. [35] characterized asperities as regions on the fault that have large slip relative to the average slip of the rupture area. They also found that the asperity areas, as well as the entire rupture areas, scale with the total seismic moment. An example of an earthquake rupture model is shown in Fig. 4. The top panel shows the distribution of slip obtained from a source inversion process [52]. The bottom panel shows the two asperities that were identified [35].

Two different approaches have been used to represent slip heterogeneity in forward rupture simulations. The first approach (see Refs [32, 53, 54]) uses a stochastic representation of the slip distribution and other source parameters. In the first two of these models, the slip distribution is specified using randomized spatial fields, constrained to fit certain wave number properties (see Refs [35, 42]).

The second approach (see Refs [50, 55–58]) uses a theoretical representation of the slip distribution and relevant source parameters. According to Ref. [50]:

“Based on two kinds of scaling relationships — one for the entire rupture area and the other for the asperity areas with respect to the total seismic moment — we found that the source model for the prediction of strong ground motions can be characterized by three kinds of parameters: outer, inner, and extra fault parameters. The outer fault parameters are conventional parameters characterizing the size of an earthquake, such as the rupture area and seismic moment, which give an overall picture of the source fault. The inner fault parameters, newly introduced in this study, define the slip heterogeneity within the seismic source. These parameters include the combined area of the asperities and the stress drop of each asperity, which have a major influence on the strong ground motions. The extra fault parameters are used to characterize the rupture nucleation and termination, such as the starting point and propagation pattern of the rupture. From a combination of the outer, inner and extra fault parameters we developed a ‘recipe’ for predicting strong ground motions for future large earthquakes (Irikura and Miyake, 2001 [59]; Irikura, 2004 [60]).”

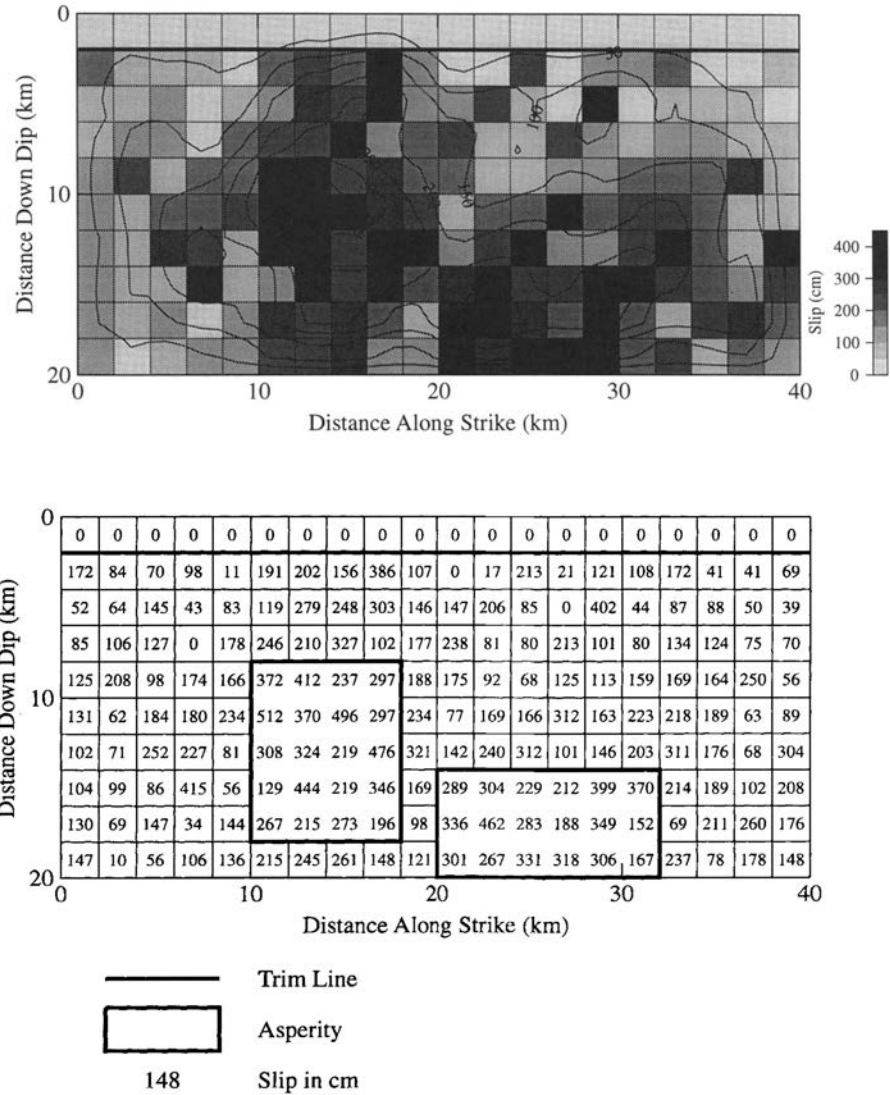


FIG. 4. Spatially variable slip (top) and its representation by discrete asperities in the 1989 Loma Prieta earthquake (reproduced from Ref. [35] with permission).

In the second source modelling approach for use in the simulation of near fault strong ground motions, including rupture directivity effects, the fault rupture is characterized using the strong motion generation area and asperity model (SMGA/asperity model). The SMGA/asperity model is a simplified source model that extracts the features from complex fault rupture models, and

can produce rupture directivity pulses [35, 47, 50]. The SMGA/asperity model is a source model consisting of SMGAs or asperities that are locked during the period between earthquakes and release elastic energy abruptly during the earthquake, and a background region that is not locked during the time period between earthquakes, and can slip during an earthquake.

The most significant feature observed in near source ground motions is the rupture directivity pulse [61]. The upper panel of Fig. 5 shows an example of directivity pulses observed in the 1995 Kobe, Japan, earthquake. Directivity pulses can be modelled by heterogeneous fault models such as the SMGA/asperity model, the hybrid model and the empirical/statistical model [62]. Matsushima and Kawase [63] showed that the directivity pulses numbered 1, 2, 3 and 5 in the upper panel of Fig. 5 came from the respective SMGAs/asperities numbered 1, 2, 3 and 5 in the lower panel. Near fault ground motions are described in more detail in Section 3.4.

Another significant feature of near source ground motions is displacement on the primary and secondary faults. Probabilistic and scenario based fault displacement hazard analysis is explained in the Annex.

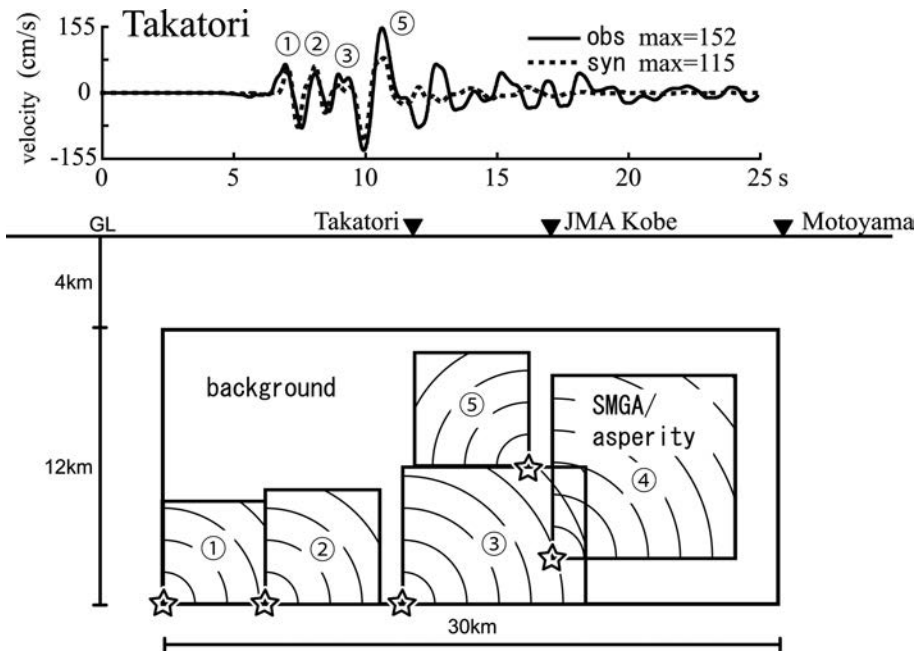


FIG. 5. Directivity pulses observed in the 1995 Kobe, Japan, earthquake (reproduced from Ref. [63] with permission).

### 3.1.4. Seismic wave propagation processes<sup>1</sup>

The effect of wave propagation in the Earth's crust is also called the path effect. Typical path effects include attenuation of wave amplitude due to geometrical spreading and inelastic energy absorption, reflection and refraction at the interface of distinct rock types (large scale heterogeneity), and wave scattering from small scale heterogeneities in the crust.

A Green's function is a mathematical function used in simulation procedures to represent the effects of wave propagation from a simple source to a station in any crustal structure. A Green's function is defined as the response of the Earth to a seismic point source, and depends only on the Earth's velocity structure and the site and source locations. Green's functions for point shear dislocation sources are used as building blocks to generate the ground motions caused by rupture of an earthquake on an extended fault plane.

The computation of theoretical Green's functions requires properties of the crustal structure such as the compressional and shear wave velocities, density, and damping factor (or seismic  $Q$  factor, where  $Q \approx 0.5/\beta$ ). Different assumptions of the crustal structure are used in different simulation procedures. Several stochastic procedures use a  $1/r_{\text{hyp}}$  ( $r_{\text{hyp}} =$  hypocentral distance) geometrical (see Refs [24, 64]). This is appropriate for the attenuation of shear waves in a homogeneous whole space, but it does not accurately represent seismic wave propagation in a layered crust. Green's functions for more realistic models of layered crust are also widely used to represent the first-order path effects of the Earth's crust [65–67].

When the site is inside a deep sedimentary basin or is expected to experience topographic effects, then an even more complicated crustal structure involving lateral variation of crustal properties and non-planar geometry may be used. Calculation of Green's functions for this type of complicated crustal structure is typically done by numerical methods such as finite element or finite difference. These methods remain computationally intensive and are often limited to long period ( $T > 1$  s) calculations.

The empirical Green's function approach [68–70] uses a recording, ideally at the site of interest, from a small earthquake located close to the fault whose ground motions are to be estimated. The empirical Green's function is considered more realistic than an analytical one because it contains wave propagation effects of the real Earth, including scattered waves. This is especially true for high frequency motions, which are strongly influenced by scattered waves. The application of this approach has many practical limitations. It is

---

<sup>1</sup> This section is based on section 6.2.2 of Ref. [20].

uncommon to have recordings of suitable earthquakes at the site of interest. Even if they are available, they may not span the full ranges of depth and distance required to represent a large earthquake on the fault. The signal-to-noise ratios of recordings are often inadequate, especially at long periods.

Waves scattered by small scale heterogeneities in the crust also contribute significantly to the complex appearance of recorded acceleration time histories. They prolong the ground shaking duration, redistribute energy among the three orthogonal components of shaking, and contribute to the spatial incoherence of ground motions. The distribution of small scale heterogeneities in the crust is not known, so it is only possible to predict the average characteristics of the scattered waves (i.e. wave envelope in the time domain, and mean power spectral density in the frequency domain) assuming random distribution of scatterers. Sato and Fehler [15] provide an extensive review of seismological models for the synthesis of scattered waves.

Some simulation procedures that explicitly include scattered waves [41] as signal generated noise in the simulated motions, where the signal is the deterministically computed theoretical Green's function. Other procedures include the scattered waves empirically, by using empirical Green's functions derived from strong motion recordings that include scattered waves generated in the real Earth.

### 3.2. OVERVIEW OF STRONG MOTION SIMULATION PROCEDURES

There is a variety of strong motion simulation procedures that take different approaches to the characterization of the earthquake source, seismic wave propagation, and site response. For example, the Southern California Earthquake Center (SCEC) Broadband Strong Motion Simulation Platform (see Appendix II) is constructed in a modular fashion that allows the user to choose among alternative methods of modelling these three aspects of ground motion simulation. The following sections summarize some of the strong motion simulation methods that have been proposed.

The stochastic method, which is the simplest method, and is most applicable at high frequencies. This method is used to characterize some aspects of high frequency ground motions in two more complex methods — the asperity method and the hybrid method — which are based respectively on deterministic and stochastic representations of fault heterogeneity. There is also the composite source model, which takes a different approach to representing fault heterogeneity.

### 3.2.1. Stochastic method

The simplest seismologically based strong motion simulation method is the stochastic method [28]. As explained in Ref. [71]:

“This method models ground motion as a time sequence of band limited white noise. A Fourier spectral model of the ground motion is constructed, starting with a model of the source spectrum and modifying its shape by factors to represent wave propagation effects.”

This method has been used for the generation of ground motion prediction methods for application at nuclear installations in the Central and Eastern United States of America (see Ref. [72]). The stochastic method is most appropriate at short periods where ground motions display the stochastic characteristics described above. At longer periods, it generally produces ground motions that are deficient because some implementations of the stochastic method do not consider earthquake source properties (such as the radiation pattern) and do not use Green’s functions to describe seismic wave propagation. The stochastic method is used to simulate high frequency ground motions in both of the ground motion simulation procedures described in detail below — the asperity model and the hybrid model [20]:

“There are two versions of this simulation procedure, one uses a point seismic source and the other uses a finite fault source. The point-source version uses an  $\omega$ -squared source model (Brune, 1970 [73], 1971 [74]) with a single corner frequency ( $f_c$ ) and a constant stress drop ( $\Delta\sigma$ ) (Boore, 1983 [28]; Atkinson, 1984 [75]).... The finite-source version combines aspects of the finite source....with the point-source ground motion model (Silva et al., 1990 [76]; Silva et al., 1995 [77]).... In the finite-source case, the approach of lagging-and-summing multiple Green’s functions over a 2D grid of subfaults is used. The finite source model includes a heterogeneous slip distribution, and the rupture velocity is taken as 0.8 times the shear-wave velocity at the depth of dominant slip. To capture heterogeneity in fault rupture propagation, a random perturbation of 20% is applied to the rupture velocity. Validation results of point- and finite-source versions (Silva et al., 1999 [78]) indicate that the finite-source model, on average, gives more accurate predictions than the point-source model for spectral periods  $T > 1$  s. For  $T < 1$  s, both versions give comparable results in terms of the modeling bias and variability (Silva et al., 1999 [78]).

“The effects of wave propagation are simply modeled by a  $1/r_{\text{hyp}}$  (or  $1/\sqrt{r_{\text{hyp}}}$  for surface wave) geometrical attenuation, crustal damping [modeled by a frequency dependent quality factor,  $Q(f)$ ], and crustal amplification due to the velocity gradient in the shallow crust. It is also possible to use either empirical or simplified numerical procedures (ray tracing) to account for the effects of reflection off crustal interfaces (such as Moho) (Ou and Herrmann, 1990 [79]; Boore, 1996 [80]).

“An equivalent-linear model is used to account for nonlinear 1D ground response. A simple damping function, parameterized by  $\kappa_{\dots}$ , is used to model the damping effect in the very shallow crust directly below the site (Hough and Anderson, 1988 [81]; Silva and Darragh, 1995 [82]). This damping effect is an attempt to model the observed rapid fall off of Fourier amplitude spectra beyond a maximum frequency (Hanks, 1982 [83]; Silva and Darragh, 1995 [82]). This observed phenomenon truncates the high frequency part of the spectrum, and along with corner frequency  $f_c$ , is responsible for the band-limited nature of predicted spectra from the stochastic ground motion model.

“This procedure predicts the power spectral density of stochastic ground motions with attractive simplicity. The predicted power spectral density, and the assumptions of normality and stationarity about the stochastic character of time histories, permit stable estimates of peak values of ground motions to be made without computing detailed time histories (Hanks and McGuire, 1981 [84]; Boore, 1983 [28]). Under these two assumptions, random vibration theory is used to relate a time-domain peak value to the time domain root-mean-square (RMS) value (Boore, 1983 [28]), which is calculated by integrating the power spectral density from zero frequency to the Nyquist frequency and applying Parsevall’s relation.

“Fourier phase spectra are needed to generate time-domain realizations of stochastic motions. One simple way is to generate random phases using a random number generator. A more attractive alternative is to carry the phase information (or time delays) in the finite-source procedure and, at the end, combine it with the phase spectrum of a real recording from an earthquake whose size is comparable to the subfault size (generally in the magnitude range of  $m = 5 - 6.5$ ). ... Interestingly, this phase spectrum need not be from a recording in the region of interest (Silva et al., 1989 [85]). Combining the amplitude and phase spectra, and transforming the resulting complex-valued Fourier spectrum back into the time domain then results

in one realization of the ground motion time history, which includes all of the aspects of a finite source as well as path and site effects.”

### 3.2.1.1. *Parameters of the stochastic method that require specification*

The following parameters require specification in the stochastic method:

- (a) Source:
  - Point source model: Seismic moment (equivalent to earthquake magnitude), and corner frequency (or frequencies), alternatively defined as the stress parameter, which defines the short period spectral level, including all but the longest periods of importance to engineering;
  - Finite source model: fault length, fault width, subfault size, hypocentre location and rupture velocity.
- (b) Path:  $Q$  (material damping factor, which may be frequency dependent) and source-to-site distance (or an empirical or numerical attenuation function; the latter derived from seismic velocities and densities of a flat layered crustal structure). The effect of the crustal structure, including the shear wave velocity at the surface, on ground motions levels is controlled by amplification functions for plane wave transmission upwards through a layered crust.
- (c) Site:
  - Surface seismic velocities, density and kappa (material damping factor);
  - Shear modulus and damping as a function of strain level for non-linear response.

### 3.2.1.2. *Alternative stochastic methods*

Alternative stochastic methods are proposed in Refs [24, 64, 72, 76, 86, 87].

## 3.2.2. **Asperity source model<sup>2</sup>**

In the asperity source model approach (see Refs [50, 53, 55, 57, 58]), the earthquake source is characterized by two types of region — asperities and background — as shown in Fig. 6.

---

<sup>2</sup> This section is based on Ref. [50].

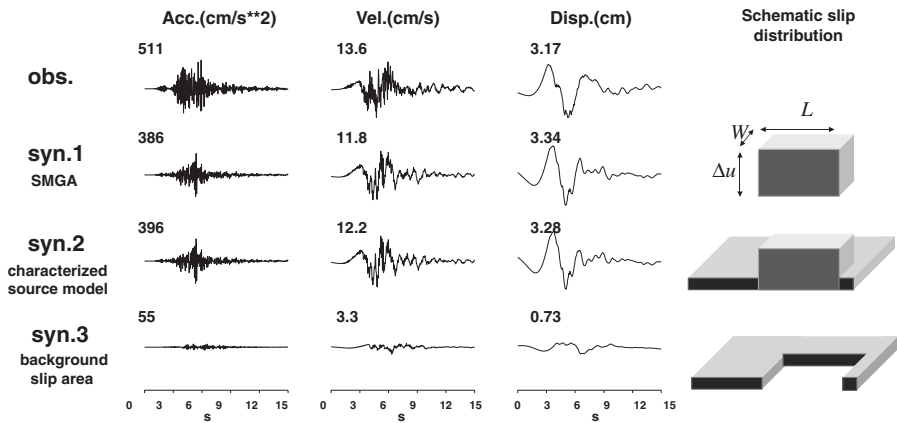


*FIG. 6. Schematic diagram illustrating the asperity source model (reproduced from Ref. [49] with permission).*

The procedure involves estimation of the outer fault parameters and the inner fault parameters in steps of the following sections.

### 3.2.2.1. Outer fault parameters estimation of seismic moment for possible earthquake

- Step 1: Total rupture area ( $S = LW$ )

The total fault length  $L$  of the target earthquake is defined as the sum of the lengths of the fault segments, grouping those simultaneously activated. The fault width  $W$  is related to the total fault length before reaching the thickness of the seismogenic zone  $W_{\max}$  and saturated at  $W_{\max}/\sin \theta$ , where  $\theta$  is the dip angle.

- Step 2: Total seismic moment ( $M_0$ )

The total seismic moment is estimated from the relationship between the seismic moment and rupture area.

- Step 3: Average stress drop on the fault

The average static stress drop for the rupture area is estimated by Eq. (1), in Section 3.2.2.4, for a circular crack model [88] at the first stage, and then by other formulas considering the tectonic loading stress (see Ref. [89])

at the second and third stages respectively, to naturally explain the three-stage scaling relationships of the seismic moment and rupture area.

### 3.2.2.2. Inner fault parameters slip heterogeneity or roughness of faulting

- Step 4: Combined area of asperities ( $S_a$ )

Two methods are used to determine the combined area of asperities. One is from the empirical relation of  $S_a - S$  [31, 59], where the combined area of asperities is specified to be around 22%. The other is from equations which estimate the acceleration level from empirical relations or observed records.

- Step 5: Stress drop on asperities ( $\Delta\sigma_a$ )

$\Delta\sigma_a$ , as the inner fault parameter, is derived by multiplying  $\Delta\sigma$ , as the outer fault parameter, by  $S/S_a$  from Step 4.

- Step 6: Number of asperities ( $N$ )

The asperities in the entire fault rupture are related to the segmentation of the active faults. The locations of the asperities are assumed from various kinds of information, such as the surface offsets measured along a fault, the back-slip rate found by GPS observations, and the weak reflection coefficients in the fault plane.

- Step 7: Average slip on asperities ( $D_a$ )

The average slip on asperities is based on Step 6 and the empirical relationships from the quasi-dynamic simulations of the slip distribution for the multiple asperity source model [90, 91].

- Step 8: Effective stress on asperity ( $\Delta\sigma_a$ ) and background slip areas ( $\Delta\sigma_b$ )

The effective stress ( $\sigma_a$ ) on an asperity for strong motion generation is considered to be almost identical to the stress drop on the asperity ( $\Delta\sigma_a$ ). The effective stress on the background slip area is constrained by the empirical relationship between the seismic moment and acceleration source spectral level (or between the effective stresses, the slips, and the widths of the asperity and the background) [92].

— Step 9: Parameterization of slip velocity time functions

There are several proposals of slip velocity time functions (e.g. see Refs [93–97]). In this Safety Report, the formulation of Nakamura and Miyatake [94] was adopted: the Kostrov-like slip velocity time functions are assumed to be functions of the peak slip velocity and rise time based on the dynamic simulation results of Day [93]. The peak slip velocity is given as the effective stress, rupture velocity and  $f_{\max}$ .

### 3.2.2.3. *Extra fault parameters propagation pattern of rupture*

The extra fault parameters of the rupture starting point and rupture velocity are used to characterize the rupture propagation pattern in the fault plane. For inland crustal earthquakes, the rupture nucleation and termination are related to the geomorphology of the active faults (e.g. see Refs [98, 99]). However, there is not enough knowledge and insufficient justification to fix the rupture's starting point (see Ref. [50] for examples of rupture starting points).

### 3.2.2.4. *Strong motion generation area/asperity method*

One version of the asperity model approach is the SMGA/asperity approach. In the following, major fault parameters of the SMGA/asperity model and their relationships are explained. Detailed procedures for evaluating the fault parameters of the SMGA/asperity model are explained for crustal earthquakes [58], for subduction interface earthquakes [58] and for intra-slab earthquakes [57] in Appendix I.

Figure 7 and Table 1 show six major fault parameters of the SMGA/asperity model: the fault area  $S$ , the averaged stress drop  $\Delta\sigma$ , the area of the combined SMGAs/asperities  $S_{\text{SMGA}}$ , the stress drop on the SMGAs/asperities  $\Delta\sigma_{\text{SMGA}}$ , the seismic moment  $M_0$ , and the short period level  $A$  (the flat level of the acceleration source spectrum in the short period range). The seismic moment  $M_0$  and the short period level  $A$  of the acceleration source spectrum are calculated from observed seismic waves of past earthquakes. These six parameters have the following three theoretical relationships [56]:

$$\Delta\sigma = \left( \frac{7}{16} \right) \left( \frac{M_0}{(S/\pi)^{1.5}} \right) \quad (1)$$

$$\Delta\sigma_{SMGA} = \left( \frac{S}{S_{SMGA}} \right) \Delta\sigma \quad (2)$$

$$A = 4\pi \left( \frac{S_{SMGA}}{\pi} \right)^{0.5} \Delta\sigma_{SMGA} \beta^2 \quad (3)$$

where  $\beta$  is the  $S$  wave velocity at the source, and the short period level from the background is assumed to be small enough to be ignored. Equation (1) is the averaged stress drop for circular crack models [88], while several equations for calculating the averaged stress drop have been obtained for other fault models (see Refs [100–102]). Equation (2) is obtained by the reciprocity theorem [103]. Equation (3) shows the short period level of the asperity model [104] based on that of the crack model [73, 105].

Values of three out of these six parameters need to be assigned to allow evaluation of the remaining three parameters. Table 1 shows fault parameters of the SMGA/asperity model assumed a priori for predicting strong ground motions and other major fault parameters evaluated by empirical and theoretical equations [57]. As shown in Table 1, the fault area is assumed a priori, and the seismic moment and the short period level is evaluated by the empirical equations for crustal earthquakes and subduction interface earthquakes, while the seismic moment is assumed a priori, and the area of the SMGAs/asperities and the short period level is evaluated by empirical equations for intra-slab earthquakes.

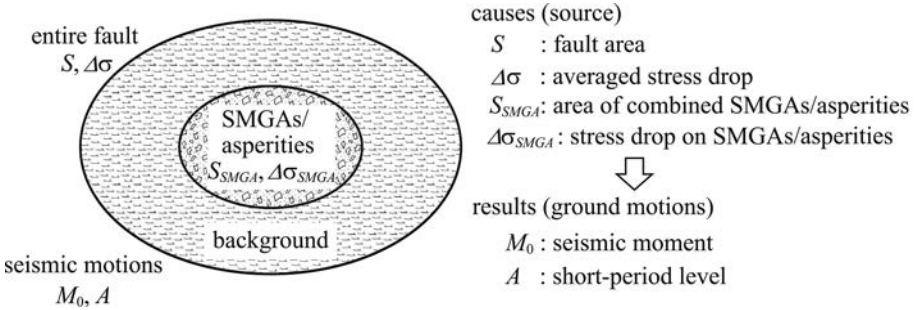


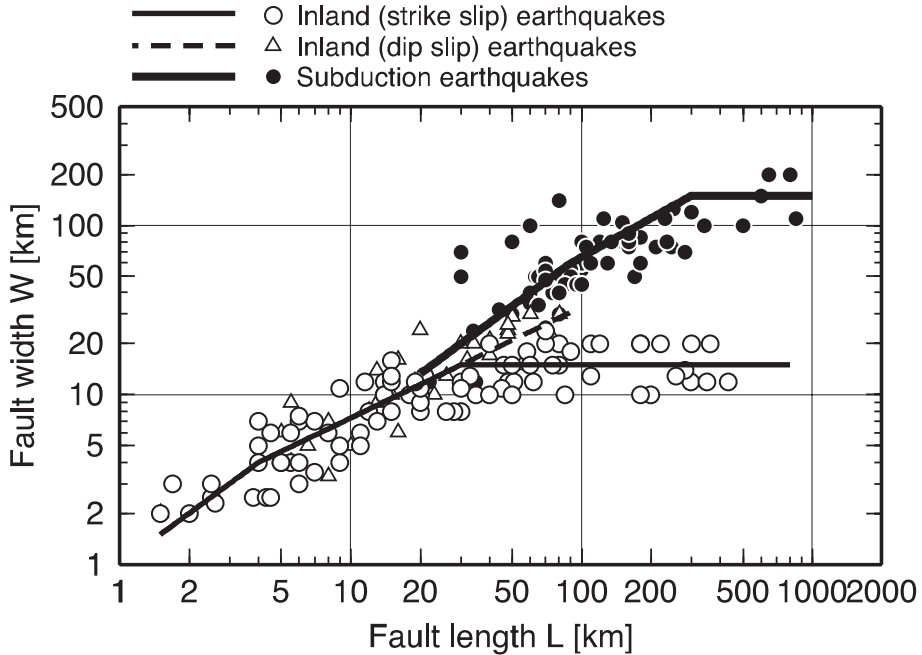
FIG. 7. Concept of the SMGA/asperity model.

TABLE 1. FAULT PARAMETERS OF THE SMGA/ASPERITY MODEL ASSUMED A PRIORI FOR PREDICTING STRONG GROUND MOTIONS AND OTHER MAJOR FAULT PARAMETERS EVALUATED BASED ON EMPIRICAL AND THEORETICAL EQUATIONS

Fault parameters	Category of earthquakes	
	Crustal and subduction interface	Intra-slab
Fault area: $S$	Assumed a priori based on the information on active faults or past earthquakes	Evaluated by the theoretical Eq. (29), in Appendix I, obtained from the theoretical Eqs (1)–(3)
Seismic moment: $M_0$	Evaluated by the empirical Eqs (11) or (12), in Appendix I	Assumed a priori based on the information on past earthquakes
Averaged stress drop: $\Delta\sigma$	Evaluated by the theoretical Eq. (1)	Evaluated by the theoretical Eq. (30), in Appendix I, obtained from the theoretical Eqs (1)–(3)
Area of combined SMGAs/asperities: $S_{\text{SMGA}}$	Evaluated by the theoretical Eq. (16), in Appendix I, obtained from the theoretical Eqs (2) and (3)	Evaluated by the empirical Eq. (27), in Appendix I
Stress drop on SMGAs/asperities: $\Delta\sigma_{\text{SMGA}}$	Evaluated by the theoretical Eq. (20), in Appendix I, obtained from the theoretical Eqs (2) and (3)	Evaluated by the theoretical Eq. (31), in Appendix I, obtained from the theoretical Eq. (3)
Short period level: $A$	Evaluated by the empirical Eq. (15), in Appendix I	Evaluated by the empirical Eq. (28), in Appendix I

**Source:** See Ref. [57].

For evaluating the fault width, the thickness of the seismogenic zone [43, 106] needs to be considered especially for crustal earthquakes caused by strike-slip faults because the fault width becomes constant in very long faults (see Fig. 8) [107].



*FIG. 8. Fault length and width for three types of earthquake (reproduced from Ref. [107] with permission).*

### 3.2.3. Hybrid source model

Graves and Pitarka [31, 32] developed a hybrid procedure for simulating broadband ground motions that combines a stochastic approach at high frequencies and a deterministic approach at low frequencies. An earlier version of the procedure is described in Ref. [108]. This simulation procedure has been implemented, validated and tested on the SCEC Broadband Platform. An example of its validation against the strong motion recordings of the 1989 Loma Prieta, California, earthquake is given in Section 4.2. A similar procedure has been used in nuclear installation licensing in California [47].

#### 3.2.3.1. Low frequency methodology ( $f < 1 \text{ Hz}$ )

“At low frequencies, we use a deterministic representation of source and wave propagation effects. The basic calculation is carried out using a 3D viscoelastic finite-difference algorithm, which incorporates both complex source rupture as well as wave propagation effects within arbitrarily heterogeneous 3D geologic structure (Graves, 1996 [23];

Pitarka, 1999 [24]). Anelasticity is incorporated using the coarse-grain approach of Day and Bradley (2001) [109]. We use a kinematic description of fault rupture incorporating spatial heterogeneity in slip and rupture velocity by dividing the fault into a number of subfaults. We use a slip velocity function that is constructed using two triangles following from the dynamic rupture analysis of Guaterri et al. (2003) [110]. The rise time comes from the empirical analysis of Somerville et al. (1999) [35] who find that CEUS events have average rise time that are 1.85 times longer than events in tectonically active regions. The rupture initiation time ( $T_i$ ) is determined using the expression

$$T_i = \frac{R}{V_r} - \delta t \quad (4)$$

where  $R$  is the rupture path length,  $V_r$  is the background rupture velocity (set at 80% of  $V_s$ ), and  $\delta t$  is a timing perturbation that scales linearly with slip amplitude such that  $\delta t = \delta t_0$  where the slip is at its maximum and  $\delta t = 0$  where the slip is at the average slip value. We set  $\delta t_0 = 0.5$  sec. This scaling results in faster rupture across portions of the fault having large slip as suggested by source inversions of past earthquakes (Yaji, 2004) [111] and dynamic rupture models (Day, 1982) [93]. For scenario earthquakes, the slip distribution can be specified using randomized spatial fields, constrained to fit certain wave number properties (e.g., Somerville et al., 1999 [35]; Mai and Beroza, 2002 [42])” [112].

### 3.2.3.2. High frequency methodology ( $f > 1$ Hz)

“The high frequency simulation methodology sums the response for each subfault assuming a random phase, an omega-squared source spectrum and simplified Green’s functions. The methodology follows from Boore (1983) [28] with the extension to finite-faults given by Frankel (1995) [113] and Hartzell et al (1999) [114]. Each subfault is allowed to rupture with a subfault moment weighting that is proportional to the final static slip amount given by the prescribed rupture model. The final summed moment is then scaled to the prescribed target mainshock moment. The convolution operator of Frankel (1995) [113] scales the subevent rise time to the target rise time. Additionally, this operator also ensures that the result is not dependent on the choice of the subfault dimensions” [115].

Beresnev and Atkinson [86] originally define a radiation strength factor, which is used as a free parameter in the specification of the subfault corner frequency as the following:

$$f_c = s \cdot z \frac{V_r}{\pi \cdot dl} \quad (5)$$

where

- $f_c$  is the corner frequency (Hz);
- $s$  is radiation strength factor;
- $z$  is a scaling factor relating  $f_c$  to the rise time of the subfault source;
- $V_r$  is the rupture velocity (km/s);

and  $dl$  is the subfault dimension (km).

In the approach by Graves and Pitarka [31], instead of allowing this to be a free parameter,  $z = C$  (constant) was assumed and:

$$s = \begin{cases} 1 & \text{if } h < h_0 \\ 1 + c_0 \frac{h - h_0}{h_1 - h_0} & \text{if } h_0 \leq h \leq h_1 \\ 1 + c_0 & \text{if } h \geq h_1 \end{cases} \quad (6)$$

where

- $h_0 = 5$  (km);
- $h_1 = 10$  (km);
- $h$  is the depth of the subfault centre (km);

and  $c_0 = 0.4$  based on calibration experiments.

Since corner frequency is proportional to slip velocity (inversely proportional to rise time), this formulation replicates the observed trend that slip velocity is relatively low for shallow ruptures and increases with increasing rupture depth [116].

This may cause the ground motions from surface faulting earthquakes to be weaker than those of earthquakes that do not break the ground surface [117–119]. For active tectonic regions,  $z$  is set to 1.6. In stable continental regions, the rise time is about 1.85 times longer than for active regions, which suggests  $z = 0.86$  for

such applications [120]. Allowing the subfault stress parameter ( $\sigma_p$ ) to be variable across the fault would accommodate a similar type of slip velocity scaling.

For the tectonically active crustal region (TCR),  $\sigma_p$  is fixed at 5 MPa. For stable continental region (SCR) applications, the stress parameter is set at 14.3 MPa, around three times larger than the stress parameter used for active tectonic regions (see Ref. [121]). This change in stress parameter most likely reflects the difference in rupture area for SCR events relative to active regions, which Somerville et al. [120] found to be a factor of around 2. Scaling the stress parameter by this factor yields a value of  $\sigma_p = 14.3$  MPa for SCR applications.

Graves and Pitarka [31] explained that:

“Our formulation also allows the specification of a plane layered velocity model from which we calculate simplified Green’s functions (GFs) and impedance effects. The GFs are comprised of the direct and Moho-reflected rays, which are traced through the specified velocity structure. Following Ou [and Herrmann, 79], each ray is attenuated by  $1/R_p$  where  $R_p$  is the path length traveled by the particular ray. For each ray and each subfault, we calculate a radiation pattern coefficient by averaging over a range of slip mechanisms and take-off angles, varying  $\pm 45^\circ$  about their theoretical values. Anelasticity is incorporated using a travel-time weighted average of the  $Q$  values for each of the velocity layers and using a kappa operator set at  $\kappa = 0.05$ . Finally, gross impedance effects are included using quarter wavelength theory (Boore [and Joyner, 122]) to derive amplification functions that are consistent with the specified velocity structure.”

According to Ref. [112]:

“In order to account for site specific geologic conditions in the final broadband response, we apply period-dependent, non-linear amplification factors to the simulated time histories. These factors are based on the 30 m travel-time averaged shear wave speed ( $V_s^{30}$ ) at the site of interest. Both the long period (3-D) and short period (1-D) computational models have minimum  $V_s^{30}$  values truncated at a constant reference value, typically between 600 m/s and 1000 m/s. This is done not only for computational efficiency, but also reflects our lack of sufficient knowledge regarding the detailed nature of the subsurface velocity structure, particularly in the upper few hundred meters. The site-specific amplification factors are based on equivalent-linear site response analysis (Walling et al., 2008) [123] as implemented in the GMPE of Campbell and Bozorgnia (2008) [8]. Those theoretical site factors have been shown to be generally consistent with empirical observation (Kwok and Stewart, 2006) [124].”

### 3.2.3.3. Parameters of the hybrid Green's function method that require specification

A typical set of input parameters used to characterize a kinematic model (see Table 2) includes fault length  $L$ , fault width  $W$ , rupture velocity  $V_r$ , permanent slip  $D$ , and rise time, which defines the slip velocity function. The output of these models is the earthquake ground motion on the free surface. The calculation of the ground motion is based on the elastodynamic representation theorem [12].

TABLE 2. SUMMARY OF PARAMETER VALUES USED IN BROADBAND SIMULATION PROCEDURE

Parameter	Fixed/variable
Rupture velocity	Slip dependent variation about fixed mean value $V_r$ (Eq. (4) in Section 3.2.3.1)
Subfault corner frequency	Fixed for a given region but depth dependent (Eqs (5) and (6) in Section 3.2.3.2) in a region dependent manner: $z = 0.86$ (SCR) and $1.6$ (TCR)
Stress parameter	Fixed for a given tectonic region: $14.3$ MPa (SCR) and $5$ MPa (TCR)
Coherence of radiation pattern	Fixed but frequency dependent
Seismic velocities, densities and $Q$	Fixed layer structure for a given region
Site amplification	Fixed, based on $V_s^{30}$

**Source:** See Refs [31, 32].

**Note:**  $Q$  — material damping factor; SCR — stable continental region; TCR — tectonically active crustal region.

The following is general description of the parameters used in the simulation procedure:

- (a) Source:
  - (i) Event specific methods are used to prescribe:
    - Seismic moment;
    - Mechanism;
    - Hypocentre.

- (ii) Region specific methods are used to prescribe:
  - Moment rupture area relations;
  - Stress parameter;
  - Rise time and corner frequency.
- (iii) Rule based procedures are used to specify:
  - How rupture parameters (correlation of slip distribution, average rise time and average rupture speed perturbations) scale with moment;
  - Scaling with depth of rise time and rupture speed;
  - Rise time and corner frequency adjusted for buried thrust ( $a_T$ );
  - Local rise time and rupture speed perturbations scale with local slip.
- (b) Path: Region specific methods are used to prescribe:
  - Seismic velocities;
  - Density;
  - $Q$  (material damping factor) of a crustal model that may be plane layered (1-D, 2-D or 3-D).
- (c) Site: Site specific methods are used to prescribe:
  - Surface seismic velocities;
  - Density;
  - Kappa (material damping factor);
  - Shear modulus and damping as a function of strain level for non-linear response.

#### *3.2.3.4. Alternative hybrid methods*

Alternative hybrid methods are proposed in Refs [32, 53, 97, 125, 126].

#### **3.2.4. Composite source model**

In the composite source method, the earthquake source is represented as a superposition of circular subevents with a constant stress drop [54]. According to Ref. [20]:

“The number of subevents and their radius follows a power law [a Gutenberg-Richter relationship]. The heterogeneous nature of the composite earthquake faulting is apparently characterized by the maximum subevent size and the subevents’ stress drop, which are constrained by independent geophysical data. The random nature of the heterogeneities on a complex fault is simulated by distributing the subevents randomly on the fault plane.”

The subevents are allowed to overlap, and need to overlap in order to match the seismic moment of the earthquake: “Rupture propagates from the initiation point at a constant rupture velocity. Each subevent initiates the radiation of a displacement pulse, calculated using a crack model” [20].

This differs from the asperity and hybrid source models described in Sections 3.2.2 and 3.2.3, which assume a continuous slip function at each point on the fault, and which use a very dense sampling of point sources on the fault plane and coherent propagation of rupture across the fault plane to provide a realistic representation of rupture directivity effects. Rupture directivity effects are incorporated in the composite source model by the delays in the times subevents are initiated. According to Ref. [20]:

“Wave propagation is modeled using analytical Green’s functions calculated for a flat-layered medium.... The short-period components of the Green’s functions are modified for the effects of random lateral heterogeneity by adding scattered waves into the Green’s function (Zeng, 1995) [127].... The solution is then further modified by propagating the motions as vertically propagating plane waves through a near-surface 1D velocity profile. Thus, the complex high-frequency waveform of this simulation procedure is generated from the combination of a heterogeneous source, wave reverberation in a stratified shallow crustal structure, and scattering from lateral heterogeneity.

“Linear site response may be directly incorporated in the Green’s function computations. Similar to the Stochastic Ground Motion Model, inelastic effects in the shallow site response are modeled using a simple inelastic attenuation function (Hough and Anderson, 1988 [81]; Silva and Darragh, 1995 [82]) that represents the absorption of seismic energy in the shallow subsurface directly below the site.”

Alternatively, the model can find the motion for a stiff material layer at the site, and then: “A ground response calculation may be used outside the computation to accommodate nonlinear site response” [20].

#### *3.2.4.1. Parameters of the composite source model that require specification*

- (a) Source: Seismic moment, fault length, fault width, strike, dip, depth of top of fault, hypocentre, rupture velocity and the parameters of a probability distribution for dimensions of circular patches of slip on the fault. The probability distribution for dimensions of the circular patches may be used

to easily generate multiple realizations of the source model, allowing the user to study the effects of alternative slip functions.

- (b) Path: Seismic velocities, density and  $Q$  (material damping factor) of a crustal model that may be plane layered (1-D, 2-D or 3-D). The most sensitive parameters are velocity gradients in the shallow and deep parts of the crust (used directly to calculate Green's functions).
- (c) Site: Surface seismic velocities, density and  $Q$  (material damping factor) shear modulus and damping as a function of strain level for non-linear response. The radiation from the subevents follows an omega-square spectrum. Thus observed distance dependence of kappa and site specific values of kappa-zero [81, 82] are ideally achieved when consistent values of  $Q$  are used at depth and in the shallow layers, thus implementing the model that kappa is a result of an omega-square source model modified by attenuation. When that is not achieved, the seismogram can be adjusted for the difference between the target and synthetic values of kappa, although this adjustment is not the preferred approach.

### 3.3. VALIDATION OF SIMULATED GROUND MOTIONS

The ground motion simulation methods described in this Safety Report have been tested and validated against recorded data. A method for engineering applications should not only be based on well founded seismological models of earthquake source, wave propagation, and site response, but should also have demonstrated ability to match the ground motion characteristics of recorded earthquakes that are of engineering interest. A method for quantifying the goodness of fit between recorded and simulated ground motions was developed by Abrahamson et al. [128]. The measurement of goodness of fit can be applied to any ground motion parameter of interest, such as peak ground acceleration, peak ground velocity, response spectral accelerations and duration. To date, most goodness of fit measurements have used response spectral acceleration, but measurements of waveform characteristics have also been proposed (see Ref. [129]). Stewart et al. [20] described that the misfit, or residual, is “computed as the difference between the logarithms of the observed and the predicted intensity measure”, and explained that (*footnote omitted*):

“The effectiveness of a simulation procedure at predicting a particular intensity measure is measured in terms of the misfit. The misfit is partly due to the fact that seismological models implemented in any simulation procedure are only approximations to the real physical processes.”

In addition, errors in the estimated model parameters can give rise to misfit, even if the seismological models are perfect.

The misfit between the estimated and actual ground motion parameters is quantified by measuring the difference in response spectra of the recorded and simulated ground motion time histories. For example, Graves and Pitarka [32] described the validation of the simulation procedure against recorded ground motions using formal goodness of fit methods. The following is based on their work.

They compared the data and simulations using the model bias and standard error for 5% damped spectral acceleration calculated from the broadband time series (see Ref. [130]). For the  $j$ -th station, the residual between the observed and simulated spectral acceleration at a period  $T_i$  is given by:

$$r_j(T_i) = \ln\left(\frac{O_j(T_i)}{S_j(T_i)}\right) \quad (7)$$

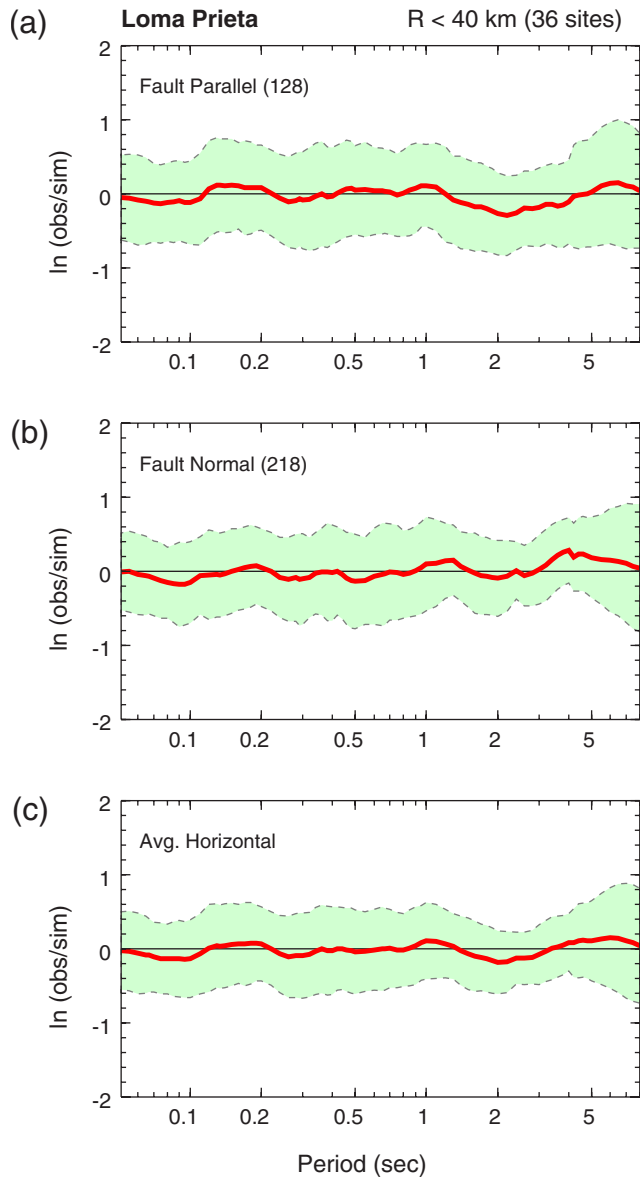
where  $O_j(T_i)$  and  $S_j(T_i)$  are the observed and simulated values on a given component, respectively. The model bias is then given by:

$$B(T_i) = \frac{1}{N} \sum_{j=1,N} r_j(T_i) \quad (8)$$

and the standard error is given by:

$$\sigma(T_i) = \left( \frac{1}{N} \sum_{j=1,N} [r_j(T_i) - B(T_i)]^2 \right)^{1/2} \quad (9)$$

where  $N$  is the total number of stations. Figure 9 shows the model bias and standard error for the Loma Prieta simulation. For this comparison, they computed separate measures for the horizontal components of motion oriented in the fault parallel ( $128^\circ$  azimuth) and fault-normal ( $218^\circ$  azimuth) orientations were computed, as well as their geometric mean (average horizontal). They only considered sites in the near-fault region: that is, those located within one fault length (40 km) of the rupture surface. There are a total of 36 sites within this distance range. The comparisons shown in Fig. 9 exhibit little systematic model bias across a wide frequency range.



**Note:** (a) Panel is for the fault-parallel component; (b) panel is for the fault-normal component; and (c) panel is for the average horizontal (geometric mean) component.

*FIG. 9. Model bias (heavy line) and standard error (shaded region) for 5% damped spectral acceleration using 36 sites for the Loma Prieta earthquake [32] (courtesy of the Seismological Society of America).*

The difference between the recorded and simulated ground motions has an average standard error of a factor of 1.8. This value is comparable to values for empirical ground motion prediction models. This demonstrates that the predicted motion at a given site may have significant variability (e.g. a factor of 1.8), even though the bias (which represents the average misfit over all recordings) may be quite small. The modelling variability, quantified by the bias and the standard error of the model misfit, along with the parametric variability associated with the model parameters for a future earthquake, contribute to the total uncertainty of predicted motions when the simulation procedure is used to predict ground motions for design. The treatment of uncertainties in simulated ground motions are described further in Section 4.3.

### 3.4. FEATURES OF NEAR SOURCE GROUND MOTIONS: RUPTURE DIRECTIVITY AND FLING STEP

#### 3.4.1. Introduction<sup>3</sup>

Near fault ground motions are different from ordinary ground motions in that they often contain strong coherent dynamic long period pulses and permanent ground displacements. The coherent long period pulses are caused by rupture directivity effects due to rupture propagation. An earthquake is a shear dislocation that begins at a point on a fault and spreads at a velocity that is almost as large as the shear wave velocity. The propagation of fault rupture towards a site at a velocity close to the shear wave velocity causes most of the seismic energy from the rupture that arrives at the site to occur in a large pulse of motion early in the record [61, 132]. This pulse of motion represents the cumulative effect of almost all of the seismic radiation from the fault to that site. The radiation pattern of the shear dislocation on the fault causes this large pulse of motion to be oriented in the direction perpendicular to the fault plane, causing the strike normal component of ground motion to be larger than the strike parallel component at periods longer than around 0.5 seconds. To accurately characterize near fault ground motions, it is therefore necessary to specify separate response spectra and time histories for the strike normal and strike parallel components of ground motion.

---

<sup>3</sup> This section is based on Ref. [131].

Near fault recordings from recent earthquakes indicate that the directivity pulse is a narrow band pulse whose period increases with magnitude, as expected from the theory [62, 117, 133]. This magnitude dependence of the pulse period causes the response spectrum an amplification around the pulse period, such that the near fault ground motions from moderate magnitude earthquakes may exceed those of larger earthquakes at intermediate periods (around 1 second).

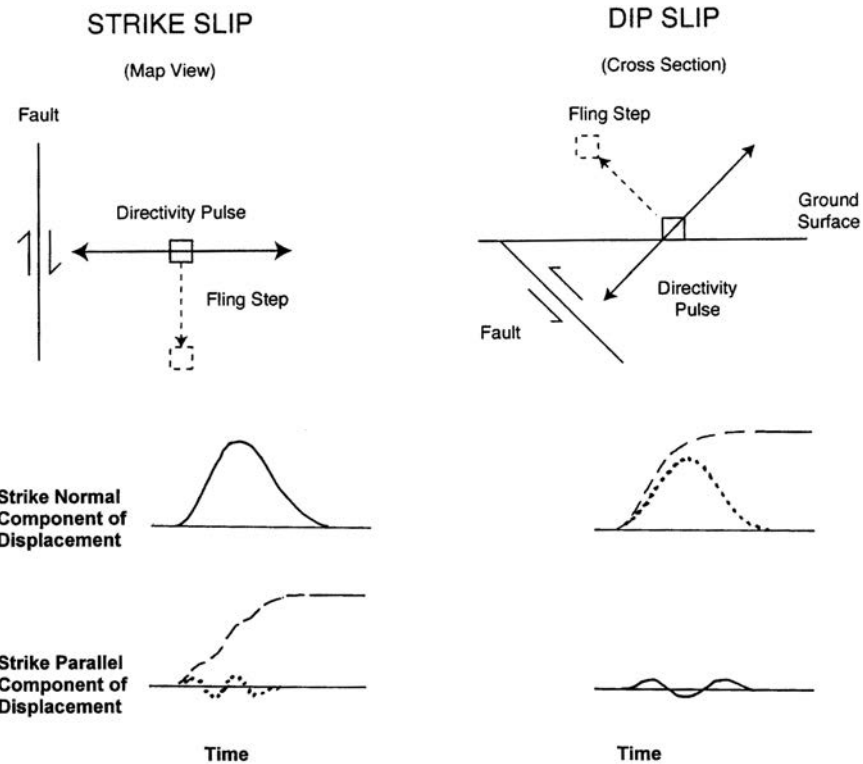
Current models for predicting rupture directivity effects are summarized by Spudich et al. [134]. The earthquake also generates static deformation of the ground. The static ground displacements in near fault ground motions are caused by the relative movement of the two sides of the fault on which the earthquake occurs. The static deformation of the ground consists of a discontinuity in displacement on the fault itself, and a gradual decrease in this displacement away from the fault on either side of the fault. If there is surface faulting, the static displacements are discontinuous across the fault at the ground surface, constituting a primary seismic hazard. Even if the fault does not break the surface, there is static deformation of the ground surface due to subsurface faulting. The static ground displacements occur at about the same time as the large dynamic motions, indicating that the static and dynamic displacements need to be treated as coincident loads.

### 3.4.2. Orientation of dynamic and static near fault ground motions<sup>4</sup>

The top part of Fig. 10 schematically illustrates the orientations of dynamic and static near fault ground motions. The strike-slip case is shown in map view, where the fault defines the strike direction. The rupture directivity pulse is oriented in the strike normal direction and the static ground displacement ('fling step') is oriented parallel to the fault strike. The dip-slip case is shown in vertical cross section, where the fault defines the dip direction; the strike direction is orthogonal to the page. The rupture directivity pulse is oriented in the direction normal to the fault dip, and has components in both the vertical direction and the horizontal strike normal directions. The static ground displacement is oriented in the direction parallel to the fault dip, and has components in both the vertical direction and the horizontal strike normal direction.

---

<sup>4</sup> This section is based on Ref. [131].



**Note:** Top — Schematic orientation of the rupture directivity pulse and fault displacement ('fling step') for strike-slip (left) and dip-slip (right) faulting. Bottom — Schematic partition of the rupture directivity pulse and fault displacement between strike normal and strike parallel components of ground displacement. Waveforms containing static ground displacement are shown as dashed lines; versions of these waveforms with the static ground displacement removed are shown as dotted lines.

FIG. 10. Directivity pulse and fling step.

The bottom part of Fig. 10 schematically illustrates the partition of near fault ground motions into the dynamic ground motion, which is dominated by the rupture directivity pulse, and the static ground displacement. For a strike-slip earthquake, the rupture directivity pulse is partitioned mainly on the strike normal component, and the static ground displacement is partitioned on the strike parallel component. If the static ground displacement is removed from the strike parallel component, very little dynamic motion remains. For a dip-slip earthquake, the dynamic and static displacements occur together on the strike normal component, and there is little of either motion on the strike parallel component. If the static

ground displacement is removed from the strike normal component, a large directivity pulse remains.

There need not be a strong correlation between the static and dynamic components of near fault ground motion. For example, the 1989 Loma Prieta and 1994 Northridge earthquakes both occurred on faults that did not break the ground surface, so they produced very small static ground displacements, but they did produce strong rupture directivity pulses. For this reason, the dynamic and static ground motions need to be quantified in separate hazard analyses for practical application at a site if the structure is sensitive to both dynamic ground motions and static ground displacements.

### **3.4.3. Different strike normal and strike parallel components of horizontal dynamic motions<sup>5</sup>**

Somerville et al. [61] developed a model for the ratio of strike normal to average horizontal motions caused by rupture directivity effects this model was updated in Spudich et al. [134]. They found that this ratio depends primarily on earthquake magnitude and rupture distance, while the dependencies on faulting mechanism and site category were not found to be practically significant. The ratio of strike normal to average horizontal motions is found to be period dependent, and becomes significant for periods greater than 0.6 seconds, indicating a transition from incoherent source radiation and wave propagation conditions at short periods to coherent source radiation and wave propagation conditions at long periods.

### **3.4.4. Incidence of the rupture directivity pulse<sup>6</sup>**

Forward rupture directivity effects occur when two conditions are met: the rupture front propagates towards the site; and the direction of slip on the fault is aligned with the direction of wave propagation towards the site. The conditions for generating forward rupture directivity effects are readily met in strike-slip faulting, where the rupture propagates horizontally along strike either unilaterally or bilaterally, and the fault slip direction is oriented horizontally in the direction along the strike of the fault. However, not all near fault locations experience forward rupture directivity effects in a given event. Backward directivity effects, which occur when the rupture propagates away from the site, give rise to the opposite effect: long duration motions having low amplitudes at long periods.

---

<sup>5</sup> This section is based on Ref. [11].

<sup>6</sup> This section is based on Ref. [11].

The conditions required for forward directivity are also met in dip-slip faulting. The alignment of both the rupture direction and the slip direction updip on the fault plane produces rupture directivity effects at sites located around the surface exposure of the fault (or its updip projection if it does not break the surface). Unlike the case for strike-slip faulting, where forward rupture directivity effects occur at all locations along the fault away from the hypocentre, dip-slip faulting produces directivity effects on the ground surface that are most concentrated in a limited region updip from the hypocentre.

#### 3.4.5. Duration of near fault time histories<sup>7</sup>

Directivity effects induce systematic spatial variations of duration in near fault ground motions. In general, the time history is compressed in time in the forward directivity region, especially on the strike normal component, while in the backward directivity region the time history is elongated in time. Brief durations are a predictable feature of near fault ground motions unless there is the potential for multiple rupture episodes on a complex fault system or there is the potential for basin response to generate long durations.

Somerville et al. [61] developed an empirical model for the dependence of duration on the location of the recording site in relation to the fault.

#### 3.4.6. Response spectrum for design and analysis

In a scenario based analysis, the magnitude and its associated pulse period  $T_p$  will be prescribed. In this case, it is appropriate to use a narrow band directivity response spectral model for which there will be a peak in the response spectrum corresponding to the value of  $T_p$ . In the probabilistic approach, the hazard will consist of contributions from a range of earthquake magnitudes, which can be identified from the deaggregation of the hazard. This magnitude distribution can be used at assess whether it is preferable to use a narrow band model, suitable for a narrow range of magnitudes, or a broadband model, suitable for a wider range of magnitudes.

#### 3.4.7. Selection of near fault time histories for design and analysis

Near fault time histories used for non-linear analyses of structures need to reliably represent the non-stationary characteristics of the directivity pulse in the time domain. It may not be sufficient to apply standard procedures to match

---

<sup>7</sup> This section is based on Ref. [11].

recorded or simulated accelerograms to the elastic response spectrum, even if the spectrum modified to include near source directivity effects as described above. If recorded time histories containing directivity pulses are available for the directivity conditions at the site, it is preferable to use them. Otherwise, simulated near fault time histories should be used, but their durations should be checked for consistency with analogous recorded time histories.

In a scenario based analysis, the magnitude, distance, style of faulting and directivity parameters are provided by the scenario, and the response spectrum is provided by GMPEs. In most cases, the scenario should embody forward rupture directivity effects, whose strength depends on directivity parameters such as the angular separation between the slip direction on the fault and the path to the site. In the probabilistic approach, the hazard can be deaggregated to identify the predominant magnitude, distance and directivity parameters, and the response spectrum is provided by the probabilistic seismic hazard analysis. The deaggregation of the probabilistic hazard will indicate the proportion of time histories that should contain forward rupture directivity effects.

Two additional parameters are important in the selection of candidate time histories: the pulse period  $T_p$  and the peak ground velocity — both of which can be calculated from the magnitude and distance using empirical relations. Candidate ground motion records containing directivity pulses are available in literature, and different classification schemes have been proposed for the identification of pulse-like time histories.

### 3.4.8. Scaling and matching of near fault time histories

Scaling of ground motions to the design response spectrum should be done over the broad range of 0.01–10 seconds, focusing on the period range around the pulse period  $T_p$ . If spectrum matching techniques are applied, it is important to preserve the pulse-like characteristic of the time history after matching. This can be done using a qualitative visual check on the acceleration, velocity, and displacement time history and the normalized energy summation curve (HUSID diagram), or by using methods that quantify the parameters of directivity pulses [62, 133].

An alternative approach is to extract the velocity pulse from the selected record before spectral matching to a response spectrum that does not contain directivity effect, and added the pulse back in to the record after scaling it so that the combined response spectrum matches the response spectrum that incorporates directivity.

### **3.4.9. Orientation of components**

The rupture directivity pulse is oriented in the strike normal direction, so the response spectra and time histories should be specified separately in two horizontal directions. If the fault geometry and the source mechanism are known, the fault normal and fault parallel components can be applied in their natural orientations, or rotated to the axis of the structure. Otherwise, they can be applied in an arbitrary orientation.

## **4. EXAMPLES OF GROUND MOTION EVALUATION BASED ON HETEROGENEOUS SOURCE MODELS**

Section 4 provides some examples of ground motion evaluation based on the heterogeneous source models. Section 4.1 shows an example based on the SMGA/asperity model for the crustal earthquake, the subduction interface earthquake and the intra-slab earthquake. Section 4.2 provides examples of ground motion evaluation based on the hybrid source model, and Section 4.3 explains the uncertainty treatment in the fault rupture modelling.

### **4.1. EXAMPLES OF PREDICTED GROUND MOTIONS BASED ON THE SMGA/ASPERITY MODEL**

This section shows examples of strong ground motions predicted for a crustal earthquake, for a subduction interface earthquake, and for an intra-slab earthquake based on the SMGA/asperity model.

#### **4.1.1. Crustal earthquake**

Figure 11 shows the fault model of a hypothetical earthquake of magnitude around 8 caused by the Itoigawa-Shizuoka Tectonic Line [135]. In this fault model, the fault length and the fault dip were assumed a priori based on the results of geological surveys.

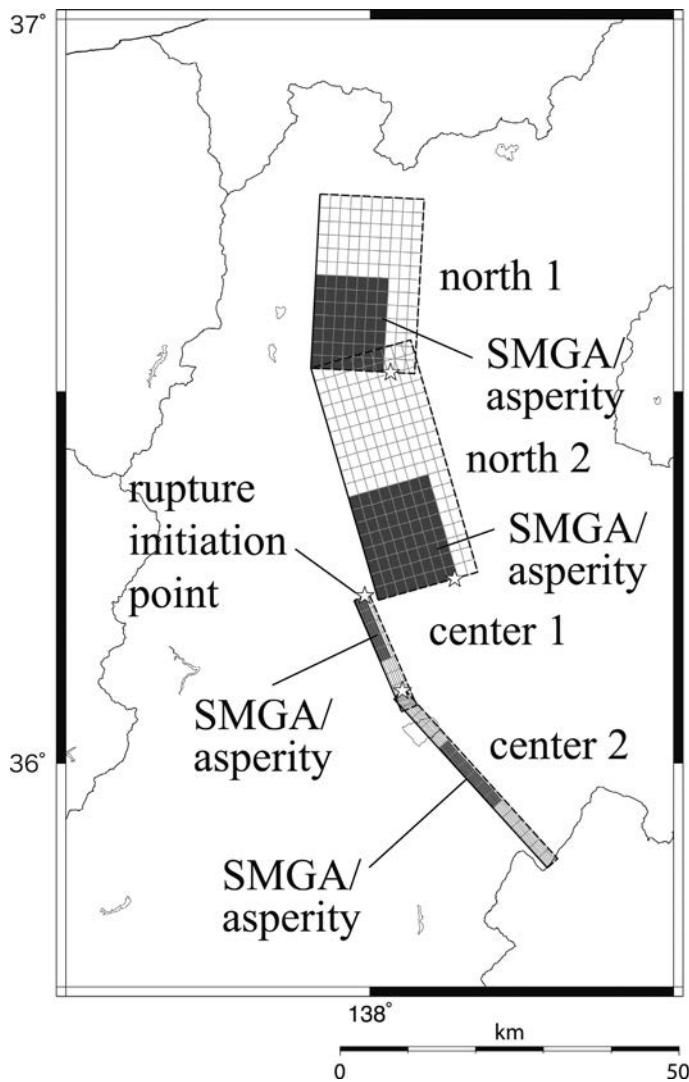


*FIG. 11. SMGA/asperity model of a hypothetical earthquake with a magnitude of around 8 caused by the Itoigawa-Shizuoka Tectonic Line (reproduced from Ref. [135] with permission).*

Strong ground motions were predicted by a hybrid method composed of the theoretical method [23] and the stochastic Green's function method [131].

Figure 12 [135] shows the comparison between peak ground velocities in the hypothetical M8 earthquake caused by the Itoigawa-Shizuoka Tectonic Line and those from the GMPE [5]. The predicted peak ground velocities agree

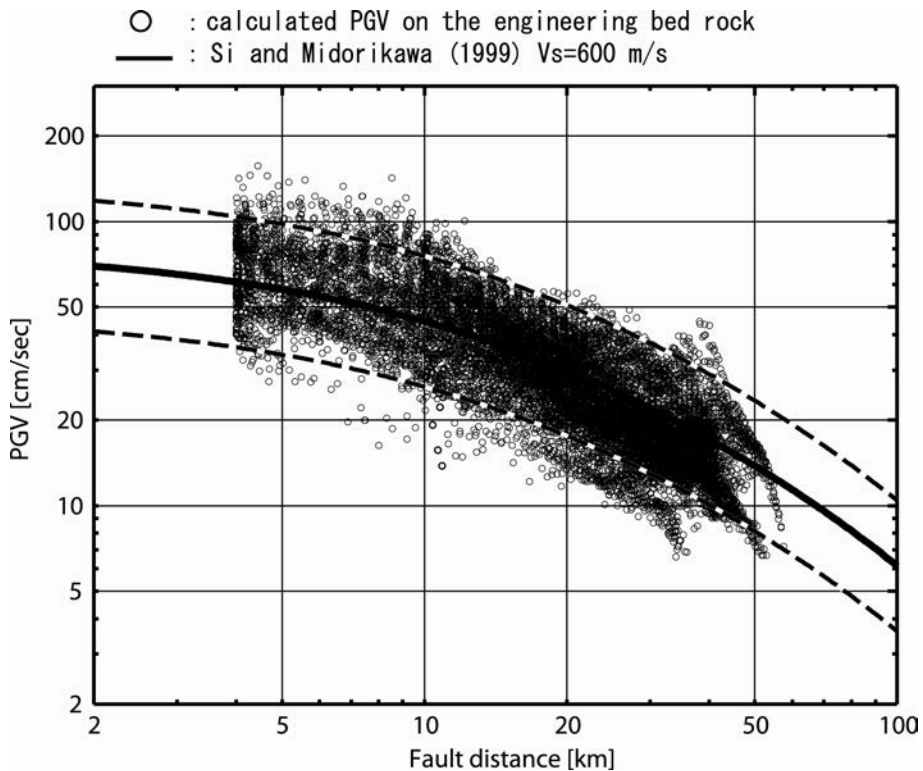


*FIG. 12. Comparison between peak ground velocities from a hypothetical earthquake with a magnitude of around 8 caused by the Itoigawa-Shizuoka Tectonic Line [135] and those from the GMPE [5] (reproduced from Ref. [135] with permission).*

well with the GMPE, indicating the consistency of the fault parameters with those that underlie the extrapolation of the recorded data in the GMPE.

The small open circles show peak velocities at 12 450 points on every 1 km mesh in the region 75 km wide in the east–west direction and 166 km long in the north–south direction near the fault. The shortest distance from the fault is 4 km, since the depth to the top of the fault is 4 km.

#### 4.1.2. Subduction interface earthquake

Figure 13 shows the fault model of a hypothetical Miyagi-Ken Oki, Japan, earthquake with a moment magnitude of 7.6 [136]. The model parameters such as the stress drop and the geometry of SMGAs/asperities were identified by fitting the simulated motions to the observed strong motion records. The strong ground motions were calculated by the stochastic Green’s function method [137].

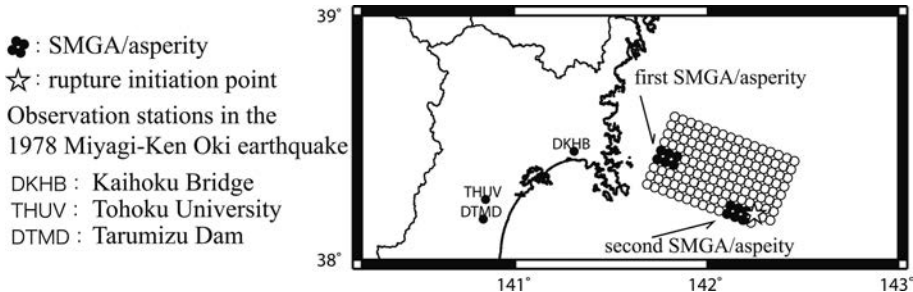


*FIG. 13. Fault model of a hypothetical Miyagi-Ken Oki, Japan, earthquake with a moment magnitude of 7.6 (reproduced from Ref. [136] with permission).*

Figure 14 shows the comparison between the calculated ground motions at Kaihoku Bridge in the hypothetical Miyagi-Ken Oki earthquake and the observed ground motion in the 1978 Miyagi-Ken Oki earthquake [136]. The agreement between the calculated motion and observed motion results from the adjustment of the asperity location, asperity area and stress drop described above.

Based on the rupture model of the M7.6 the Miyagi-Ken Oki earthquake (see Fig. 13), Dan et al. [138] developed a fault model for a larger earthquake with a moment magnitude of 8.2. The Tohoku Electric Power Company adopted this model for assessing the design input earthquake ground motions for nuclear power plants as shown in Fig. 15 [139]. The validation of this modelling procedure was later shown by comparing the ground motions predicted based on this model with the records in the 2011 Tohoku earthquake with a moment magnitude of 9.0 (see Fig. 16) [140].

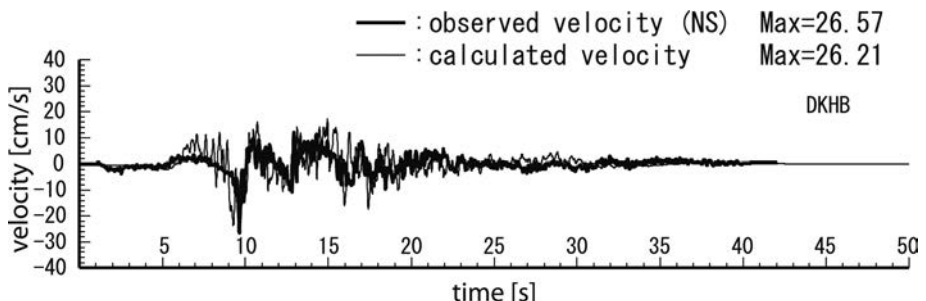


*FIG. 14. Comparison between the calculated ground motions at Kaihoku Bridge in the hypothetical Miyagi-Ken Oki earthquake and the observed ground motion in the 1978 Miyagiken Oki earthquake (reproduced from Ref. [136] with permission).*

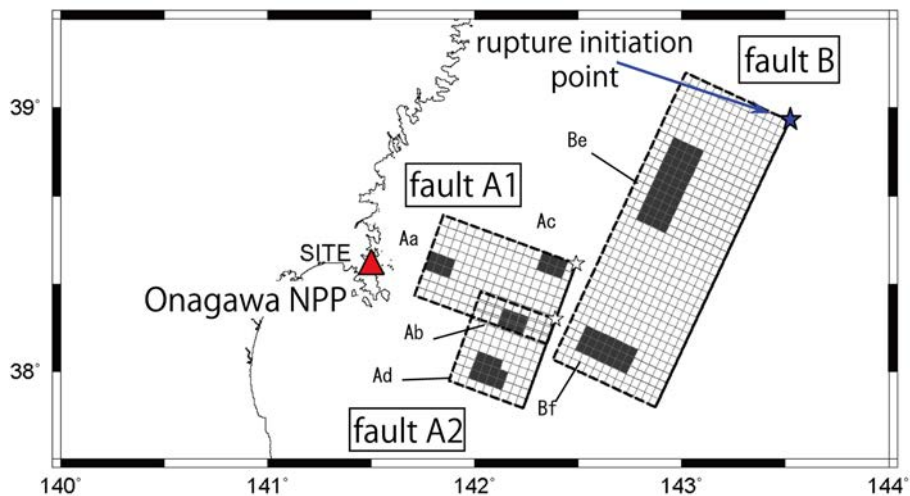


FIG. 15. SMGA/asperity model for the Miyagi-Ken Oki earthquake with a moment magnitude of 8.2 (reproduced from Ref. [139] with permission).

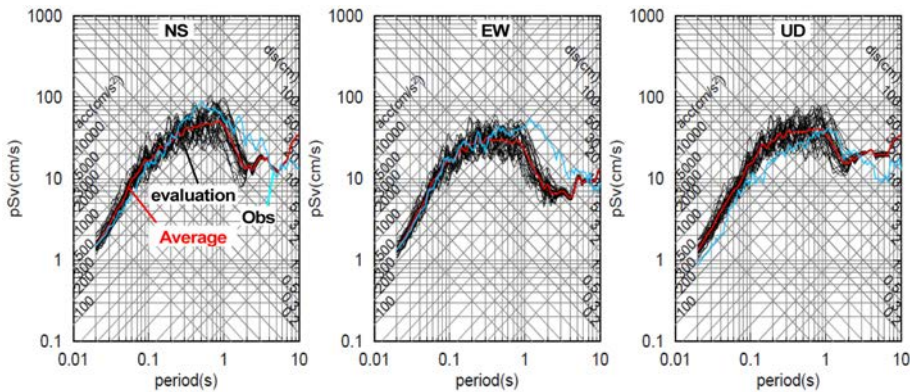


FIG. 16. Response spectrum comparison of evaluated ground motions (black) with the seismic ground motions (blue) observed during the Tohoku earthquake (reproduced from Ref. [140] with permission).

#### 4.1.3. Intra-slab earthquake

An intra-slab earthquake occurred at Miyagi-Ken Oki in 2003, and several SMGA/asperity models that reproduce the strong ground motion records were proposed.

Figure 17 shows one of the proposed SMGA/asperity models [57] for the 2003 Miyagi-Ken Oki intra-slab earthquake, which had a seismic moment  $M_0$  of  $3.49 \times 10^{19}$  N·m. The area of the SMGAs/asperities  $S_{\text{SMGA}}$  was estimated using Eq. (27), in Appendix I, and the short period level  $A$  by Eq. (28), in Appendix I. The entire fault area  $S$ , the average stress drop  $\Delta\sigma$ , and the stress drop on the SMGA/asperity were calculated using Eqs (29)–(31), in Appendix I.

A number of locations of the fault model were considered in order to compare the synthesized results with the attenuation relation equation for intra-slab earthquakes. Figure 18 shows the locations of the fault models numbered Nos 1–35.

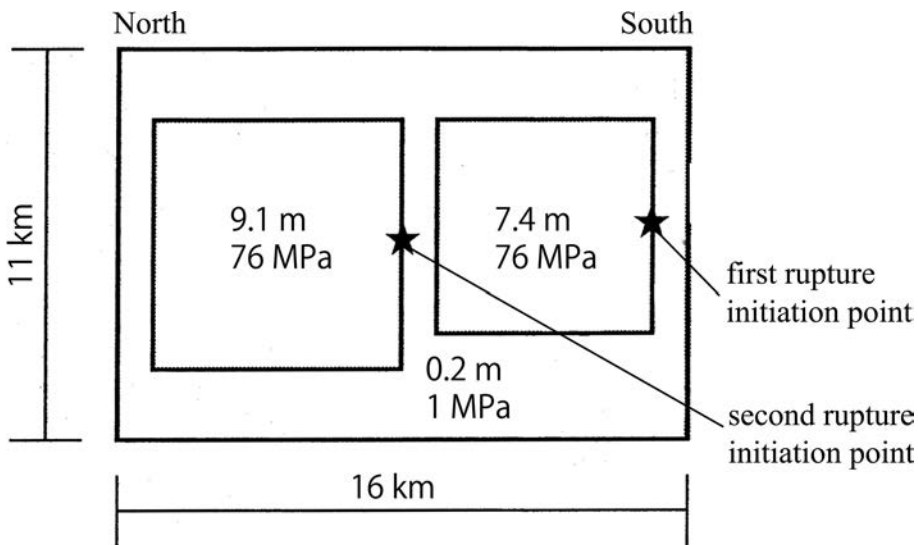


*FIG. 17. Example of an SMGA/asperity model with the averaged source characteristics of intra-slab earthquakes (reproduced from Ref. [57] with permission).*

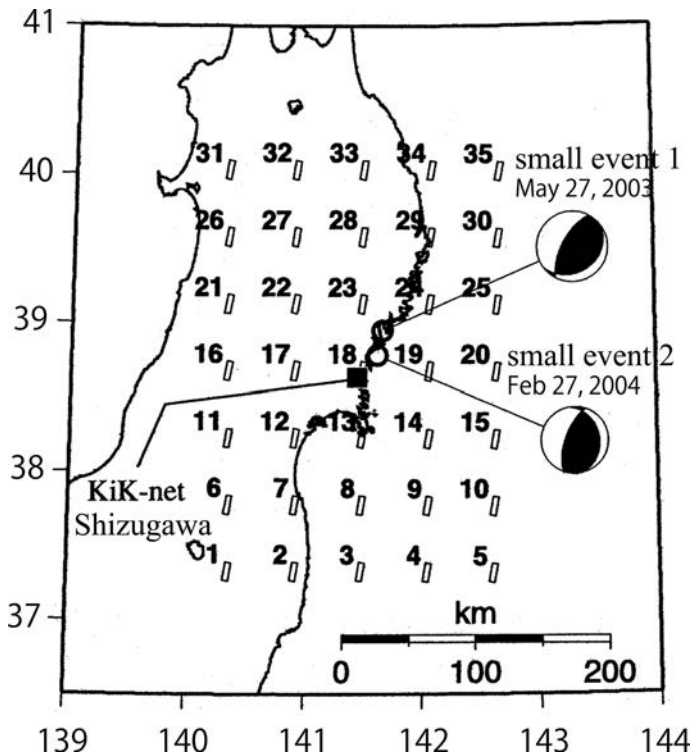
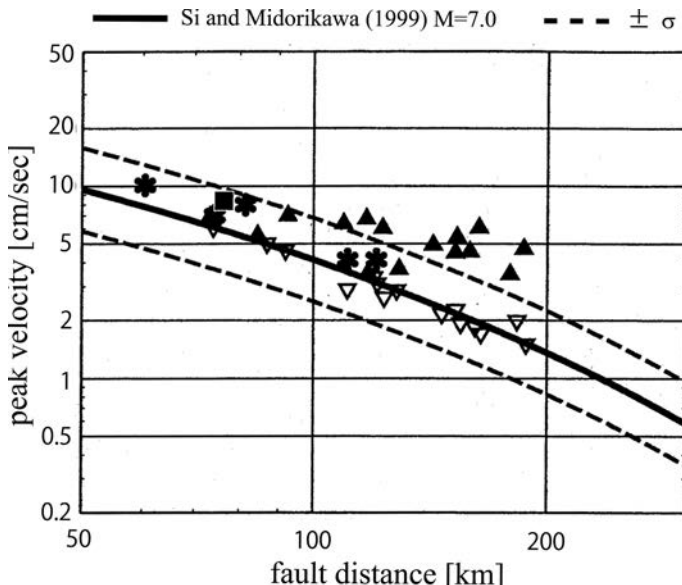


FIG. 18. Fault locations from Nos 1–35 for strong motion simulation (reproduced from Ref. [57] with permission).

Strong ground motion time histories were computed at the basement (GL=14 m) of KiK-net station Shizugawa by the empirical Green's function method [141]. Figure 19 compares the synthesized results and the GMPE of Ref. [5] modified based on the attenuation correction factor [142]. The solid triangles in Fig. 19 indicate larger ground motion caused by rupture directivity effects from faults Nos 1–15. It was found that the computed and observed peak velocities are slightly larger than that the ones predicted by the GMPE.

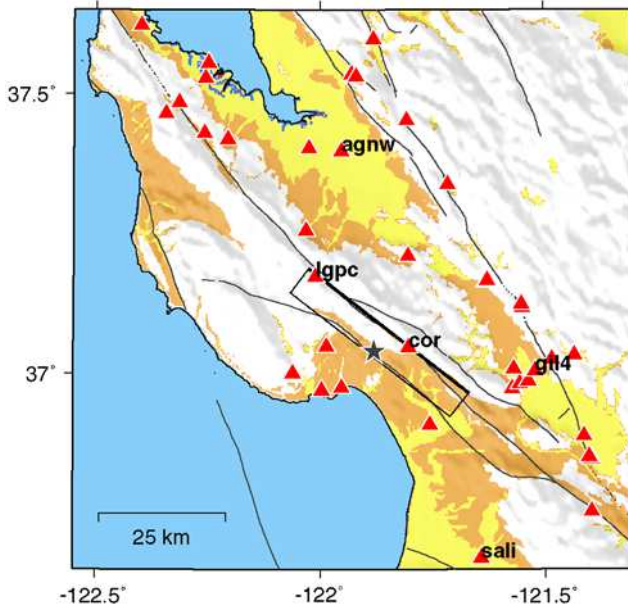


**Note:** ▲ = Nos 1–15, \* = Nos 16–20, ▽ = Nos 21–35, ■ = observed.

FIG. 19. Peak velocities of strong motions at the basement ( $GL - 14\text{ m}$ ) of KiK-net Shizugawa for the SMGA/asperity model in Fig. 14 (reproduced from Ref. [57] with permission).

#### 4.2. EXAMPLES OF GROUND MOTION EVALUATION BASED ON THE HYBRID METHOD

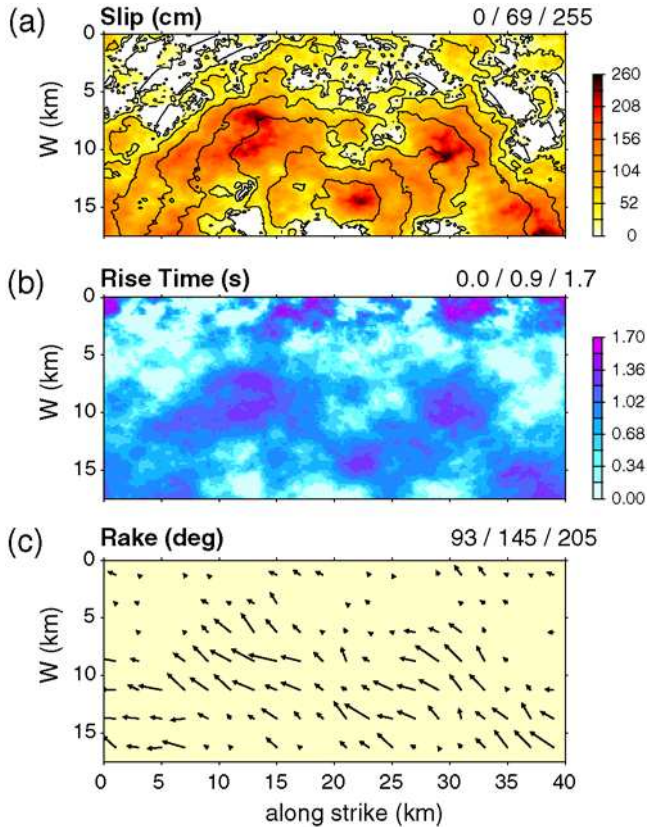
Graves and Pitarka [32] provided examples of the application of their hybrid model to the simulation of ground motions recorded in several earthquakes in 2010. As an example, results for the 1989 Loma Prieta, California, earthquake are introduced here. Figure 20 shows a projection of the fault rupture at surface and ground motion observation sites. The site conditions range from United States National Earthquake Hazard Reduction Program categories BC to D [11, 143].



**Note:** The rectangle indicates the surface projection of the fault with the heavy line denoting the top edge. The star is the epicentre and the triangles are recording stations analysed in the study. Generalized surface geology follows the classification of Wills et al. [143]: white contains classes B, BC, and C; dark shading is CD; and light shading is class D.

*FIG. 20. Map of the model region used for the Loma Prieta earthquake simulation [32] (courtesy of the Seismological Society of America).*

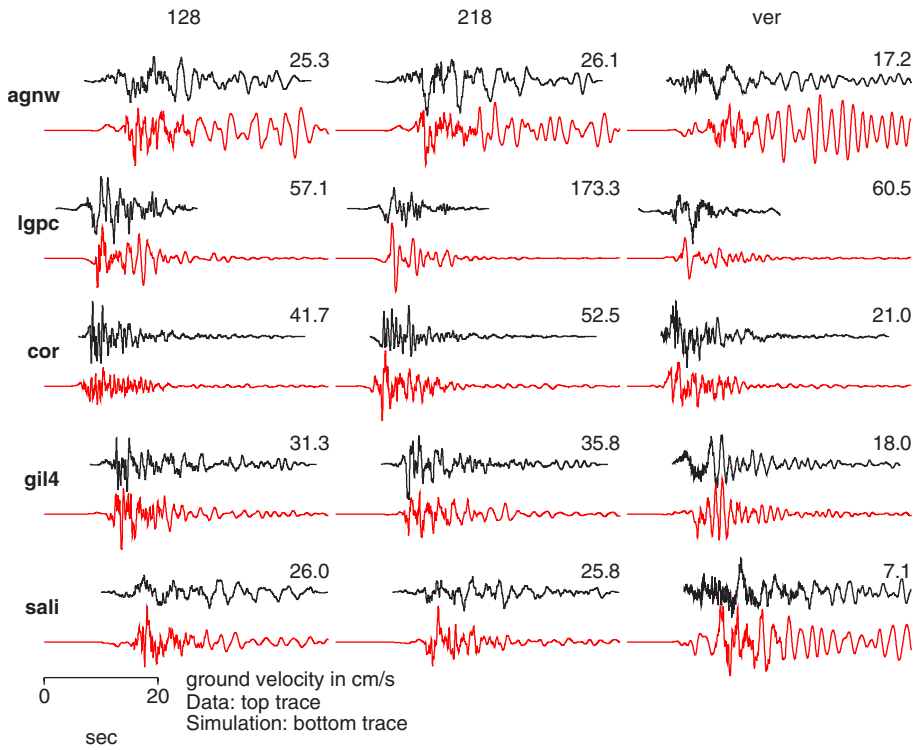
As shown in Fig. 21, the fault geometry and rupture initiation followed the model by Wald et al. [144] and the seismic moment of  $1.83 \times 10^{19}$  N·m was adopted. The 3-D Bay Area Velocity Model, by the United States Geological Survey (version 08.3.0), was used as basis for the simulation with a mid-crustal reflector. The Moho discontinuity and upper mantle structure were considered. For the low frequency component, the model was discretized with a grid size of 0.1 km intervals for the lowest shear wave velocity down to 0.5 km/s. For the high frequency component, the average 1-D velocity model near surface was evaluated from soil profiles of the individual observation stations to constrain  $V_s^{30}$  to 865 m/s.



**Note:** (a) Panel shows slip distribution with rupture front contours at 1 second intervals superimposed. (b) Panel shows distribution of slip rise time. (c) Panel shows distribution of rake. Triplet of numbers at top right of each panel indicates the minimum, mean and maximum values of the given distribution, respectively.

FIG. 21. Kinematic rupture model developed for the Loma Prieta earthquake [32] (courtesy of the Seismological Society of America).

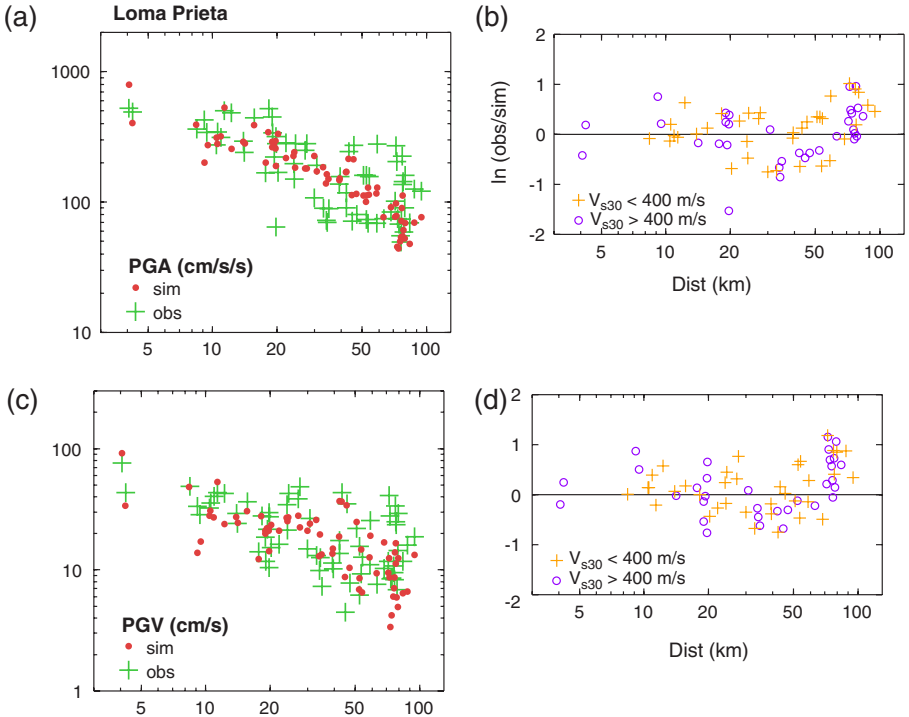
Comparison between the observed and simulated ground motions of velocity was indicated in Fig. 22 for the five sites mapped in Fig. 20. In the short distance from the fault ('lgpc' and 'cor' in Fig. 20), the duration of the motions can be short and pulse-like, particularly at 'lgpc', strong rupture directivity effect can be seen in the fault-normal ( $218^\circ$  azimuth) component. At 'cor', the nearest to the rupture initiation consist of rich high frequency phases with similar amplitude in both fault-normal and fault-parallel component. At 'agnw', 'gil4' and 'sali' (in Fig. 20), there are later phases that are also dominant in the observations with lower frequency components.



**Note:** Horizontal components have been rotated into fault parallel ( $128^\circ$  azimuth) and fault-normal ( $218^\circ$  azimuth).

*FIG. 22. Comparison of recorded (black) and simulated (red) broadband three component ground velocity waveforms at five selected sites for the Loma Prieta earthquake [32] (courtesy of the Seismological Society of America).*

The distribution of both simulated and observed peak ground accelerations and velocities were compared in Fig. 23 with the closest distance to the fault plane, and a fairly good prediction by the simulation can be seen. In order to evaluate effect of the near surface structure, the ratio between observed and simulated peak values were indicated above and below 400 m/s of  $V_s^{30}$ , respectively. Systematic trend beyond 60 km can be seen, where most of the sites are located around San Francisco and the simulation might underestimate the basin effect.



**Note:** Panels (a, c) show absolute ground motion values (recorded as crosses, simulated as circles) and panels (b, d) show the residuals of the recorded and simulated values in natural log units. For residuals, sites have been separated into two groups based on  $V_{s30}$ . PGA — peak ground acceleration PGV — peak ground velocity.

FIG. 23. Comparison of recorded and simulated PGA (a, b) and PGV (c, d) plotted as functions of closest distance to the fault surface for the Loma Prieta earthquake (c, d).

In the long distance area, simulated motions were underpredicted. As pointed out by previous studies (see Ref. [145]), larger amplitudes were observed in this area owing to the influence of Moho reflection of seismic wave propagation. Although the simulation took account of Moho reflections, ground structure model may have still some deficiencies, so that it did not reach the increase of 35% and 15% for peak ground acceleration and peak ground velocity, which had been estimated for the Moho reflections [146].

The bias of the simulation is evaluated by using a method of Abrahamson et al. [147] for nearby fault as shown in Fig. 9, in Section 3.3. The standard deviation for the spectral acceleration is in the range of around 0.5 in the natural logarithmic scale, which is equivalent to the bias of GMPEs.

#### 4.3. UNCERTAINTY IN GROUND MOTION PREDICTION USING FAULT RUPTURE MODELLING

A comprehensive representation of the uncertainty of the ground motion prediction is essential for the seismic hazard assessment. The parameters that need to be specified include the median value ( $\mu$ ) of the ground motion parameter, the scatter ( $\sigma$ ) about the median value, and the uncertainty in each of these two values ( $\sigma_\mu$  and  $\sigma_\sigma$ ). Two different types of uncertainty are used in different ways in seismic hazard analyses. Epistemic uncertainty is due to incomplete knowledge and data, and can in principle be reduced by the collection of additional information. Aleatory randomness is due to the inherently unpredictable nature of future events, and cannot be reduced. The total uncertainty can be evaluated by the combining epistemic and aleatory compositions. The epistemic uncertainty is usually represented by alternative branches on a logic tree, leading to alternative hazard curves, and affects the median hazard curve. Each hazard curve integrates over the aleatory component, which contributes to the uncertainty band about the hazard curve.

When fault rupture models are used to simulate ground motions, the total uncertainty is partitioned into modelling and parametric components that each contain epistemic and aleatory components [72]. The discrepancy between simplified modelling and the actual complicated process can be expressed as modelling uncertainty, whereas the discrepancy between the assumed model parameters and unknown accurate parameters for future earthquakes can be expressed as parametric uncertainty [147]. Parametric uncertainty represents the uncertainty in the values of the model parameters for future earthquakes [147]. The total uncertainty for the ground motion simulations can be evaluated by the combination of the modelling and parametric compositions. These two partitions of uncertainty are represented in matrix form in Table 3.

In the inversion of earthquake rupture models using strong motion and other data, strong correlations are usually found between the various source parameters such as rupture velocity and rise time. However, these parameters are often treated as being independent when the parametric uncertainty is estimated, causing overestimation of the parametric uncertainty.

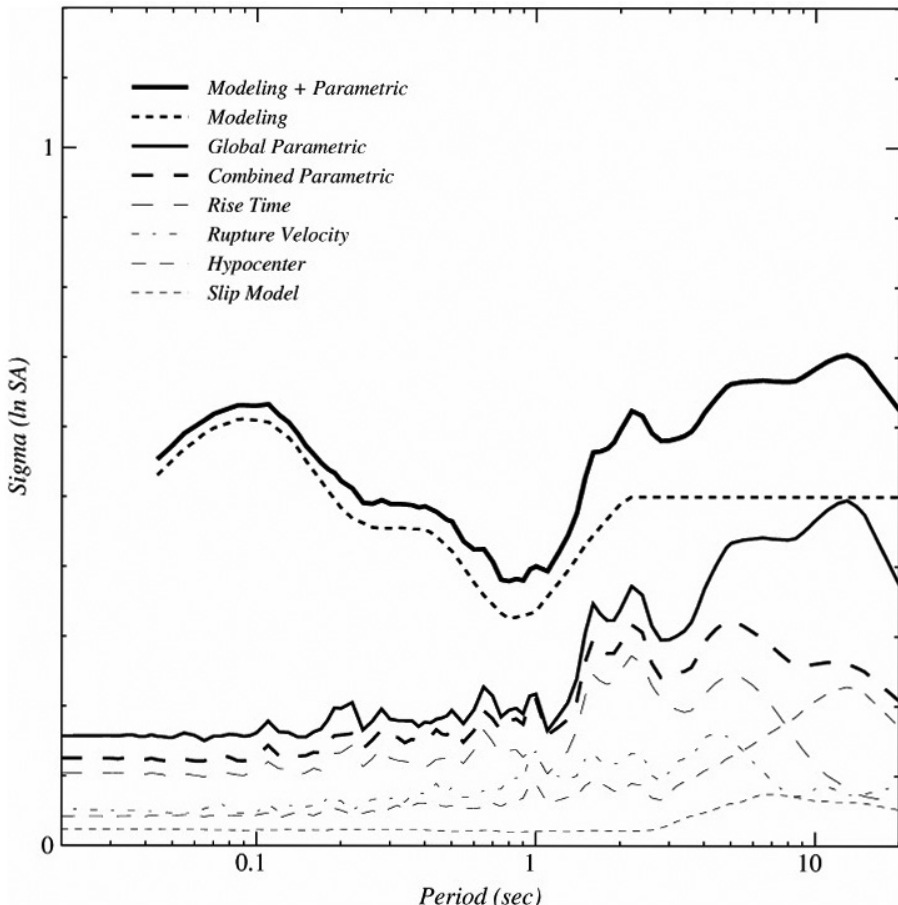
TABLE 3. PARTITION OF UNCERTAINTY IN GROUND MOTION PREDICTION MODELS

	Epistemic ( $\sigma_\mu, \sigma_\sigma$ )	Aleatory ( $\sigma$ )
Modelling	$\sigma_\mu$ : Uncertainty in the true bias of the model $\sigma_\sigma$ : Uncertainty in estimate of $\sigma_m$	$\sigma_m$ : Unexplained scatter due to physical processes not included in the model
Parametric	$\sigma_\mu$ : Uncertainty in median values of source and path parameters $\sigma_\sigma$ : Uncertainty in probability distributions of parameters	$\sigma_p$ : Event to event variation in source and path specific parameters of the model

**Source:** See Ref. [72].

As an example of total variability of prediction using the hybrid Green's function procedure, the variability for a magnitude 8 subduction earthquake is shown in Fig. 24 [148]. Four source parameters — slip distribution, hypocentre location (rupture initiation point), rupture velocity and rise time — are varied to estimate the parametric variability. The variability in the response spectrum due to each parameter was calculated with the other parameters fixed. The combined parametric variability is obtained by directly combining the variability arising from individual parameters, thus neglecting correlations between the effects of these four parameters. Global variability is derived from the whole set of simulations. The fact that global parametric variability is higher than the combined parametric variability suggests the presence of correlation between the effects of the four source parameters. The total variability of ground motion prediction is obtained by combining the modelling variability and the global parametric variability.

The partition of uncertainty between modelling and parametric uncertainty depends on the parameterization of the particular ground motion model being used. For example, if the stress drop is not a parameter of the model, then actual variations in ground motions due to differences in stress drops are included as an aleatory component of the modelling uncertainty. If the stress drop is a parameter in the model, then it can have both epistemic and aleatory components (i.e. uncertainty in the median stress drop of earthquakes, and the variability in stress drops about the median value).



**Note:** Also shown are the partial standard error due to parametric variability of slip model, hypocentre location, rupture velocity and rise time, and the combination of these standard errors assuming no correlation between them.

*FIG. 24. Overall standard error of hybrid Green's function simulation procedure (modelling + parametric), and its contributions from global parametric standard error and modelling standard error (reproduced from Ref. [148] with permission).*

In treating parametric uncertainty, some parameters can be evaluated accurately by detailed geological and seismological survey. Others need to be calculated from other parameters, and their uncertainty comes from the uncertainty in other parameters. Some examples of uncertainty treatment are described as follows. In the SMGA/asperity model, the seismic moment is evaluated from the fault area, as shown in Figs 30 and 31, in Appendix I. The

figures show that empirical relations between the seismic moment and the fault area are subject to a large amount of random variation. This should be taken into account in considering the uncertainty in the seismic moment.

The short period level is evaluated from the seismic moment, as shown in Fig. 32, in Appendix I. The figure shows that the empirical relation between seismic moment and the short period level also has a large amount of random variation. Cotton et al. [149] showed that a lognormal distribution of a stress drop with a sigma of 0.5 produced peak ground accelerations whose variance corresponds to the variance of the peak ground accelerations estimated by empirical GMPEs. Because their stress drop was the Brune's type stress drop [73], the short period level is proportional to the square of the cube root of the stress drop with the seismic moment preserved.

The location and number of the SMGAs/asperities can be estimated if the detailed slip distribution along the fault trace on the surface is well identified by geological survey [150]. However, it is generally difficult to know the detailed slip distribution along the fault trace on the surface, so various locations of the SMGAs/asperities should be assumed, including the vicinity of the site. Several locations of the rupture initiation point should be assumed when the location of the rupture initiation point cannot be identified.

#### 4.4. EXAMPLES OF UNCERTAINTY TREATMENT

This section describes examples of uncertainty treatment in the ground motion assessment for an actual nuclear power plant. Figure 25 shows various SMGA/asperity models for the Yokohama fault near Higashidori nuclear power plant in eastern Japan [151]. The length of the Yokohama fault is 15.4 km. Figure 25(a) shows a basic SMGA/asperity model of case 1, which describes one of the most probable fault rupture scenarios. Figure 25(b) shows an SMGA/asperity model of case 2 with a different rupture initiation point from that in case 1. Figures 25(c–e) show SMGA/asperity models of cases 3–5 with a different locations of the SMGA/asperity, a different stress drop (1.5 times larger) on the SMGA/asperity, and a different dip angle from those in case 1, respectively.

Figure 26 shows the simulated ground motions for the Yokohama fault [151]. The peak ground accelerations are 248.0, 204.0, 209.9, 297.6 and 243.2 Gal ( $= 1 \text{ cm/s}^2$ ) for cases 1–5, respectively. It was found that the largest influence comes from the different stress drop on the SMGA/asperity in this ground motion assessment.

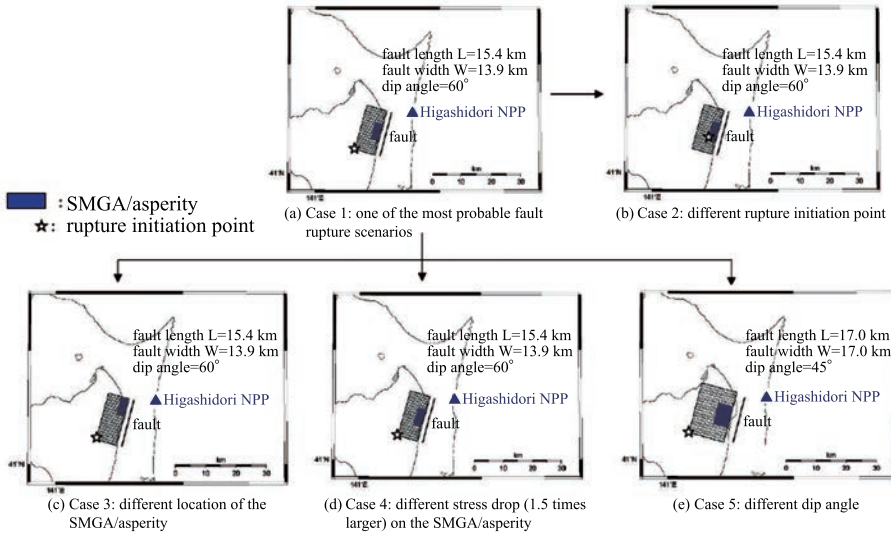


FIG. 25. Various SMGA/asperity models for the Yokohama active fault near Higashidori nuclear power plant in eastern Japan (reproduced from Ref. [151] with permission).

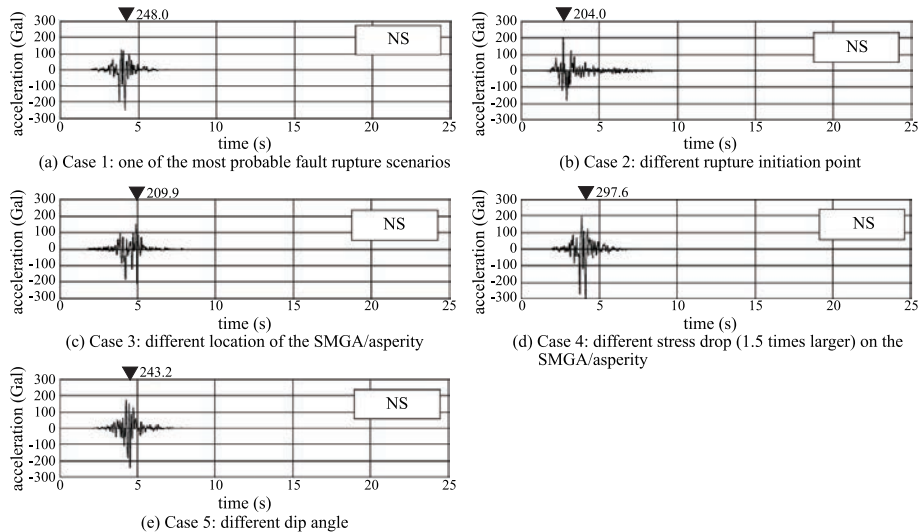


FIG. 26. Simulated ground motions for the Yokohama active fault near Higashidori nuclear power plant in eastern Japan (reproduced from Ref. [151] with permission).

## 5. CONCLUSIONS

This Safety Report explains the principles that underlay strong ground motion simulation, describes various methods for simulating strong ground motions, and shows some examples of ground motion simulations using two of these methods. The methodology and the examples in this report can be applied to fault rupture modelling for seismic hazard assessment in site evaluation for nuclear installations.

### 5.1. ADVANTAGES AND DISADVANTAGES OF DIFFERENT APPROACHES

The simplest seismologically based strong motion simulation method is the stochastic method [28]. The stochastic method is most appropriate at short periods (below around 1 second) where ground motions display stochastic characteristics. The stochastic method is used to simulate high frequency ground motions in broadband ground motion simulation procedures, including the asperity model and the hybrid model. At longer periods, the stochastic method generally produces ground motions that are deficient because some implementations of the stochastic method do not consider earthquake source properties (such as radiation pattern) and do not use Green's functions to describe seismic wave propagation, so the stochastic method is only suitable for high frequency.

The asperity model and hybrid model have several advantages over the stochastic method [152]:

“By using scaling relations for earthquake source parameters in conjunction with the elastodynamic representation theorem, the procedure can be used to construct ground motion time histories without resorting to assumptions about the shape of the source. The Green’s functions that are used in this procedure can be calculated from known crustal structure models, facilitating the use of the procedure in regions where recorded data are sparse or absent.”

However, these two methods require the specification of more source and wave propagation parameters than does the stochastic method. The composite source model also uses calculated Green’s functions and generates broadband ground motions.

## 5.2. ROLES OF GROUND MOTION SIMULATIONS AND GMPEs

There are two common uses of simulated ground motions in current nuclear installation engineering practice. First, they are used as input time histories for dynamic structural analysis, in which the modelling of non-linear response requires a time-domain approach. Second, they are used in the development of response spectral ground motion prediction models analogous to the GMPEs that are derived from recorded ground motions models. It is in this second area of application that the simulated spectral ground motions and GMPEs have overlapping roles.

In the second area, two practices are already applied in the seismic hazard evaluation for nuclear installations. The first case is the ground motion simulation at short distance from fault rupture of large seismic sources. In a high seismicity region such as Japan, the ground motion evaluation by empirical GMPEs are not reliable because the GMPEs are usually determined from observed ground motions and the number of observation in this region is not enough to determine the equations. Physical basis simulations may be better than the extrapolation of the GMPEs in this region. The second case is the use of the simulated ground motion to determine the GMPEs as the data, instead of the observed ground motion. In low seismicity regions, such as in Central and Eastern United States of America, the determination of the regional empirical GMPE is impossible with only sparse observed data. The simulated motions might represent the regional source and crustal characteristics for the determination of the GMPEs.

Recent GMPEs are also parameterized with rupture directivity effects, hanging wall effects, non-linear magnitude scaling and seismic wave propagation distinction (e.g. high and low  $Q$  zone, Moho reflection and deep basin effects), among others. However, they are constrained with still sparse observed data. The simulated ground motions have an advantage of the physical basis to evaluate these effects. On the contrary, the simulation may need calibration by comparing with the predicted motions by the empirical GMPEs (and/or the observed ground motions if applicable). Both schemes of the simulation and the GMPE have no controversial role and complement each other.

## **Appendix I**

### **ESTIMATION OF FAULT PARAMETERS FOR THE SMGA/ASPERITY MODEL**

This appendix explains how to estimate the fault parameters describing the SMGA/asperity model introduced in Section 3.2.2. Since the specific procedure coexist with the common procedures in evaluating the fault parameters for the crustal earthquakes, the subduction interface earthquakes and the intra-slab earthquakes, the estimation of the fault parameters is described for each earthquake category in the following sections. A detailed procedure for the SMGA/asperity model is explained by National Research Institute for Earth Science and Disaster Prevention [153].

#### **I.1. FAULT PARAMETERS FOR CRUSTAL EARTHQUAKES**

Figure 27 shows four steps in evaluating fault parameters of crustal earthquakes. The procedure is explained in the following.

##### **I.1.1. Estimation of identified faults**

The geometry of the surface traces of active faults are identified by geomorphological investigation, geological survey, geophysical investigation, seismological data and geodetic data. For ground motion prediction, a subsurface fault that combines the largest number of surfaces traces is assumed to be the largest identified fault, which is then divided into several segments, each of which has one or two SMGAs/asperities (see Fig. 28) [154]. Similar concepts are proposed by Sibson [155] and Wesnousky [156].

Since it is difficult to choose which segments rupture during the same earthquake, all possible combinations of rupture segments are assumed.

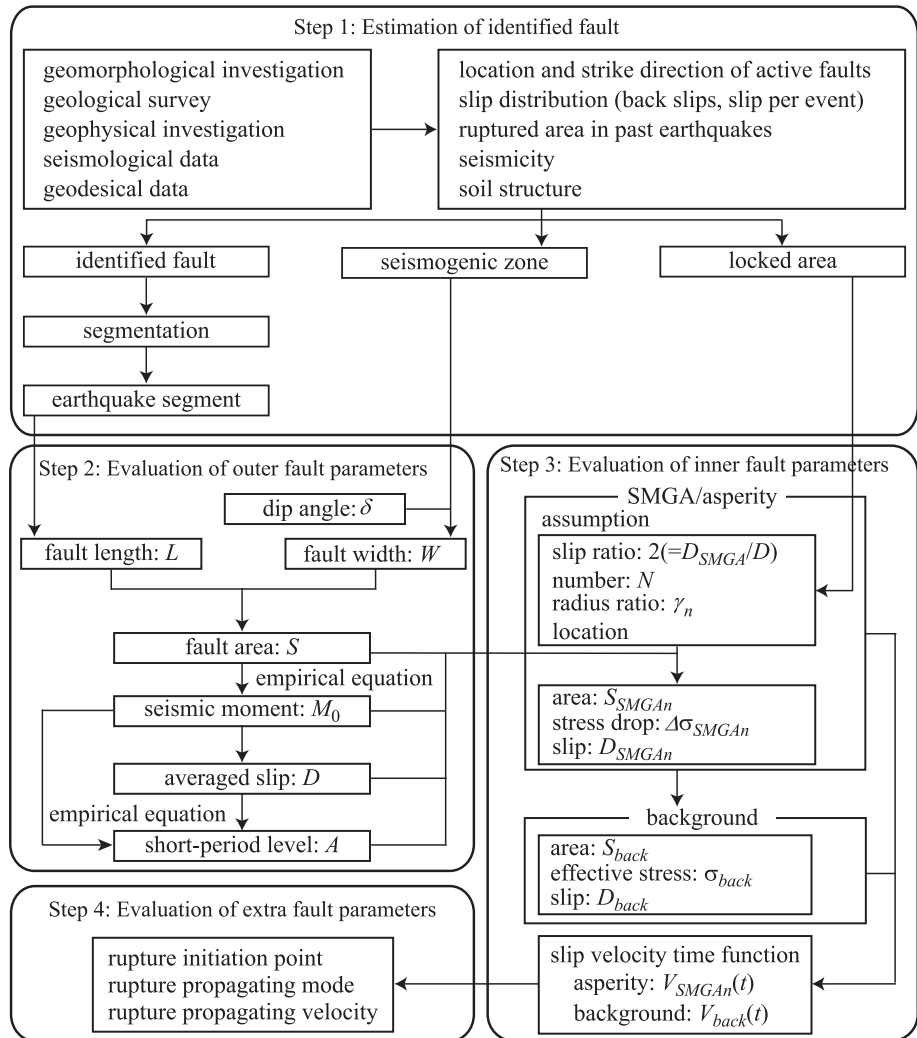
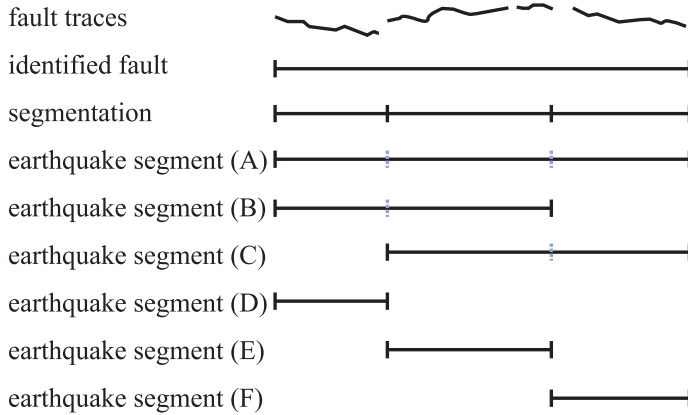


FIG. 27. Flow of evaluating fault parameters of the SMGA/asperity model for predicting strong ground motions from crustal earthquakes.



*FIG. 28. Relationship of fault traces on the surface explored by geological survey and earthquake segments in the seismogenic zone for predicting strong ground motions (reproduced from Ref. [154] with permission).*

### I.1.2. Evaluation of outer fault parameters

#### I.1.2.1. Fault length, width and depth

The fault length is evaluated from the geometry of the earthquake segments. The fault width is constant for larger earthquakes because it is assumed to be limited by the thickness of the seismogenic layer, as shown in Fig. 8, in Section 3.2.2.4. Irikura and Miyake [50] proposed the following relationship between the fault length  $L$  and the fault width  $W$  (see Fig. 29):

$$\begin{cases} W = L & (L < W_{\max}) \\ W = W_{\max} & (L \geq W_{\max}) \end{cases} \quad (10)$$

where

$$\begin{aligned} W_{\max} &= W_s / \sin \delta && \text{is the maximum value of the fault width;} \\ \delta & && \text{is the dip angle measured from the horizontal surface;} \\ W_s &= H_d - H_s && \text{is the thickness of the seismogenic zone;} \\ H_d & && \text{is the depth of the deepest part of the seismogenic zone;} \end{aligned}$$

and  $H_s$  is the depth of the shallowest part of the seismogenic zone, which is often determined by the depth distribution of micro-earthquakes or the velocity profile

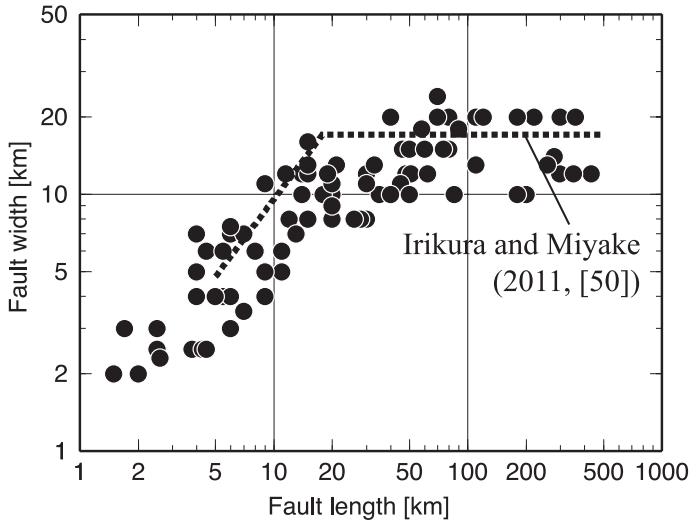


*FIG. 29. Fault length and width of crustal earthquakes.*

of the crust. The data in Fig. 29 are taken from Ref. [157] and are classified into two groups by two straight lines, while the data in Fig. 8, in Section 3.2.2.4, are classified into three groups by three straight lines for crustal earthquakes caused by strike-slip faults.

The fault model is confined to the seismogenic layer, and does not extend into the shallower layer because dynamic fault rupture simulation shows that little stress drop is observed in the upper several kilometres even though rupture occurs in it [158].

#### *I.I.2.2. Seismic moment and averaged slip*

The seismic moment is evaluated from the fault area by empirical equations. Figure 30 shows the following relationship between the seismic moment  $M_0$  and the fault area  $S$  proposed by Somerville et al. [35]:

$$S[\text{km}^2] = 2.23 \times 10^{-15} \times (M_0[\text{dyne} \cdot \text{cm}])^{2/3} \quad (11)$$

where  $10^7 \text{ dyne} \cdot \text{cm} = 1 \text{ N} \cdot \text{m}$ .

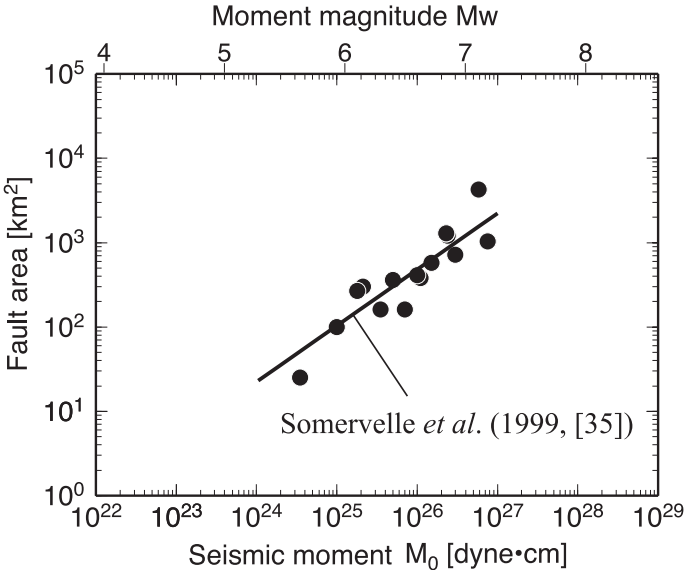


FIG. 30. Seismic moment and fault area of crustal earthquakes.

Empirical Eq. (11) was obtained from source inversion results of past large earthquakes, but the database did not include large earthquakes with the magnitude of around 8. More recently, Leonard [159] has developed self-similar relations that are similar to that found in Ref. [35].

The fault area is systematically smaller than that derived from Eq. (11) for larger earthquakes if the data of Abe [160] and Wells and Coppersmith [157] are included. Hence, the following empirical equation proposed by Irikura and Miyake [50], shown in Fig. 31, is adopted for larger earthquakes with larger areas:

$$S[\text{km}^2] = 4.24 \times 10^{-11} \times (M_0[\text{dyne}\cdot\text{cm}])^{1/2} \quad (12)$$

Empirical Eq. (12) can be applied to the range of the seismic moment between  $7.5 \times 10^{18}$  N·m to  $1.0 \times 10^{21}$  N·m, based on the data used in the analysis. Equation (12) cannot be applied to very large crustal earthquakes on very long faults. For very long faults, a new procedure for evaluating fault parameters has been developed by Dan et al. [161, 162].

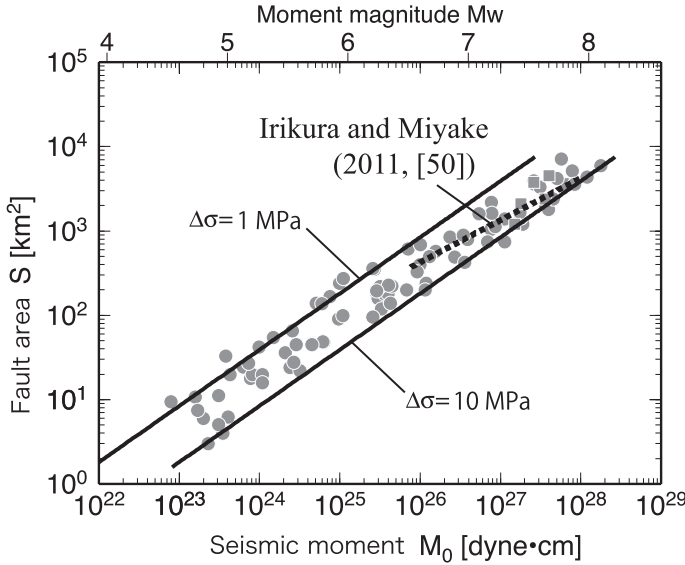


FIG. 31. Seismic moment and fault area of crustal earthquakes including larger earthquakes.

In the case that multiple segments rupture at once, the total seismic moment is evaluated by empirical Eqs (11) or (12) from the total area of the segments. The entire seismic moment is distributed to each segment by the following equation so that the averaged stress drop on each segment should be uniform:

$$M_{0i} = \frac{M_0 S_i^{1.5}}{\sum S_i^{1.5}} \quad (13)$$

where  $M_{0i}$  is the seismic moment of the  $i$ -th segment and  $S_i$  is the fault area of the  $i$ -th segment.

The average slip  $D$  is evaluated from the total seismic moment by:

$$D = \frac{M_0}{\mu S} \quad (14)$$

where  $\mu$  is the shear rigidity at the source.

### I.I.2.3. Short period spectral amplitude level

The short period spectral amplitude level  $A$  can be estimated from ground motion records on rock, which is not affected by the amplification of the surface layer, or from those at site where the amplification of the surface layer is evaluated quantitatively. In the case that the short period level cannot be estimated from records, it can be evaluated by the following empirical equation from the seismic moment proposed by Dan et al. [92] (see Fig. 32):

$$A[\text{dyne} \cdot \text{cm} / \text{s}^2] = 2.46 \times 10^{17} \times (M_0[\text{dyne} \cdot \text{cm}])^{1/3} \quad (15)$$

Similar empirical equations are proposed by Hanks and McGuire [84] and Atkinson and Hanks [163].

○ This study (Inland) ⋆ Papageorgiou (1988) □ Kamae (1997) ▽ Kamae (1990)  
 ● This study (Sea) ■ Kamae (1996) ◇ Irikura (1999) △ Kato-1 (1998)

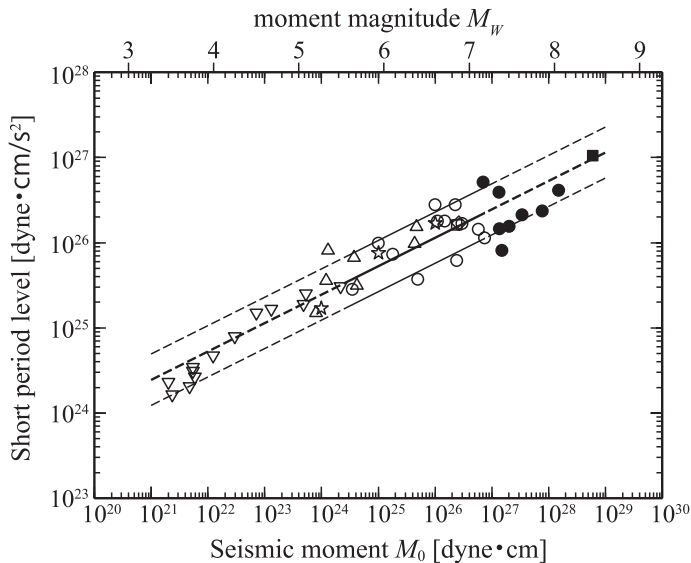


FIG. 32. Seismic moment and short-period level of crustal earthquakes, indicated by the open symbols, and subduction interface earthquakes, indicated by the solid symbols (reproduced from Ref. [92] with permission).

### I.1.3. Evaluation of inner fault parameters

#### I.1.3.1. Location and number of SMGAs/asperities

The location of the SMGA/asperity is one of the most important modelling parameters because the results of ground motion simulations are sensitive to the relative location of the SMGA/asperity and rupture initiation point. Sugiyama et al. [150] showed that the region where large slip was observed [164] corresponded to the location of the SMGAs/asperities on the fault [165]. Hence, if the detailed slip distribution along the fault trace on the surface is well known from geological surveys, it may be possible to estimate the location of the SMGAs/asperities. However, it is generally difficult to know the detailed slip distribution along the fault, so various locations of the SMGAs/asperities should be assumed, including ones in the vicinity of the site.

The average number of SMGA/asperities in an earthquake is around 2.6. It becomes larger as the size of the earthquake becomes larger, according to the compiled results of strong motion inversions for past crustal earthquakes [35]. For example, the 2000 Tottori, Japan, earthquake ( $M_w$  6.8) has two SMGAs/asperities, the 1995 Kobe, Japan, earthquake ( $M_w$  6.9) has three SMGAs/asperities, while the 1999 Kocaeli, Turkey, earthquake ( $M_w$  7.4) has five SMGAs/asperities, and the 1999 ChiChi, Taiwan, earthquake ( $M_w$  7.6) has six SMGAs/asperities [166, 167]. Based on these observations, one or two SMGAs/asperities are assumed in each segment.

#### I.1.3.2. Area of combined SMGAs/asperities

The area of combined SMGAs/asperities can be evaluated by the following equation, obtained from Eqs (2) and (3), in Section 3.2.2.4:

$$S_{\text{SMGA}} = \frac{16\pi\beta^4 S^2 \Delta\sigma^2}{A^2} \quad (16)$$

Studies have shown that the ratio of the area of the combined SMGAs/asperities to that of the entire fault is 22% [35] or 15–27% [167] in the crustal earthquakes. These values are not constraint condition for evaluating the area of the combined SMGAs/asperities, but are important indices. In the case that a segment has two SMGAs/asperities, the ratio of 16:6 can be applied to assigning the area to each SMGA/asperity [35].

### I.I.3.3. Average slip on SMGAs/asperities and that on background

The averaged slip on the SMGAs/asperities  $D_{\text{SMGA}}$  can be evaluated by the following equation from the averaged slip on the entire fault  $D$  obtained for the crustal earthquakes [35]:

$$D_{\text{SMGA}} = 2D \quad (17)$$

The average slip in the background can be evaluated from the seismic moment of the background  $M_{0\text{back}}$ , which is calculated from the total seismic moment  $M_0$  and the seismic moment of the SMGAs/asperities  $M_{0\text{SMGA}}$ , and the area of the background  $S_{\text{back}}$  as follows:

$$\begin{aligned} D_{\text{back}} &= \frac{M_{0\text{back}}}{\mu S_{\text{back}}} \\ M_{0\text{back}} &= M_0 - M_{0\text{SMGA}} \\ M_{0\text{SMGA}} &= \mu D_{\text{SMGA}} S_{\text{SMGA}} \end{aligned} \quad (18)$$

The average slip on each SMGAs/asperity  $D_{\text{SMGA}_n}$  can be evaluated by the following equation based on self-similarity:

$$D_{\text{SMGA}_n} = \left( \frac{\gamma_n}{\sum \gamma_n^3} \right) D_{\text{SMGA}} \quad (19)$$

where

$$\begin{aligned} \gamma_n &\quad \text{is } r_n/r; \\ r_n &= (S_{\text{SMGA}_n}/\pi)^{0.5} \quad \text{is the equivalent radius of the } n\text{-th SMGA/asperity;} \end{aligned}$$

and  $r = (S_{\text{SMGA}}/\pi)^{0.5}$  is the equivalent radius of the combined SMGAs/asperities.

If the average slip on the largest SMGA/asperity evaluated by Eq. (19) is not consistent with the slip obtained by trench exploration, the proportionality constant 2 in Eq. (17) should be re-examined.

#### 1.1.3.4. Stress drop on SMGAs/asperities and effective stress on background

The stress drop on the SMGAs/asperities can be evaluated by:

$$\Delta\sigma_{\text{SMGA}} = \frac{A^2}{16\pi\beta^4 S \Delta\sigma} \quad (20)$$

Equation (20) is obtained from Eqs (2) and (3), in Section 3.2.2.4. Dalguer et al. [168] showed that the effective stress on the SMGA/asperity  $\sigma_{\text{SMGA}}$  is almost the same as the stress drop on the SMGA/asperity  $\Delta\sigma_{\text{SMGA}}$ . In the case of multiple SMGAs/asperities, the stress drop on each SMGA/asperity is generally assumed to be constant, and equal to  $\Delta\sigma_{\text{SMGA}}$ .

Dan et al. [56] showed the following proportionality relationships and the approximate relationship:

- effective stress  $\propto$  slip velocity  $\propto \frac{\text{slip}}{\text{rise time}}$ ;
- rise time  $\approx \frac{\text{fault width}}{(2 \times \text{rupture velocity})}$ .

Based on these relationships, and when there is only one SMGAs/asperity in each fault segment, the effective stress in the background area  $\sigma_{\text{back}}$  can be evaluated by:

$$\sigma_{\text{back}} = \left( \frac{D_{\text{back}}}{W_{\text{back}}} \right) \left( \frac{D_{\text{SMGA}}}{W_{\text{SMGA}}} \right) \sigma_{\text{SMGA}} \quad (21)$$

When the number of the SMGAs/asperities in each fault segment is two or greater  $\sigma_{\text{back}}$  can be evaluated by:

$$\sigma_{\text{back}} = \left( \frac{D_{\text{back}}}{W_{\text{back}}} \right) \left( \frac{\pi^{1/2}}{D_{\text{SMGA}}} \right) r \sum \gamma_i^3 \sigma_{\text{SMGA}} \quad (22)$$

Here,  $W_{\text{SMGA}}$  is the width of the SMGA/asperity and  $W_{\text{back}}$  is the width of the background area.  $W_{\text{back}}$  is often assumed to be equal to the width of the entire fault  $W$ .

### I.I.3.5. $f_{max}$

It is known that ground motion acceleration spectra generally decrease at frequencies above a certain frequency called  $f_{max}$  [83, 169]. It is unclear whether  $f_{max}$  is caused by source or path effects. The value of 6 Hz in the 1995 Kobe, Japan, earthquake [170] is often adopted as  $f_{max}$ , and in the ground motion simulations for this earthquake is considered as a source effect. The validity of  $f_{max}$  value adopted in source modelling should be confirmed by actual records or empirical ground motion prediction models.

### I.I.3.6. Slip velocity time function

The slip velocity time function is proposed by Nakamura and Miyatake [94] based on the dynamic simulation of fault rupturing as follows:

$$V(t) = \begin{cases} \frac{2V_m}{t_d} t \left(1 - \frac{t}{2t_d}\right) & 0 < t \leq t_b \\ \frac{b}{\sqrt{t - \varepsilon}} & t_b < t \leq t_r \\ c - a_r(t - t_r) & t_r < t \leq t_s \\ 0 & t \leq 0, t_s < t \end{cases} \quad (23)$$

where

$$\begin{aligned} \varepsilon &= \frac{(5t_b - 6t_d)}{4(1 - t_d/t_b)} \\ b &= 2V_m \left( \frac{t_b}{t_d} \right) (t_b - \varepsilon)^{1/2} \left( 1 - \frac{t_b}{2t_d} \right) \\ c &= \frac{b}{(t_r - \varepsilon)^{1/2}} \\ a_r &= \frac{c}{t_s - t_r} \\ t_r : (t_s - t_r) &= 2 : 1 \end{aligned}$$

The three parameters of the peak velocity  $V_m$ , the time  $t_d$  from the beginning of the slip to the peak velocity, and the rise time  $t_r$  are evaluated by:

$$V_m = \frac{\Delta\sigma(2f_c W_{\text{SMGA}} V_r)^{1/2}}{\mu} \quad (24)$$

$$t_d \approx \frac{1}{\pi f_{\max}} \quad (25)$$

$$t_r \approx \frac{W}{2V_r} \quad (26)$$

Here,  $f_c$  is the corner frequency for the low pass filter, and it is assumed to be equivalent to  $f_{\max}$ .  $W_{\text{SMGA}}$  is the width of the SMGA/asperity,  $V_r$  is the rupture propagation velocity, and  $t_b$  is automatically calculated by using the final slip in Eq. (23). Figure 33 shows an example of the slip velocity time function [94]. Similar slip velocity time functions are proposed by Day [93] and Tinti et al. [96].

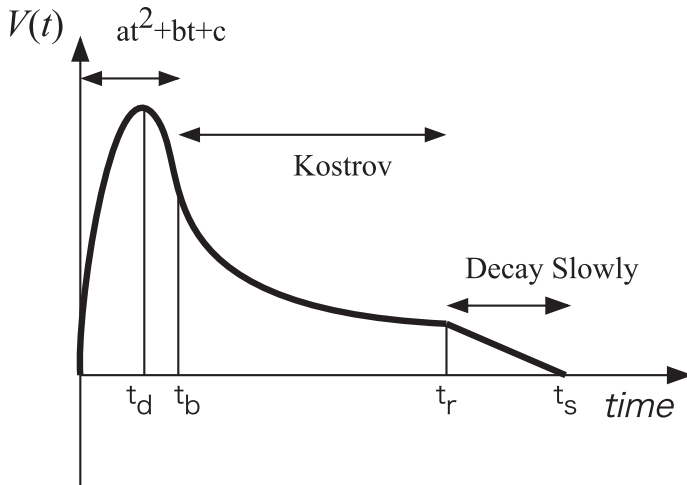


FIG. 33. Example of modelling of the slip velocity time function (reproduced from Ref. [94] with permission).

## I.1.4. Evaluation of extra fault parameters

### I.1.4.1. Rupture initiation point

Nakata et al. [98] showed typical examples in which branching points of strike-slip faults do not become rupture initiation points (see Fig. 34). For dip-slip faults, no specific relationships are found between the branching geometry and the rupture initiation point. Since the location of the rupture initiation point affects the predicted strong ground motions, several locations of the rupture initiation point should be assumed when the location of the rupture initiation point cannot be identified.

Somerville et al. [35] and Kikuchi and Yamanaka [171] showed the tendency for the rupture initiation point to be located away from asperities. Kikuchi and Yamanaka [171] also showed the tendency for the rupture to propagate from deeper to shallower parts of the fault in crustal strike-slip earthquakes. Mai et al. [172] concluded that hypocentres of crustal earthquakes are often located close to, but not within, asperities.

According to Kame et al. [173], branching of rupture from one fault to another can only occur under certain conditions. Poliakov et al. [174] showed that the propensity of the rupture path to follow a fault branch is determined by the pre-existing stress state, branch angle and incoming rupture velocity at the branch location. The predictions of the model by Kame et al. [173] used the following three parameters:

- $\psi$  is the angle between the direction of maximum compressive stress ( $S_{\max}$ ) and the fault strike;
- $\varphi$  is the angle between the main fault and the branch fault;
- $V_r$  is the rupture velocity (expressed as a fraction of the shear wave velocity).

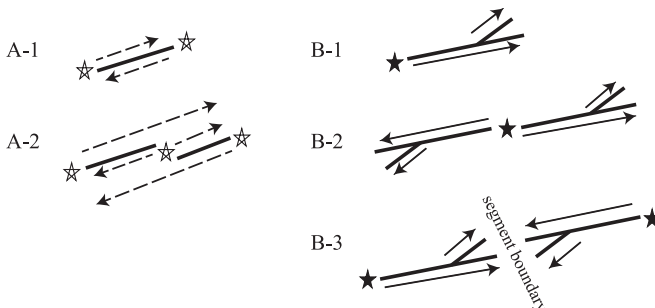
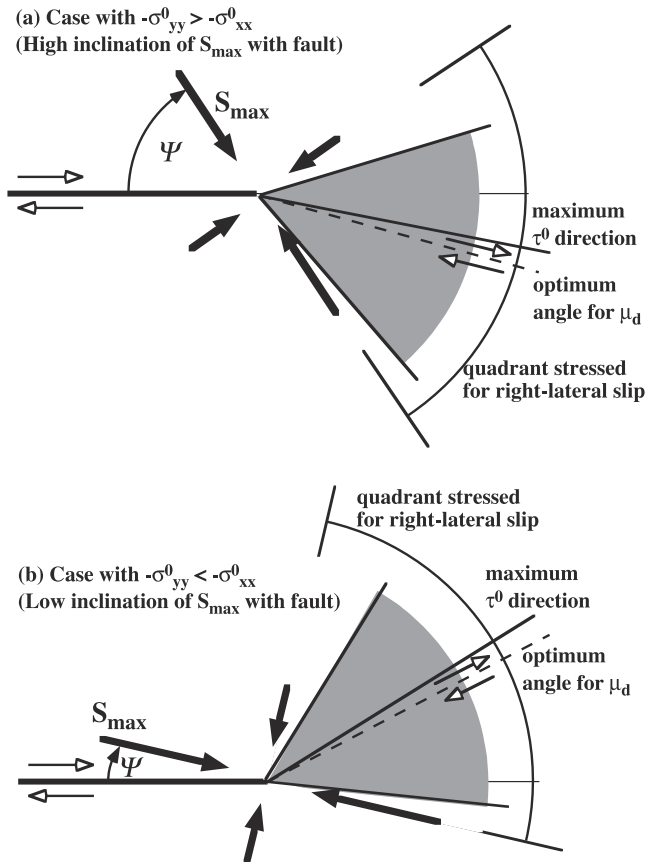


FIG. 34. Relationships of the branching geometry and the rupture initiation point in strike-slip faults (reproduced from Ref. [98] with permission).

As shown in Fig. 35, values of  $\psi > 45^\circ$  generally favour branch faulting on the extensional side of the main fault, while values of  $\psi < 45^\circ$  generally favour branch faulting on the compressional side of the main fault.



**Note:** (a) Fault normal precompression is dominant,  $\psi > 45^\circ$ , allowing rupture to continue along bend paths primarily to the extensional side. (b) Fault parallel precompression is dominant,  $\psi < 45^\circ$ , allowing rupture to continue along bend paths primarily to the compressional side. The grey zones indicate the angle range where the initial shear stress is larger than the frictional resistance.

FIG. 35. Qualitative prediction of the directions over which the larger scale prestress states favour right-lateral shear along bend paths (reproduced from Ref. [173] with permission).

#### *I.I.4.2. Rupture propagation mode*

The rupture propagation mode is defined from observations. Where such information does not exist, it is assumed to be radial from the rupture initiation point. When there are multiple rupture segments, the rupture front is often assumed to propagate from the point in each segment where the rupture front from the neighbouring fault segment arrives first. In the case when the neighbouring segments are separated, the rupture time delay can be evaluated using either the rupture propagation velocity in the two separated segments, or the shear wave velocity (reflecting shear strain propagation) of the material between the two segments.

#### *I.I.4.3. Rupture propagation velocity*

The rupture propagating velocity  $V_r$  is assumed to be 0.6–0.8 times the shear wave velocity if there are no direct measurements [175].

## **I.2. FAULT PARAMETERS FOR SUBDUCTION INTERFACE EARTHQUAKES**

Several procedures used for estimating the fault parameters of the SMGA/asperity model for crustal earthquakes can also be applied to subduction interface earthquakes. Hence, only the procedures that are different between crustal earthquakes and subduction interface earthquakes are explained in this section.

### **I.2.1. Estimation of identified faults**

The location and geometry of faults activated during subduction interface earthquakes are usually estimated from the plate boundaries and rupture zone of past earthquakes.

### **I.2.2. Estimation of outer fault parameters**

#### *I.2.2.1. Depth and fault area*

The estimated depth and fault area should be consistent with the plate boundary geometry and location of small earthquakes. Seismic faults estimated for the past earthquakes are also important information.

#### I.2.2.2. Seismic moment

The seismic moment can be evaluated from the assumed fault area. When data from past earthquakes are available, it is possible to develop a local relationship between the fault area and the seismic moment. In areas with scarce information empirical equations developed for other areas that relate fault area and magnitude [176] or fault area and seismic moment [177–180] are used. However, it is crucial to pay attention to the methodology used to estimate the fault area of earthquakes in the database.

#### I.2.3. Evaluation of inner fault parameters

It has been found that the location of asperities with large slip does not vary during repeated earthquakes. An example of such observation is shown in Fig. 36 [181]. Consequently, it may be possible to accurately locate the SMGAs/asperities of future earthquakes in regions with repeated earthquakes.

The back slip distribution on the plate boundary can be used to locate the SMGAs/asperities because the coupling rate is thought to be higher on the SMGAs/asperities than on the background. Here, the back slip is the amount of movement of the continental plate relative to the subducting oceanic plate during the period between earthquakes. This amount of movement is abruptly released during earthquakes. The coupling rate is the ratio of the velocity of the back slip to the velocity of the subducting oceanic plate.

The value of  $f_{\max}$  is uncertain for subduction interface earthquakes as well as for crustal earthquakes, and it is not clear whether it is attributable to a source effect or a site effect. An  $f_{\max}$  of 13.5 Hz [182] is often adopted as the source effect in recent examples of strong ground motion prediction.

#### I.2.4. Evaluation of extra fault parameters

When the location of the hypocentre of a past earthquake is available, the hypocentre may be considered as the rupture initiation point for the target earthquake in the same region. When the hypocentre of a past earthquake is not available, multiple hypocentre locations are used. Systematic features may be evident in some regions. For example, Kikuchi and Yamanaka [171] showed that the rupture propagation direction is shallow to deep in the Pacific coast of north-east Japan and deep to shallow in the Pacific coast of south-west Japan.

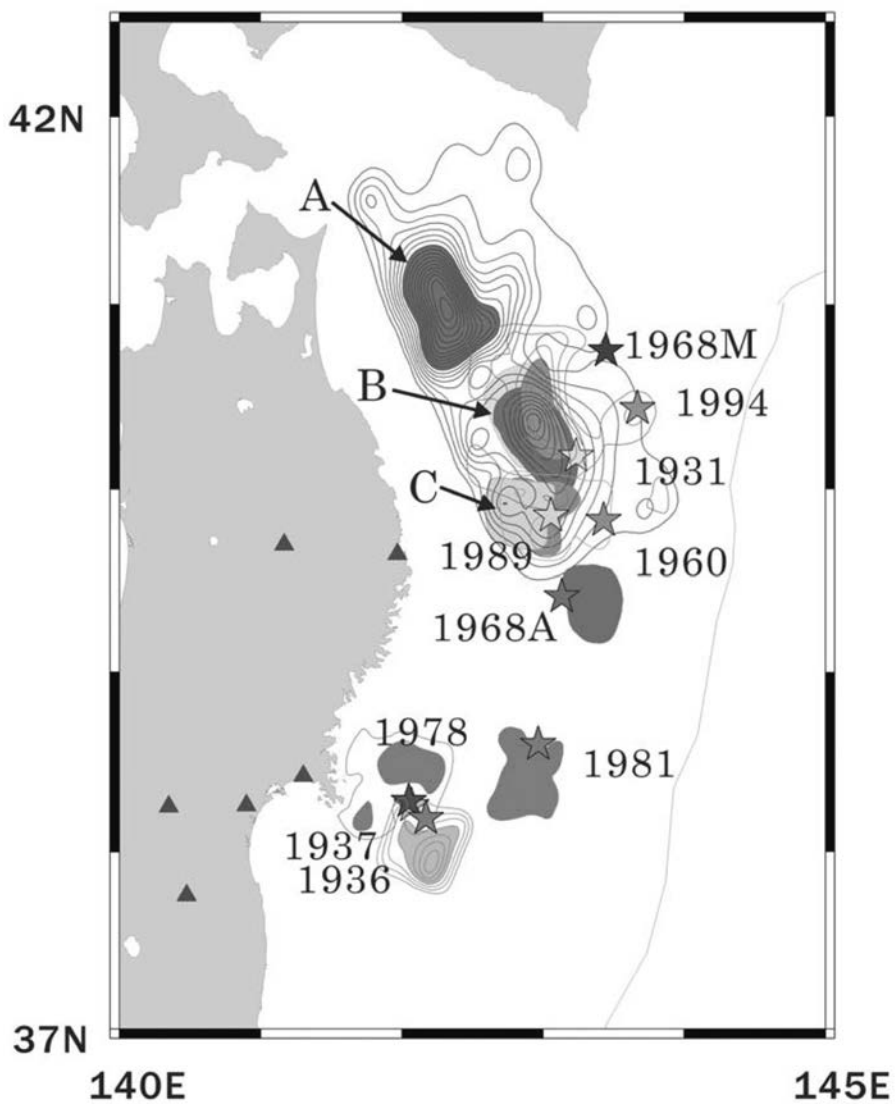


FIG. 36. Repeating rupture of the asperities with large slip in Sanriku-Oki, Japan, derived from source inversion (reproduced from Ref. [181] with permission).

### I.3. FAULT PARAMETERS FOR INTRA-SLAB EARTHQUAKES

Unlike the case for crustal and subduction earthquakes, the fault area for intra-slab earthquakes is not well known. Hence, the seismic moment is assumed a priori based on the information from past earthquakes in the region.

The area of the SMGAs/asperities  $S_{\text{SMGA}}$  and the short period level  $A$  are evaluated by empirical equations using seismic moment [183–187].

The corresponding empirical equations for calculating  $S_{\text{SMGA}}$  and  $A$  are:

$$S_{\text{SMGA}} [\text{km}^2] = 1.71 \times 10^{-16} \times (M_0 [\text{dyne} \cdot \text{cm}])^{2/3} \quad (27)$$

$$A [\text{dyne} \cdot \text{cm} / \text{s}^2] = 1.13 \times 10^{18} \times (M_0 [\text{dyne} \cdot \text{cm}])^{1/3} \quad (28)$$

Equation (27) is proposed by Asano et al. [188], using intra-slab earthquakes in the Pacific Plate and the Philippines Sea Plate. Equation (28) is obtained by Satoh [186] for intra-slab earthquakes in the Pacific Plate, off the Miyagi region.

The fault area  $S$ , the averaged stress drop  $\Delta\sigma$  and the stress drop in the SMGAs/asperities  $\Delta\sigma_{\text{SMGA}}$  are evaluated by:

$$S = \frac{49\pi^4 \beta^4 M_0^2}{16 S_{\text{SMGA}} A^2} \quad (29)$$

$$\Delta\sigma = \frac{4S_{\text{SMGA}}^{1.5} A^3}{49\pi^{4.5} \beta^6 M_0^2} \quad (30)$$

$$\Delta\sigma_{\text{SMGA}} = \frac{A}{4\beta^2 (\pi S_{\text{SMGA}})^{0.5}} \quad (31)$$

These equations are obtained from Eqs (1)–(3), in Section 3.2.2.4.

## Appendix II

### OPEN ACCESS TO THE SCEC BROADBAND SIMULATION PLATFORM

Several of the ground motion simulation methods described in this Safety Report have been implemented on the Southern California Earthquake Center (SCEC) Broadband Simulation Platform. Access to the platform is open to all users, who can perform validations of simulated ground motions against recorded ground motions for a set of past events, and simulations of scenario earthquakes, using methods of their choice. Details of how to access and use the Broadband Platform can be found on a collaborative SCEC web site, from which the following excerpt is taken.<sup>8</sup> However, for practical application, acquisition of deep knowledge about ground motion simulations is strongly encouraged.

“The goal of the SCEC Broadband Simulation Platform is to generate broadband (0–100 Hz) ground motions for earthquakes. The SCEC Broadband Platform is a collaborative software development project involving SCEC researchers, research engineers, graduate students, and the SCEC/CME software development group. SCEC scientific groups have contributed modules to the Broadband Platform including rupture generation, low- and high-frequency seismogram synthesis, non-linear site effects, and visualization. These complex scientific codes have been integrated into a system that supports easy on-demand computation of broadband seismograms. The SCEC Broadband Platform is designed to be used by both scientific and engineering researchers with some experience interpreting ground motion simulations.

“Users may calculate broadband seismograms for both historical earthquakes (validation events including Northridge and Loma Prieta) and user-defined earthquakes. The platform produces a variety of data products, including broadband seismograms, rupture visualizations, and several goodness-of-fit plots. Users can install the platform on their own machine, verify that it is installed correctly, and run their own simulations on demand without requiring knowledge of any of the code involved. Users may run a validation event, supply their own simple source description, or provide a rupture description in SRF format. Users may specify their

---

<sup>8</sup> See [http://scec.usc.edu/scecpedia/Broadband\\_Platform](http://scec.usc.edu/scecpedia/Broadband_Platform).

own list of stations or use a provided list. Currently the platform supports stations and events in Southern California, the Bay Area, the Mojave Desert, Eastern United States, Eastern Canada, Central and Western Japan. Users may select among various method that include rupture generation, low-frequency synthesis, high-frequency synthesis, and incorporation of site effects, with the option of running a goodness-of-fit comparison against observed or simulated seismograms. These codes have been validated against recorded ground motions from real events.

“The Broadband Platform was implemented using software development best practices, including version control, user documentation, acceptance tests, and formal releases, with the aim of ease of installation and use.”

## REFERENCES

- [1] INTERNATIONAL ATOMIC ENERGY AGENCY, Seismic Hazards in Site Evaluation for Nuclear Installations, IAEA Safety Standards Series No. SSG-9, IAEA, Vienna (2010).
- [2] US ARMY CORPS OF ENGINEERS, Selection of Design Earthquakes and Associated Ground Motions, EC 1110-2-6000, Department of the Army, Washington, DC (2009).
- [3] ABRAHAMSON, N., et al., Comparison of the NGA ground-motion relations, *Earthq. Spectra* **24** (2008) 45–66.
- [4] NODA, S., et al., “Response spectra for design purpose of stiff structures on rock sites” (OECD/NEA Workshop on the Relations Between Seismological Data and Seismic Engineering Analysis, Istanbul, 2002) 10.
- [5] SI, H., MIDORIKAWA, S., New attenuation relationships for peak ground acceleration and velocity considering effects of fault type and site condition, *J. Struct. Const. Eng. (Trans. Archit. Inst. Jpn.)* **523** (1999) 63–70 (in Japanese).
- [6] ABRAHAMSON, N., SILVA, W., Summary of the Abrahamson & Silva NGA ground-motion relations, *Earthq. Spectra* **24** (2008) 67–97.
- [7] BOORE, D.M., ATKINSON, G.M., Ground-motion prediction equations for the average horizontal component of PGA, PGV, and 5%-damped PSA at spectral periods between 0.01 s and 10.0 s, *Earthq. Spectra* **24** (2008) 99–138.
- [8] CAMPBELL, K.W., BOZORGNA, Y., NGA ground motion model for the geometric mean horizontal component of PGA, PGV, PGD and 5% damped linear elastic response spectra for periods ranging from 0.01 to 10 s, *Earthq. Spectra* **24** (2008) 139–171.
- [9] CHIOU, B.S.-J., YOUNGS, R.R., An NGA model for the average horizontal component of peak ground motion and response spectra, *Earthq. Spectra* **24** (2008) 173–215.
- [10] IDRISI, I.M., An NGA empirical model for estimating the horizontal spectral values generated by shallow crustal earthquakes, *Earthq. Spectra* **24** (2008) 217–242.
- [11] NEHRP CONSULTANTS JOINT VENTURE, Selecting and Scaling Earthquake Ground Motions for Performing Response-History Analyses, National Institute of Standards and Technology, Gaithersburg, MA (2011).
- [12] AKI, K., RICHARDS, P.G., Quantitative Seismology, Theory and Methods, Vols I and II, W.H. Freeman, San Francisco, CA (1980).
- [13] HELMBERGER, D.V., “Theory and application of synthetic seismograms”, *Earthquakes: Observation, Theory, and Interpretation*, Course LXXXV (KANAMORI, H., BOSCHI, E., Eds), Elsevier, Amsterdam (1983) 456–478.
- [14] SPUDICH, P., ARCHULETA, R.J., “Techniques for earthquake ground-motion calculation with applications to source parameterization of finite faults”, *Seismic Strong Motion Synthetics* (BOLT, B.A., Ed.), Academic Press, Orlando, FL (1987).
- [15] SATO, H., FEHLER, M.C., *Seismic Wave Propagation and Scattering in the Heterogeneous Earth*, Springer-Verlag, New York (1998).

- [16] HARTZELL, S., HARMSEN, S., FRANKEL, A., LARSEN, S., Calculation of broadband time histories of ground motion: Comparison of methods and validation using strong ground motion from the 1994 Northridge earthquake, *Bull. Seism. Soc. Am.* **89** (1999) 1484–1504.
- [17] GRAVES, R., PITARKA, A., COLLINS, N., SOMERVILLE, P., Goodness of Fit in Simulated Near-Fault Long Period Ground Motions, Final Report, PG&E-PEER Directed Studies Program, Phase II, URS Greiner Woodward Clyde, Pasadena, CA (1999).
- [18] SOMERVILLE, P.G., GRAVES, R.W., SAIKIA, C.K., Characterization of Ground Motions During the Northridge Earthquake of January 17, 1994: Program to Reduce the Earthquake Hazards of Steel Moment Frame Buildings, SAC Rep. 95-03, URS Greiner Woodward Clyde, Pasadena, CA (1995).
- [19] LIU, H., HELMBERGER, D.V., The 23:19 aftershock of the October 1979 Imperial Valley earthquake: More evidence for an asperity, *Bull. Seism. Soc. Am.* **75** (1985) 689–708.
- [20] STEWART, J.P., et al., Ground Motion Evaluation Procedures for Performance-Based Design, PEER Report No. 2001/09, Pacific Earthquake Engineering Research Center, Berkeley, CA (2001).
- [21] BOUCHON, M., A simple method to calculate Green's functions in elastic layered media, *Bull. Seism. Soc. Am.* **71** (1981) 959–971.
- [22] HISADA, Y., An efficient method for computing Green's functions for a layered half-space with sources and receivers at close depths (Part 2), *Bull. Seism. Soc. Am.* **85** (1995) 1080–1093.
- [23] GRAVES, R.W., Simulating seismic wave propagation in 3D elastic media using staggered-grid finite-differences, *Bull. Seism. Soc. Am.* **86** (1996) 1091–1107.
- [24] PITARKA, A., 3D elastic finite-difference modeling of seismic motion using staggered grids with nonuniform spacing, *Bull. Seism. Soc. Am.* **89** (1999) 54–68.
- [25] IRIKURA, K., “Prediction of strong acceleration motions using empirical Green's function”, Proceedings of the 7th Japan Earthquake Engineering Symposium (1986) 151–156.
- [26] DAN, K., WATANABE, T., TANAKA, T., SATO, R., Stability of earthquake ground motion synthesized by using different small-event records as empirical Green's functions, *Bull. Seism. Soc. Am.* **80** (1990) 1433–1455.
- [27] SOMERVILLE, P.G., Engineering applications of strong ground motion simulation, *Tectonophys.* **218** (1993) 195–219.
- [28] BOORE, D.M., Stochastic simulation of high-frequency ground motions based on seismological models of the radiated spectra, *Bull. Seism. Soc. Am.* **73** (1983) 1865–1894.
- [29] DAN, K., JU, D., MUTO, T., Modeling of subsurface fault for strong motion prediction inferred from short active fault observed on ground surface, *J. Struct. Const. Eng. (Trans. Archit. Inst. Jpn.)* **648** (2010) 279–288 (in Japanese).
- [30] SOMERVILLE, P., SAIKIA, C., WALD, D., GRAVES, R., Implications of the Northridge earthquake for strong ground motions from thrust faults, *Bull. Seism. Soc. Am.* **86** (1996) S115–S125.

- [31] GRAVES, R.W., PITARKA, A., “Broadband time history simulation using a hybrid approach” (Proc. 13th World Conf. Earthquake Engineering, Vancouver, 2004) Paper No. 1098.
- [32] GRAVES, R.W., PITARKA, A., Broadband ground-motion simulation using a hybrid approach, Bull. Seism. Soc. Am. **100** (2010) 2095–2123.
- [33] REID, H.F., The elastic-rebound theory of earthquake, Univ. Calif. Publ Geol. Sci. **6** (1911) 13–44.
- [34] BOLT, B.A., Earthquakes, W.H. Freeman, New York (1993).
- [35] SOMERVILLE, P.G., et al., Characterizing crustal earthquake slip models for the prediction of strong ground motion, Seism. Res. Lett. **70** (1999) 59–80.
- [36] SPUDICH, P., FRAZER, L.N., Use of ray theory to calculate high-frequency radiation from earthquake source having spatially variable rupture velocity and stress drop, Bull. Seism. Soc. Am. **74** (1984) 2061–2082.
- [37] HASKELL, N.A., Elastic displacements in the near-field of a propagating fault, Bull. Seism. Soc. Am. **59** (1969) 865–908.
- [38] BOORE, D.M., JOYNER, W.B., The influence of rupture incoherence on seismic directivity, Bull. Seism. Soc. Am. **68** (1978) 283–300.
- [39] HERRERO, A., BERNARD, P., A kinematic self-similar rupture process for earthquake, Bull. Seism. Soc. Am. **83** (1994) 1216–1228.
- [40] JOYNER, W., “Stochastic simulation of near-source earthquake ground motion”, Proceedings of Workshop on Modeling Earthquake Ground Motion at Close Distances, EPRI Rep. TR-104975, Electric Power Research Institute, Palo Alto, CA (1995).
- [41] ZENG, Y., ANDERSON, J.G., SU, F., Sub-event rake and random scattering effects in realistic strong ground motion simulation, Geophys. Res. Lett. **22** (1995) 17–20.
- [42] MAI, M.P., BEROZA, G.C., A spatial random field model to characterize complexity in earthquake slip, J. Geophys. Res. **107** (2002) 2308.
- [43] SCHOLZ, C.H., The Mechanics of Earthquakes and Faulting, Cambridge University Press, Cambridge (1990).
- [44] KANAMORI, H., “The nature of seismicity patterns before large earthquakes”, Earthquake Prediction (SIMPSON, D.W., RICHARDS, P.G., Eds), American Geophysical Union, Washington, DC (1981) 1–19.
- [45] LAY, T., KANAMORI, H., “An asperity model of large earthquake sequences”, Earthquake Prediction (SIMPSON, D.W., RICHARDS, P.G., Eds), American Geophysical Union, Washington, DC (1981) 579–592.
- [46] DAS, S., KOSTROV, B.V., “Fracture of a single asperity on a finite fault: A model for weak earthquakes?”, Earthquake Source Mechanics (DAS, S., BOATWRIGHT, J., SCHOLZ, C.H., Eds), American Geophysical Union, Washington, DC (1986) 91–96.
- [47] SOMERVILLE, P., et al., A study on empirical modeling of slip distribution on faults, Proc. 22nd JSCE Earthq. Eng. Symp. (1993) 291–294 (in Japanese).
- [48] MIYAKE, H., IWATA, T., IRIKURA, K., Estimation of rupture propagation direction and strong motion generation area from azimuth and distance dependence of source amplitude spectra, Geophys. Res. Lett. **28** (2001) 2727–2730.

- [49] MIYAKE, H., IWATA, T., IRIKURA, K., Source characterization for broadband ground-motion simulation: Kinematic heterogeneous source model and strong motion generation area, *Bull. Seism. Soc. Am.* **93** (2003) 2531–2545.
- [50] IRIKURA, K., MIYAKE, H., Recipe for predicting strong ground motion from crustal earthquake scenarios, *Pure Appl. Geophys.* **168** (2011) 85–104.
- [51] LAY, T., et al., Depth-varying rupture properties of subduction zone megathrust faults, *J. Geophys. Res.* **117** (2012).
- [52] WALD, D.J., HEATON, T.H., HELMBERGER, D.V., Rupture model of the 1989 Loma Prieta earthquake from the inversion of strong motion and broadband teleseismic data, *Bull. Seism. Soc. Am.* **81** (1991) 1540–1572.
- [53] SCHMEDES, J., ARCHULETA, R.J., LAVALLÉE, D., Correlation of earthquake source parameters inferred from dynamic rupture simulations, *J. Geophys. Res.* **115** (2010).
- [54] ZENG, Y., ANDERSON, J.G., YU, G., A composite source model for computing realistic synthetic strong ground motions, *Geophys. Res. Lett.* **21** (1994) 725–728.
- [55] IRIKURA, K., et al., “Recipe for predicting strong ground motion from future large earthquake” (Proc. 13th World Conf. Earthquake Engineering, Vancouver, 2004) Paper No. 1371.
- [56] DAN, K., SATO, T., IRIKURA, K., “Characterizing source model for strong motion prediction based on asperity model”, Proceedings of the 11th Japan Earthquake Engineering Symposium (2002) 555–560 (in Japanese).
- [57] DAN, K., MUTO, T., MIYAKOSHI, J., WATANABE, M., Characterized fault model for prediction of strong ground motions from intra-slab earthquakes, *J. Struct. Const. Eng. (Trans. Archit. Inst. Jpn.)* **600** (2006) 35–42 (in Japanese).
- [58] HEADQUARTERS OF EARTHQUAKE RESEARCH PROMOTION, On the strong ground motion assessment in the hypothetical earthquake caused by the faults of the west coast of the Lake Biwa (2004) (in Japanese).
- [59] IRIKURA, K., MIYAKE, H., Prediction of strong ground motions for scenario earthquakes, *J. Geogr.* **110** (2001) 849–875 (in Japanese).
- [60] IRIKURA, K., Recipe for predicting strong ground motion from future large earthquake, *Annu. Disaster Prev. Res. Inst.* **47A** (2004) 25–45 (in Japanese).
- [61] SOMERVILLE, P.G., SMITH, N.F., GRAVES, R.W., ABRAHAMSON, N.A., Modification of empirical strong ground motion attenuation relations to include the amplitude and duration effects of rupture directivity, *Seism. Res. Lett.* **68** (1997) 180–203.
- [62] SHAHI, S., BAKER, J.W., An empirically calibrated framework for including the effects of near-fault directivity in probabilistic seismic hazard analysis, *Bull. Seism. Soc. Am.* **101** (2011) 742–755.
- [63] MATSUSHIMA, S., KAWASE, H., Re-evaluation of strong motion and damage of wooden houses in Kobe city during the 1995 Kobe earthquake, *J. Struct. Eng.* **55B** (2006) 537–543 (in Japanese).
- [64] SILVA, W.J., LEE, K., State-of-the-Art for Assessing Earthquake Hazards in the United States, Report 24: WES RASCAL Code for Synthesizing Earthquake Ground Motions, Woodward-Clyde Consultants, Walnut Creek, CA (1987).

- [65] HELMBERGER, D., STEAD, R., HO-LIU, P., DREGER, D., Broadband modeling of regional seismograms; Imperial Valley to Pasadena, *Geophys. J. Int.* **110** (1992) 42–54.
- [66] OLSON, A.H., ORCUTT, J.A., FRAZIER, G.A., The discrete wavenumber/finite element method for synthetic seismograms, *J. R. Astron. Soc.* **77** (1984) 421–460.
- [67] LUCO, J.E., APSEL, J.J., On the Green's functions for a layered half-space, Part I, *Bull. Seism. Soc. Am.* **73** (1983) 909–929.
- [68] HARTZELL, S., Earthquake aftershocks as Green's functions, *Geophys. Res. Lett.* **5** (1978) 1–4.
- [69] HARTZELL, S., “The use of small earthquake as Green's functions”, Strong Motion Simulation and Earthquake Engineering Applications (SCHOLL, R.E., KING, J.L., Eds.), EERI Publication 85-02, Earthquake Engineering Research Institute, El Cerrito, CA (1985).
- [70] IRIKURA, K., Semi-empirical estimation of strong ground motions during large earthquakes, *Bull. Disaster Prev. Res. Inst.* **33** (1983) 63–104.
- [71] SOMERVILLE, P., “Seismic Hazard Evaluation” (Proc. 12th World Conf. Earthquake Engineering, Auckland, 2000) Paper No. 2833.
- [72] TORO, G.R., ABRAHAMSON, N.A., SCHNEIDER, J.F., Modeling of strong ground motions from earthquakes in Central and Eastern North America: Best estimates and uncertainties, *Seism. Res. Lett.* **68** (1997) 41–57.
- [73] BRUNE, J., Tectonic stress and the spectra of seismic shear waves from earthquakes, *J. Geophys. Res.* **75** (1970) 4997–5009.
- [74] BRUNE, J., Correction, *J. Geophys. Res.* **76** (1971) 5002.
- [75] ATKINSON, G.M., Attenuation of strong ground motion in Canada from a random vibration approach, *Bull. Seism. Soc. Am.* **74** (1984) 2629–2653.
- [76] SILVA, W.J., et al., “A methodology to estimate design response spectra in the near-source region of large earthquake using the band-limited-white noise ground motion model”, Proceedings of the Fourth US National Conference on Earthquake Engineering, Vol. 1, Earthquake Engineering Research Institute, El Cerrito, CA (1990) 487–494.
- [77] SILVA, W.J., CHIOU, S.J., SOMERVILLE, M., “Finite and point source RVT modeling”, Proceedings of Workshop on Modeling Earthquake Ground Motion at Close Distances, EPRI Report TR-104975, Electric Power Research Institute, Palo Alto, CA (1995).
- [78] SILVA, W.J., LI, S., DARRAGH, R., GREGOR, N., Surface geology based strong motion amplification factors for the San Francisco Bay and Los Angeles areas, Report to Pacific Earthquake Engineering Research Center (1999).
- [79] OU, G.B., HERRMANN, R., A statistical model for ground motion produced by earthquakes at local and regional distances, *Bull. Seism. Soc. Am.* **80** (1990) 1397–1417.
- [80] BOORE, D.M., SMSIM — Fortran Programs for Simulating Ground Motions from Earthquakes: Version 1.0, Open-File Report 96-80-A, United States Geological Survey, Menlo Park, CA (1996).
- [81] HOUGH, S.E., ANDERSON, J.G., High-frequency spectra observed at Anza, California: Implications for Q structure, *Bull. Seism. Soc. Am.* **78** (1988) 692–707.

- [82] SILVA, W.J., DARRAGH, R.B., “Engineering characterization of earthquake strong ground motion recorded at rock sites”, EPRI Report TR-102261, Electric Power Research Institute, Palo Alto, CA (1995).
- [83] HANKS, T.C., “ $f_{\max}$ ”, The Dynamic Characteristics of Faulting Inferred from Recordings of Strong Ground Motion (Proc. Workshop XVI), Open-File Report 82-591, Vol. II, United States Geological Survey, Menlo Park, CA (1982) 405–436.
- [84] HANKS, T.C., MCGUIRE, R.K., The character of high-frequency strong ground motion, Bull. Seism. Soc. Am. **71** (1981) 2071–2095.
- [85] SILVA, W.J., DARRAGH, R.B., GREEN, R.K., TURCOTTE, F.T., Estimated Ground Motions for a New Madrid Event, Misc. Paper GL-89-17, Woodward-Clyde Consultants, Oakland, CA (1989).
- [86] BERESNEV, I., ATKINSON, G., Stochastic finite fault modeling of ground motions from the 1994 Northridge, California earthquake, I. Validation on rock sites, Bull. Seism. Soc. Am. **88** (1998) 1392–1401.
- [87] BOORE, D.M., Comparing stochastic point-source and finite-source ground-motion simulations: SMSIM and EXSIM, Bull. Seism. Soc. Am. **99** (2009) 3202–3216.
- [88] ESHELBY, J.D., The determination of the elastic field of an ellipsoidal inclusion, and related problems, Proc. R. Soc. Lond. **241** (1957) 376–396.
- [89] FUJII, Y., MATSU'URA, M., Regional difference in scaling laws for large earthquakes and its tectonic implication, Pure Appl. Geophys. **157** (2000) 2283–2302.
- [90] DALGUER, L.A., MIYAKE, H., IRIKURA, K., “Characterization of dynamic asperity source models for simulating strong ground motions” (Proc. 13th World Conf. Earthquake Engineering, Vancouver, 2004) Paper No. 3286.
- [91] DALGUER, L.A., MIYAKE, H., DAY, S.M., IRIKURA, K., Surface rupturing and buried dynamic rupture models calibrated with statistical observations of past earthquakes, Bull. Seism. Soc. Am. **98** (2008) 1147–1161.
- [92] DAN, K., WATANABE, M., SATO, T., ISHII, T., Short period source spectra inferred from variable-slip rupture models and modeling of earthquake faults for strong motion prediction by semi-empirical method, J. Struct. Const. Eng. (Trans. Archit. Inst. Jpn.) **545** (2001) 51–62 (in Japanese).
- [93] DAY, S.M., Three-dimensional simulation of spontaneous rupture: The effect of nonuniform prestress, Bull. Seism. Soc. Am. **72** (1982) 1881–1902.
- [94] NAKAMURA, H., MIYATAKE, T., An approximate expression of slip velocity time function for simulation of near-field strong ground motion, J. Seismol. Soc. Jpn. **53** (2000) 1–9 (in Japanese).
- [95] GUATTERI, M., MAI, M.P., BEROZA, G., A pseudo-dynamic approximation to dynamic rupture models for strong ground motion prediction, Bull. Seism. Soc. Am. **94** (2004) 2051–2063.
- [96] TINTI, E., FUKUYAMA, E., PIATANESI, A., COCCO, M., A kinematic source-time function compatible with earthquake dynamics, Bull. Seism. Soc. Am. **95** (2005) 1211–1223.
- [97] LIU, P., ARCHULETA, R.J., HARTZELL, S.H., Prediction of broadband ground-motion time histories: Hybrid low/high-frequency method with correlated random source parameters, Bull. Seism. Soc. Am. **96** (2006) 2118–2130.

- [98] NAKATA, T., SHIMAZAKI, K., SUZUKI, Y., TSUKUDA, E., Fault branching and directivity of rupture propagation, *J. Geogr.* **107** (1998) 512–528 (in Japanese).
- [99] KAME, N., YAMASHITA, T., Dynamic branching, arresting of rupture and the seismic wave radiation in a self-chosen crack path modeling, *Geophys. J. Int.* **155** (2003) 1042–1050.
- [100] STARR, A.T., Slip in a crystal and rupture in a solid due to shear, *Proc. Camb. Philos. Soc.* **24** (1928) 489–500.
- [101] KNOPOFF, L., Energy release in earthquakes, *Geophys. J. R. Astron. Soc.* **1** (1958) 44–52.
- [102] SATO, R., *Handbook of Earthquake Fault Parameters in Japan*, Kajima Institute Publishing Co., Ltd, Tokyo (1989) (in Japanese).
- [103] MADARIAGA, R., On the relation between seismic moment and stress drop in the presence of stress and strength heterogeneity, *J. Geophys. Res.* **84** (1979) 2243–2250.
- [104] BOATWRIGHT, J., The seismic radiation from composite models of faulting, *Bull. Seism. Soc. Am.* **78**, (1988) 489–508.
- [105] MADARIAGA, R., High-frequency radiation from crack (stress drop) models of earthquake faulting, *Geophys. J. R. Astron. Soc.* **51** (1977) 625–651.
- [106] ITO, K., Seismogenic layer, reflective lower crust, surface heat flow and large inland earthquakes, *Tectonophys.* **306** (1999) 423–433.
- [107] WATANABE, M., DAN, K., SATO, T., “Scaling relations among macroscopic fault parameters”, *Summaries of Technical Papers of Annual Meeting*, B-2, Architectural Institute of Japan (2002) 117–118 (in Japanese).
- [108] PITARKA, A., SOMERVILLE, P.G., FUKUSHIMA, Y., UETAKE, T., IRIKURA, K., Simulation of near-fault ground motion using hybrid Green’s functions, *Bull. Seism. Soc. Am.* **90** (2000) 566–586.
- [109] DAY, S., BRADLEY, C., Memory efficient simulation of anelastic wave propagation, *Bull. Seism. Soc. Am.* **91** (2001) 520–531.
- [110] GUATTERI, M., MAI, P.M., BEROZA, G., BOATWRIGHT, J., Strong ground motion prediction from stochastic-dynamic source models, *Bull. Seism. Soc. Am.* **93** (2003) 301–313.
- [111] YAJI, Y., Source rupture process of the 2003 Tokachi-Oki earthquake determined by joint inversion of teleseismic body wave and strong ground motion data, *Earth, Planets and Space* **56** (2004) 311–316.
- [112] NI, S., SOMERVILLE, P., GRAVES, R., Ground Motion Simulations for the 1811 and 1812 New Madrid Earthquakes, Final Technical Report to the US Geological Survey G09AP00139, URS Group, Inc., Los Angeles, CA (2012).
- [113] FRANKEL, A., Simulating strong motions of large earthquakes using recordings of small earthquakes: The Loma Prieta mainshock as a test case, *Bull. Seism. Soc. Am.* **85** (1995) 1144–1160.
- [114] HARTZELL, S., HARMSEN, S., FRANKEL, A., LARSEN, S., Calculation of broadband time histories of ground motion: Comparison of methods and validation using strong ground motion from the 1994 Northridge earthquake, *Bull. Seism. Soc. Am.* **89** (1999) 1484–1504.

- [115] SOMERVILLE, P., NI, S., Earthquake Source and Ground Motion Characteristics in the Central and Eastern United States, Final Report No. G09AP00054, URS Group, Inc., Pasadena, CA (2010).
- [116] KAGAWA, T., IRIKURA, K., SOMERVILLE, P.G., Differences in ground motion and fault rupture process between the surface and buried rupture earthquakes, *Earth, Planets and Space* **56** (2004) 3–14.
- [117] SOMERVILLE, P.G., Magnitude scaling of the near fault rupture directivity pulse, *Phys. Earth and Planet. Inter.* **137** (2003) 201–212.
- [118] SOMERVILLE, P.G., PITARKA, A., “Differences in earthquake source and ground motion characteristics between surface and buried earthquakes” (8th Nat. Conf. Earthquake Engineering, San Francisco, 2006) Paper No. 977.
- [119] PITARKA, A., DALGUER, L.A., DAY, S.M., SOMERVILLE, P.G., DAN, K., Numerical study of ground-motion differences between buried rupturing and surface-rupturing earthquakes, *Bull. Seism. Soc. Am.* **99** (2009) 1521–1537.
- [120] SOMERVILLE, P.G., COLLINS, N., ABRAHAMSON, N., GRAVES, R., SAIKIA, C., Ground Motion Attenuation Relations for the Central and Eastern United States, Final Report No. 99HQGR0098, URS Group, Inc., Pasadena, CA (2001).
- [121] ATKINSON, G.M., BOORE, D.M., Earthquake ground-motion prediction equations for eastern North America, *Bull. Seism. Soc. Am.* **96** (2006) 2181–2205.
- [122] BOORE, D., JOYNER, W., Site amplification for generic rock sites, *Bull. Seism. Soc. Am.* **87** (1997) 327–341.
- [123] WALLING, M., SILVA, W., ABRAHAMSON, N., Non-linear site amplification factors for constraining the NGA models, *Earthq. Spectra* **24** (2008) 243–256.
- [124] KWOK, A.O., STEWART, J.P., Application of theoretical 1D amplification factors for evaluation of seismic site effects, *Bull. Seism. Soc. Am.* **96** (2006) 1422–1436.
- [125] MAI, P.M., IMPERATORI, W., OLSEN, K.B., Hybrid broadband ground-motion simulations: Combining long-period deterministic synthetics with high-frequency multiple S-to-S back-scattering, *Bull. Seism. Soc. Am.* **100** (2010) 2124–2142.
- [126] MENA, B., MAI, P.M., OLSEN, K.B., PURVANCE, M.D., BRUNE, J.N., Hybrid broadband ground motion simulation using scattering Green’s functions: Application to large magnitude events, *Bull. Seism. Soc. Am.* **100** (2010) 2143–2162.
- [127] ZENG, Y., A realistic synthetic Green’s function calculation using a combined deterministic and stochastic modeling approach, *EOS, Trans. Am. Geophys. Union* **76** (1995) F357.
- [128] ABRAHAMSON, N.A., SOMERVILLE, P.G., CORNELL, C.A., Uncertainty in numerical strong motion predictions, *Proc. 4th US Natl. Conf. Earthq. Eng.* **1** (1990) 407–416.
- [129] OLSEN, K.B., MAYHEW, J.E., Goodness-of-fit criteria for broadband synthetic seismograms, with application to the 2008 Mw5.4 Chino Hills, CA, earthquake, *Seismol. Res. Lett.* **81** (2010) 715–723.
- [130] SCHNEIDER, J.F., SILVA, W.J., STARK, C., Ground motion model for the 1989 M 6.9 Loma Prieta earthquake including effects of source, path, and site, *Earthq. Spectra* **9** (1993) 251–287.

- [131] SOMERVILLE, P.G., "Characterizing near fault ground motion for the design and evaluation of bridges" (3rd National Seismic Conf. and Workshop on Bridges and Highways, Portland, 2002).
- [132] ARCHULETA, R.J., HARTZELL, S.H., Effects of fault finiteness on near-source ground motion, *Bull. Seism. Soc. Am.* **71** (1981) 939–957.
- [133] MAVROEIDIS, G.P., PAPAGEORGIOU, A.S., A mathematical representation of near-fault ground motions, *Bull. Seism. Soc. Am.* **93** (2003) 1099–1131.
- [134] SPUDICH, P., et al., Final Report of the NGA-West2 Directivity Working Group, PEER 2013/09, Pacific Earthquake Engineering Research Center, Berkeley, CA (2013).
- [135] HEADQUARTERS OF EARTHQUAKE RESEARCH PROMOTION, Strong ground motion assessment in the hypothetical earthquake caused by the Itoigawa-Shizuoka Tectonic Line (Northern parts and central parts) (2002) (in Japanese).
- [136] HEADQUARTERS OF EARTHQUAKE RESEARCH PROMOTION, Strong ground motion assessment in the hypothetical Miyagi-Ken Oki earthquake (revised) (2005) (in Japanese).
- [137] DAN, K., WATANABE, M., SATO, T., MIYAKOSHI, J., SATOH, T., Isoseismal map of strong motions for the 1923 Kanto earthquake (MJMA 7.9) by stochastic Green's function method, *J. Struct. Const. Eng. (Trans. Archit. Inst. Jpn.)* **530** (2000) 53–62 (in Japanese).
- [138] DAN, K., HATA, N., MUTO, T., MIYAKOSHI, J., KANDA, J., "Probabilistic design earthquake ground motions considering scenario earthquakes, Part 3: Faulting scenario of the plate-boundary earthquakes off Miyagi Prefecture and strong ground motion simulation", Summaries of Technical Papers of Annual Meeting, Architectural Institute of Japan (2005) 97–98 (in Japanese).
- [139] TOHOKU ELECTRIC POWER COMPANY, Nuclear Regulation Authority Japan (2009) (in Japanese),  
[http://warp.da.ndl.go.jp/info:ndljp/pid/9394330/www.nsr.go.jp/archive/nsc/senmon/shidai/taishin\\_godo\\_WG1/taishin\\_godo\\_WG1\\_22/siryo4.pdf](http://warp.da.ndl.go.jp/info:ndljp/pid/9394330/www.nsr.go.jp/archive/nsc/senmon/shidai/taishin_godo_WG1/taishin_godo_WG1_22/siryo4.pdf)
- [140] WU, C., TSUTSUMI, H., SI, H., SAIJO, Y., "Rupture process of the 2011 Mw9.0 Tohoku earthquake and strong motion simulation from the viewpoint of NPP seismic design" (Proc. 15th World Conf. Earthquake Engineering, Lisbon 2012).
- [141] DAN, K., SATO, T., A semi-empirical method for simulating strong ground motions based on variable-slip rupture models for large earthquake, *Bull. Seism. Soc. Am.* **89** (1999) 36–53.
- [142] MORIKAWA, N., et al., Additional correction terms for attenuation relations corresponding to the anomalous seismic intensity in Northeast Japan, *J. Jpn. Assoc. Earthq. Eng.* **3** (2003) 14–26 (in Japanese).
- [143] WILLIS, C., et al., A site conditions map for California based on geology and shear wave velocity, *Bull. Seism. Soc. Am.* **90** (2000) S187–S208.
- [144] WALD, D.J., HEATON, T.H., HELMBERGER, D.V., Rupture model of the 1989 Loma Prieta earthquake from the inversion of strong motion and broadband teleseismic data, *Bull. Seism. Soc. Am.* **81** (1991) 1540–1572.

- [145] SOMERVILLE, P., YOSHIMURA, J., The influence of critical Moho reflections on strong ground motions recorded in San Francisco and Oakland during the 1989 Loma Prieta earthquake, *Geophys. Res. Lett.* **17** (1990) 1203–1306.
- [146] AAGAARD, B.T., et al., Ground motion modeling of the 1906 San Francisco earthquake I: Validation using the 1989 Loma Prieta earthquake, *Bull. Seism. Soc. Am.* **98** (2008) 989–1011.
- [147] ABRAHAMSON, N.A., SOMERVILLE, P.G., CORNELL, C.A., “Uncertainty in numerical strong motion predictions”, Proceedings of the Fourth US National Conference on Earthquake Engineering, Vol. 1, Earthquake Engineering Research Institute, El Cerrito, CA (1990) 407–416.
- [148] OTSUKA, H., SOMERVILLE, P.G., SATO, T., Estimation of broadband strong ground motions considering uncertainty of fault parameters, *JSCE J. Struct. Earthq. Eng.* **584** (1998) 185–200.
- [149] COTTON, F., ARCHULETA, R., CAUSSE, M., What is sigma of the stress drop? *Seism. Res. Lett.* **84** (2013) 42–48.
- [150] SUGIYAMA, Y., et al., “Application of active fault information to strong ground motion prediction”, The 31st Symposium of Earthquake Ground Motion, Architectural Institute of Japan (2003) 5–14 (in Japanese).
- [151] TOHOKU ELECTRIC POWER COMPANY, Nuclear Regulation Authority Japan (2010) (in Japanese),  
[http://warp.da.ndl.go.jp/info:ndljp/pid/9394330/www.nsr.go.jp/archive/nsc/senmon/shidai/taishin\\_godo\\_WG4/taishin\\_godo\\_WG4\\_40/siry06.pdf](http://warp.da.ndl.go.jp/info:ndljp/pid/9394330/www.nsr.go.jp/archive/nsc/senmon/shidai/taishin_godo_WG4/taishin_godo_WG4_40/siry06.pdf)
- [152] SOMERVILLE, P., MORIWAKI, Y., “Seismic hazards and risk assessment in engineering practice”, International Handbook of Earthquake & Engineering Seismology, Vol. 81, Part B (LEE, W.H.K., KANAMORI, H., JENNINGS, P.C., KISSLINGER, C., Eds), Elsevier Science (2003) 1065–1080.
- [153] NATIONAL RESEARCH INSTITUTE FOR EARTH SCIENCE AND DISASTER PREVENTION, Technical Reports on National Seismic Hazard Maps for Japan, Technical Note of the National Research Institute for Earth Science and Disaster Prevention No. 336, NIED, Tsukuba (2009).
- [154] DAN, K., “Problems in evaluating fault parameters for strong motion prediction based on the results of the geological survey”, Proceedings of the 3rd Annual Meeting of Japan Association for Earthquake Engineering (2005) 242–243 (in Japanese).
- [155] SIBSON, R.H., Stopping of earthquake ruptures at dilatational fault jogs, *Nature* **316** (1985) 248–251.
- [156] WESNOUSKY, S.G., Predicting the endpoints of earthquake ruptures, *Nature* **444** (2006) 358–360.
- [157] WELLS, D.L., COPPERSMITH, K.J., New empirical relationships among magnitude, rupture length, rupture width, rupture area, and surface displacement, *Bull. Seism. Soc. Am.* **84** (1994) 974–1002.
- [158] DALGUER, L.A., IRIKURA, K., RIERA, J., CHIU, H.C., Fault dynamic rupture simulation of the hypocentre area of the thrust fault of the 1999 Chi-Chi (Taiwan) earthquake, *Geophys. Res. Lett.* **28** (2001) 1327–1330.

- [159] LEONARD, M., Earthquake fault scaling: Self-consistent relating of rupture length, width, average displacement, and moment release, *Bull. Seism. Soc. Am.* **100** (2010) 1971–1988.
- [160] ABE, K., Seismological aspects of the Luzon, Philippines earthquake of July 16, 1990, *Bull. Earthq. Res. Instit.* **65** (1990) 851–873 (in Japanese).
- [161] DAN, K., JU, D., IRIE, K., ARZPEIMA, S., ISHII, Y., Estimation of averaged dynamic stress drops of inland earthquakes caused by long strike-slip faults and its application to asperity models for predicting strong ground motions, *J. Struct. Const. Eng. (Trans. Archit. Inst. Jpn.)* **670** (2011) 2041–2050 (in Japanese).
- [162] DAN, K., IRIE, K., JU, D., SHIMAZU, N., TORITA, H., Procedure for estimating parameters of fault models of inland earthquakes caused by long reverse faults, *J. Struct. Const. Eng. (Trans. Archit. Inst. Jpn.)* **707** (2015) 47–57 (in Japanese).
- [163] ATKINSON, G., HANKS, T., A high-frequency magnitude scale, *Bull. Seism. Soc. Am.* **85** (1995) 825–833.
- [164] LEE, Y., WU, W., SUGIYAMA, Y., AZUMA, T., KARIYA, Y., Displacements and segmentation of the surface fault, 1999 Chi-Chi, Taiwan, earthquake, *EOS Trans. Am. Geophys. Union* **81** (2000).
- [165] IWATA, T., SEKIGUCHI, H., PITARKA, A., Source and site effects on strong ground motions in near-source area during the 1999 Chi-Chi, Taiwan, earthquake, *EOS Trans. Am. Geophys. Union* **81** (2000).
- [166] IWATA, T., SEKIGUCHI, H., MIYAKOSHI, K., “Characterization of source processes of recent earthquake inverted from strong motion records in the dense network”, Proceedings of US–Japan Joint Workshop and Third Grantees Meeting for US–Japan Cooperative Research on Urban Earthquake Disaster Mitigation (2001) 53–59.
- [167] MIYAKOSHI, K., SEKIGUCHI, H., IWATA, T., “Extract of spatial heterogeneity of slips”, Study on Master Model of Strong Motion Prediction for Earthquake Disaster Mitigation (2001) 99–109 (in Japanese).
- [168] DALGUER, L.A., IRIKURA, K., ZHANG, W., RIERA, J.D., Distribution of dynamic and static stress changes during 2000 Tottori (Japan) earthquake: Brief interpretation of the earthquake sequences — Foreshocks, mainshock and aftershocks, *Geophys. Res. Lett.* **29** (2002).
- [169] ANDERSON, J.G., HOUGH, S.E., A model for the shape of the Fourier amplitude spectrum of acceleration at high frequencies, *Bull. Seism. Soc. Am.* **74** (1984) 1969–1993.
- [170] TSURUGI, M., KAGAWA, T., IRIKURA, K., KOWADA, A., “Cutoff frequency  $f_{\max}$  of earthquakes occurring in Kinki distinct”, Abstracts, Japan Earth and Planetary Science Joint Meeting (1997) 103 (in Japanese).
- [171] KIKUCHI, M., YAMANAKA, Y., Rupture process of the past large earthquakes = Identification of asperities, *SEISMO Hqrs Earthq. Res. Promot.* **5** (2001) 6–7 (in Japanese).
- [172] MAI, P., SPUDICH, P., BOATWRIGHT, J., Hypocenter locations in finite-source rupture models, *Bull. Seism. Soc. Am.* **95** (2005) 965–980.
- [173] KAME, N., RICE, J.R., DMOWSKA, R., Effects of prestress state and rupture velocity on dynamic fault branching, *J. Geophys. Res.* **108** (2003).

- [174] POLIAKOV, A.N.B., DMOWSKA, R., RICE, J.R., Dynamic shear rupture interactions with fault bends and off-axis secondary faulting, *J. Geophys. Res.* **107** (2002) 2295.
- [175] GELLER, R.J., Scaling relations for earthquake source parameters and magnitudes, *Bull. Seism. Soc. Am.* **66** (1976) 1501–1523.
- [176] UTSU, T., Seismology (Third Edition), Kyoritsu Shuppan Co. Ltd. (2001) (in Japanese).
- [177] YAMANAKA, Y., SHIMAZAKI, K., Scaling relationship between the number of aftershocks and the size of the main shock, *J. Phys. Earth* **38** (1990) 305–324.
- [178] IRIKURA, K., MIYAKE, H., IWATA, T., KAMAE, K., KAWABE, H., “Revised recipe for predicting strong ground motion and its validation”, Proceedings of the 11th Japan Earthquake Engineering Symposium (2002) 567–572 (in Japanese).
- [179] SOMERVILLE, P.G., SATO, T., ISHII, T., COLLINS, N.F., DAN, K., FUJIWARA, H., “Characterizing heterogeneous slip models for large subduction earthquakes for strong ground motion prediction”, Proceedings of the 11th Japan Earthquake Engineering Symposium (2002) 163–166 (in Japanese).
- [180] MUROTANI, S., MIYAKE, H., KOKETSU, K., Scaling of characterized slip models for plate-boundary earthquakes, *Earth, Planets and Space* **60** (2008) 987–991.
- [181] YAMANAKA, Y., KIKUCHI, M., Asperity map along the subduction zone in northeastern Japan inferred from regional seismic data, *J. Geophys. Res.* **109** (2004).
- [182] SATOH, T., KAWASE, H., SATO, T., Statistical spectral characteristics for engineering bedrock waves in which local site effects of surface geology are removed: Based on the ground motion records of small and medium earthquakes observed in the boreholes in Sendai, *J. Struct. Const. Eng. (Trans. Archit. Inst. Jpn.)* **462** (1994) 79–89 (in Japanese).
- [183] IWATA, T., SEKIGUCHI, H., MIYAKE, H., ASANO, K., “Extract and analysis of the heterogeneity characteristics of the source”, Study on Master Model of Strong Motion Prediction for Earthquake Disaster Mitigation (2002) 95–106 (in Japanese).
- [184] SATOH, T., Relation of stress drops of small and moderate earthquakes to focal mechanism, fault type, focal depths, and regions, *Jpn. Soc. Civ. Eng. J. Earthq. Eng.* (2003) CD-ROM (in Japanese).
- [185] SASATANI, T., MORIKAWA, N., MAEDA, T., “Intra-slab earthquakes: Source characteristics and strong motion prediction”, The 31st Symposium of Earthquake Ground Motion, Architectural Institute of Japan (2003) 17–22 (in Japanese).
- [186] SATOH, T., Short period spectral level of intraplate and interplate earthquakes occurring off Miyagi Prefecture, *J. Jpn. Assoc. Earthq. Eng.* **4** (2004) 1–4 (in Japanese).
- [187] ASANO, K., IWATA, T., IRIKURA, K., Source modeling and strong ground motion simulation of the off Miyagi intraslab earthquake of May 26, 2003, *J. Seismol. Soc. Jpn.* **57** (2004) 171–185 (in Japanese).
- [188] ASANO, K., IWATA, T., IRIKURA, K., Source characteristics of shallow intraslab earthquakes derived from strong-motion simulations, *Earth, Planets and Space* **55** (2003) e5–e8.

## **Annex**

### **FAULT DISPLACEMENT HAZARD ANALYSIS**

#### **A-1. INTRODUCTION**

This Annex provides procedures for assessing the fault displacement hazard analysis recommended in IAEA Safety Standards Series No. SSG-9, Seismic Hazards in Site Evaluation [A-1], using both scenario based (previously termed deterministic) and probabilistic approaches. In the scenario based approach, the hazard from a single earthquake scenario is considered. In scenario based hazard analysis, it is necessary to take account of the random variability in fault displacement for that scenario, which may be the median value (50th percentile) or a higher value such as the median plus one or two standard deviations (84th percentile and 95th percentile values, respectively). The earthquake scenario is usually chosen to represent the largest event that is expected to occur, regardless of how unlikely that is within the bounds described in para. 8.4 of SSG-9 [A-1]. These bounds may range from 1.8 million years (Upper Pleistocene) in tectonically active regions to as much as 5.3 million years (Pliocene) in tectonically stable regions.

If the scenario based approach is used, this may result in design criteria for fault displacement that are inconsistent with (and more conservative than) those for other hazards at the nuclear installations, depending on the percentile level chosen to represent the scenario. In the probabilistic approach for an identified fault, the hazard is calculated as a function of annual probability of exceedance. Unlike the case for probabilistic ground motion hazard, which is finite for even high annual probabilities of occurrence, fault displacement hazard is zero for annual probabilities that are higher than a value related to the inverse of the recurrence interval of the earthquake. It is therefore possible to have site at which the probabilistic fault displacement hazard on an identified fault at an annual probability of 1 in 1 million is zero, but the scenario based hazard is non-zero.

The focus of this Annex is on probabilistic fault displacement hazard analysis (PFDHA). The scenario based approach consists of selecting, from all of the possible earthquakes that are evaluated in the probabilistic approach, the earthquake event that produces the largest fault displacement at the site, using the relationships described in Section A-4.1. It may also be appropriate for the scenario based approach to consider the possibility of distributed faulting, described in Section A-4.2. Distributed faulting addresses the possibility

of faulting occurring off identified faults, on unidentified faults. In that sense, it is analogous to the ground shaking hazard from diffuse seismicity.

## A-2. PROBABILISTIC FAULT DISPLACEMENT HAZARD ANALYSIS

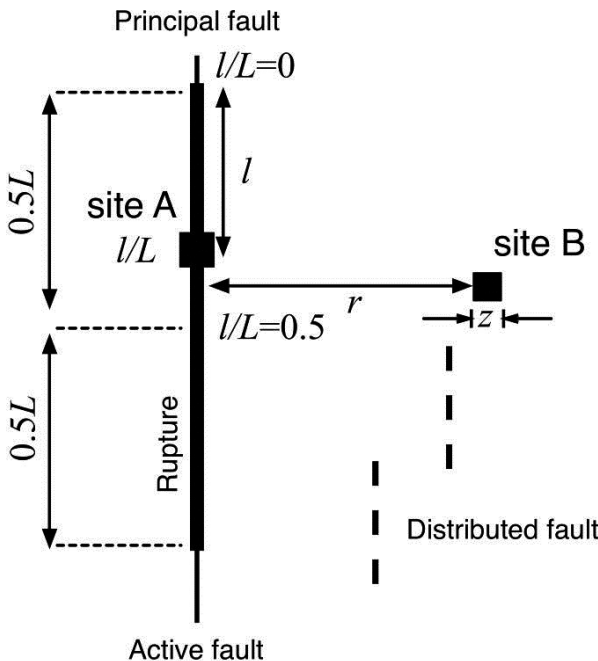
The work by Youngs et al. [A-2] in particular provides a comprehensive basis for modern PFDHA techniques. Scenario based analyses have also been conducted (see Ref. [A-3]), but these tend to overestimate the hazard in many cases, since they generally assume that the probability of fault rupture is 1 and either the average displacement or even the maximum displacement occur at any point along the fault. There are two basic approaches to PFDHA [A-2, A-4]:

- (1) Direct (or displacement) method: The probability of slip is directly related to the rate of displacement on a fault and a slip distribution function.
- (2) Earthquake method: In this method, the displacements are related to the occurrence of earthquakes through scaling relationships or slip distribution functions.

The framework closely follows the approach of probabilistic seismic hazard (PSHA), with the traditional attenuation relationships replaced by magnitude and position dependent slip distribution functions and the hazard computed through an integration over magnitude and rupture locations. Definitions of the variables used in PFDHA are given in Fig. A-1. According to Ref. [A-5]:

“The principal fault displacements are considered primary ruptures on the main, continuous faults that are located within several meters of the mapped fault. The distributed fault displacements are off the principal fault and are typically discontinuous ruptures or shears located tens of meters to a few kilometers from the principal fault trace.”

The inputs to PFDHA and the data needs are summarized in Table A-1. The principal and distributed fault displacements represent the net displacements.



**Note:**  $L$  is the length of surface rupture on principal fault;  $l$  is the distance on the surface rupture;  $r$  is the distance from the principal fault; and  $z$  is the dimension of the area considered for calculating the probability of fault rupture (area  $z^2$ ), respectively.

FIG. A-1. Definitions of variables used in the PFDHA [A-5].

TABLE A-1. INPUTS AND DATA NEEDED FOR THE PFDHA

Input to PFDHA	Data needed
Direct method	
Location of faults	Maps of faults
Frequency of displacement events based on slip rate and average displacement per event	Paleoseismic estimates of displacement per event Slip rates Total length of fault Cumulative displacement on fault Scaling relationships between fault slip and fault dimensions

TABLE A-1. INPUTS AND DATA NEEDED FOR THE PFDHA (cont.)

Input to PFDHA	Data needed
Probability of exceeding specific amounts of slip	Compilations of measured slip at sites with multiple ruptures Compilations of measured slip versus fault dimensions
Earthquake method (principal fault)	
Location of principal faults	Maps of active faults
Probability of principal surface rupture	Down dip geometry of faults Depth distribution of earthquakes Relationships between earthquake magnitude and rupture dimensions Frequency of surface rupture as function of magnitude
Slip distribution function	Mapped displacement profiles for surface rupturing earthquakes: maximum and average displacements Paleoseismic estimates of displacement per event Slip rates Paleoseismic recurrence intervals Total length of fault
Earthquake method (distributed fault)	
Location of principal faults	Maps of active faults
Probability of distributed rupture	Maps of distributed ruptures in historical earthquakes, as function of magnitude, style of faulting, distance from principal fault, hanging/foot wall
Slip distribution function	Measurements of the amplitude of distributed slip on individual ruptures indicating location with respect to the principal rupture

**Source:** Reproduced from Ref. [A-6] with permission.

### A-3. DIRECT METHOD

The frequency of displacement exceedance  $v(d)$  can be written as:

$$v(d) = \lambda_{DE} P(D > d) \quad (A-1)$$

where  $d$  is displacement,  $\lambda_{DE}$  is the rate of displacement events on the fault, and  $P(D > d)$  is the conditional probability that  $D$  in an event exceeds  $d$ .

This method forms a direct connection (hence its name) to the geological data from fault trench studies and other field observations. The rate of displacement events can simply be obtained by dating observed slip events. Alternatively, it can be computed simply as the slip rate divided by the average slip per event. The conditional probability of exceedance slip ( $P(D > d)$ ) can be obtained by measuring the amount of slip for many events at a site.

It is clear that this approach relies heavily on site specific information and rupture, but Youngs et al. [A-2] gave alternative methods to obtain the aforementioned functions, usually based on scaling relationships and normalized data from other faults. Although it seems that this would diminish the appeal of this method as one firmly based on local observations and make it more similar to the earthquake method described later. Angell et al. [A-7] presented a comprehensive example of this approach in a PFDHA analysis for submarine pipelines in the Gulf of Mexico, which included an extensive analysis of subsurface geophysical and geological data.

Braun [A-8] used this method to develop a PFDHA model for the Wasatch front using an extensive logic tree model and concluded that the results are strongly dependent on the choice of weights between the different branches, and thus that there is a strong sensitivity to epistemic uncertainties.

### A-4. EARTHQUAKE METHOD

The earthquake method closely follows the procedures developed for PSHA. In general, the equation for the exceedance rate for displacement

at a site on a fault,  $k(D > d)$  has the following form (see Ref. [A–2] for normal faulting; Ref. [A–5] for strike-slip faulting; Ref. [A–9] for reverse faulting; and Ref. [A–10] for strike-slip and reverse faulting in Japan):

$$k(D > d) = \sum_{m_j=m_0}^{m_u} \dot{N}(m_j) \left[ \sum_{k=1}^N P_r(D > d | r_k, m_j) \cdot P_r(sr \neq 0 | m_j) \cdot P_r(r_k | m_j) \right] \quad (\text{A-2})$$

where

- $\dot{N}(m_j)$  is the mean number of earthquakes of magnitude  $m_j$ ;
- $P_r(D > d | r_k, m_j)$  is the probability that displacement  $D$  exceeds  $d$  given that an earthquake of magnitude  $m_j$  centred at a distance  $r_k$  occurs;

and  $P_r(sr \neq 0 | m_j)$  the probability of surface rupture, given magnitude  $m$ . This term differs from the usual ground motion attenuation function. It is assumed in the PSHA that each earthquake produces “some level of ground shaking at site  $k$ ” [A–2].  $P_r(r_k | m_j)$  is the probability that an earthquake of magnitude  $m_j$  occurs with its centre of rupture located at  $r_k$ ;  $m_0$  is the minimum magnitude of earthquake engineering significance and  $m_u$  is the maximum magnitude for earthquake event considered.

In the setting of the surface rupture on the fault, Petersen et al. [A–5] distinguished the surface rupture from the fault (see Fig. A–1, in Section A–2). Takao et al. [A–10] applied the rupture segments apart from the fault according to the magnitude. The other differences between many of the papers are in the forms of  $P_r(D > d | r_k, m_j)$  and  $P_r(sr \neq 0 | m_j)$  from Eq. (A–2). Researchers have proposed beta or gamma models for the distribution of displacement along faults. For the Petersen et al. [A–5] model (see also Ref. [A–11]), functional forms were used. Petersen et al. [A–5] also addressed the uncertainties in the location of the actual trace of the fault (“mapping error”).

## A–4.1. Principal fault

### A–4.1.1. Probability of surface rupture

The probability that surface rupture ( $sr$ ) occurs for a given magnitude is given as:

$$P_r(sr \neq 0 | m_j) = \frac{e^{a+bm}}{(1+e^{a+bm})} \quad (\text{A-3})$$

with

$a = -12.51$  and  $b = 2.053$  for all slip types (these coefficients were applied in Refs [A–5, A–12]);

$a = -7.3$  and  $b = 1.03$  for a reverse fault [A–9];

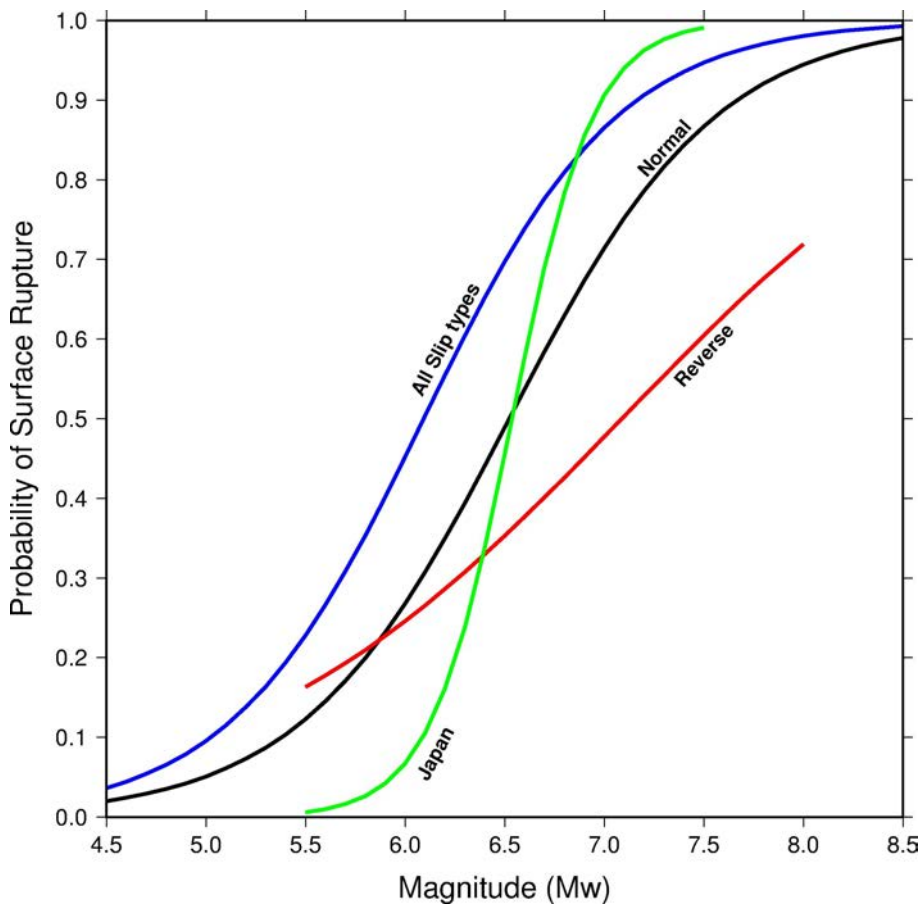
and  $a = -32.03$  and  $b = 4.90$  for a Japanese fault [A–10] (see Fig. A–2). Thus, the probability of surface rupture for a reverse earthquake at magnitude 7.0 is only 0.48, compared to 0.86 for all slip types. Takao et al. [A–10] indicated less fault type dependency for probability in the Japanese case. However, the probability curve of Japan is consistent with the evaluation of diffuse seismicity in Japan. This factor plays an important role in reducing the probabilistic hazard relative to the deterministic hazard.

Some authors (e.g. Abrahamson [A–13]) divided this function in two: one for the probability of surface rupture for the entire earthquake; and one for the probability of surface rupture reaching the site. The latter is sometimes inherently included in the previous term (slip distribution) and the integration process.

### A–4.1.2. Probability of slip exceedance

As stated in Ref. [A–2], the “conditional probability of exceedance represents the probability that at a specific point  $k$  on a rupture the fault displacement exceeds  $d$ .” Given that slip occurs, it “can be assessed using models built on empirical data, much as ground motion attenuation relationships are constructed.”

The displacement for a rupture is not uniform over the entire rupture, but instead tapers towards both ends of the rupture, and is parameterized using the ratio  $l/L$  between the total rupture length ( $L$ ) and the distance from the centre of the rupture to the point on the rupture closest to the site (see Fig. A–1, in Section A–2).



**Note:** Coloured solid lines indicate fitted function of each fault mechanism: normal [A-2]; all slip types [A-12]; reverse [A-9]; and Japan [A-10].

FIG. A-2. Probability of surface rupture.

Slip distributions are determined from two probability distributions: a distribution representing the spatial variability of slip along a fault and a distribution representing the average ( $D_{\text{ave}}$ ) or maximum displacement ( $D_{\text{max}}$ ). Displacement values are normalized by either the average displacement ( $D_{\text{ave}}$ ) or the maximum displacement ( $D_{\text{max}}$ ), which are estimated by applying the Wells and Coppersmith equation [A-14]. The probability of slip exceedance is obtained by convolving the distributions for displacements normalized by the maximum displacement ( $D/D_{\text{max}}$ ) or displacements normalized by the average displacement ( $D/D_{\text{ave}}$ ) with log-normal distributions for  $D_{\text{max}}$  or  $D_{\text{ave}}$ .

Youngs et al. [A-2] and Moss and Ross [A-9] derived slip distributions for normal and thrust mechanisms, respectively, although only for the normalized relationship ( $D/D_{\text{ave}}$ ) and normalized by maximum slip ( $D/D_{\text{max}}$ ). Takao et al. [A-10] also derived relationships for all types of earthquake mechanism in Japan for the normalized relationship with maximum and average slip. They used a beta distribution for the maximum displacement scaling, which is bound between 0 and 1. The beta distribution has the form [A-2]:

$$F(y) = \frac{\Gamma(a+b)}{\Gamma(a)\Gamma(b)} \int_0^y z^{a-1} (1-z)^{b-1} dz \quad (\text{A-4})$$

where

- $\Gamma(\cdot)$  is the gamma function;
- $F(y)$  is the cumulative probability that variable  $Y$  is less than or equal to a specific value  $y$ ;
- $y$  is equal to  $D/D_{\text{max}}$ ;

and  $a$  and  $b$  are the gamma shape parameters and are functions of  $l/L$ . The parameters  $a$  and  $b$  for normal fault displacements derived by Youngs et al. [A-2] are:

$$\begin{aligned} a &= \exp\left(-0.705 + 1.138 \frac{l}{L}\right) \\ b &= \exp\left(0.421 - 0.257 \frac{l}{L}\right) \\ \text{for } 0 \leq \frac{l}{L} \leq 0.5 \end{aligned} \quad (\text{A-5})$$

The parameters  $a$  and  $b$  for reverse fault displacements derived by Moss and Ross [A-9] are:

$$\begin{aligned} a &= 0.713 + 0.901 \frac{l}{L} \\ b &= 1.74 - 1.86 \frac{l}{L} \\ \text{for } 0 \leq \frac{l}{L} \leq 0.5 \end{aligned} \quad (\text{A-6})$$

The parameters  $a$  and  $b$  for Japanese fault displacements derived by Takao et al. [A-10] are:

$$\begin{aligned} a &= \exp\left(0.70 - 0.87 \frac{l}{L}\right) \\ b &= \exp\left(2.30 - 3.84 \frac{l}{L}\right) \\ \text{for } 0 \leq \frac{l}{L} \leq 0.5 \text{ and } L \geq 10\text{km} \end{aligned} \quad (\text{A-7})$$

For the average displacement scaling, Youngs et al. [A-2], Moss and Ross [A-9] and Takao et al. [A-10] used a gamma distribution. Moss and Ross [A-9] used also a Weibull distribution. The gamma distribution has the form:

$$F(y) = \frac{1}{\Gamma(a)} \int_0^{y/b} e^{-t} t^{a-1} dt \quad (\text{A-8})$$

where

$\Gamma(\cdot)$  is the gamma function;  
 $y$  is equal to  $D/D_{\text{ave}}$ ;

and the parameters  $a$  and  $b$  are functions of  $l/L$ . The parameters  $a$  and  $b$  for normal faults estimated by Youngs et al. [A-2]) are:

$$\begin{aligned} a &= \exp\left(-0.193 + 1.628 \frac{l}{L}\right) \\ b &= \exp\left(0.009 - 0.476 \frac{l}{L}\right) \\ \text{for } 0 \leq \frac{l}{L} \leq 0.5 \end{aligned} \quad (\text{A-9})$$

For reverse faults [A-9]:

$$\begin{aligned} a &= \exp\left(0.574 - 2.29 \frac{l}{L} + 19.9\left(\frac{l}{L}\right)^2 - 30.4\left(\frac{l}{L}\right)^3\right) \\ b &= \exp\left(-1.05 + 6.60 \frac{l}{L} - 34.6\left(\frac{l}{L}\right)^2 + 50.3\left(\frac{l}{L}\right)^3\right) \\ \text{for } 0 &\leq \frac{l}{L} \leq 0.5 \end{aligned} \quad (\text{A-10})$$

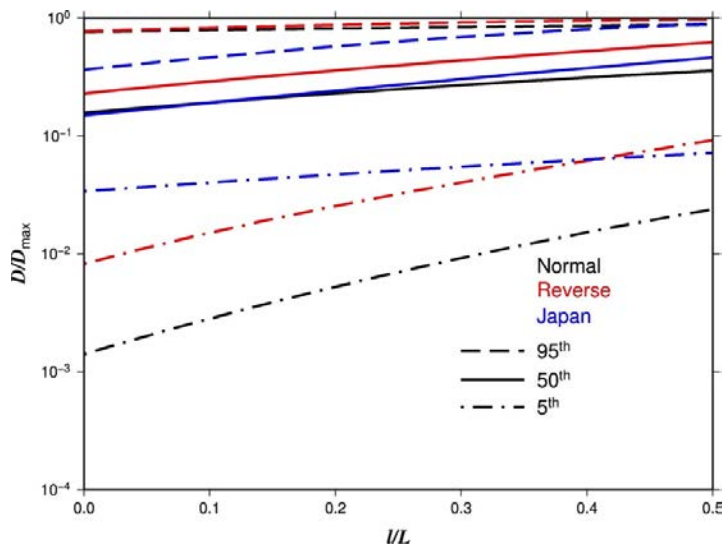
For Japanese faults [10]:

$$\begin{aligned} a &= \exp\left(0.70 + 0.34 \frac{l}{L}\right) \\ b &= \exp\left(-1.40 + 1.82 \frac{l}{L}\right) \\ \text{for } 0 &\leq \frac{l}{L} \leq 0.5 \text{ and } L \geq 10\text{km} \end{aligned} \quad (\text{A-11})$$

Takao et al. [A-10] divided the slip distribution function into two groups according to the length of the fault: more than 10 km and less than 10 km. The relationship between  $l/L$  and displacement are weak when the length is less than 10 km. Figures A-3 and A-4 show the displacement models of the beta and gamma distributions.

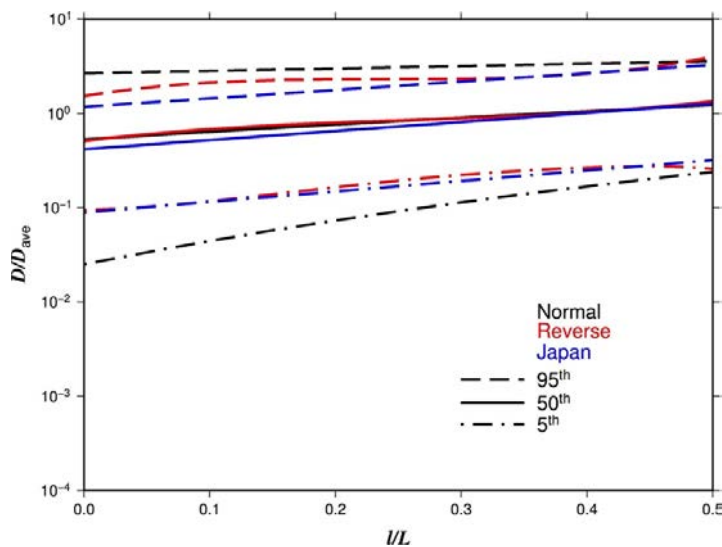
Petersen et al. [A-5] derived several functions for slip along a rupture in the case of strike-slip faulting. They express the average slip at a location as a function of magnitude and the site location relative to the ends of the rupture, and carried out a regression using a log-normal distribution.

For this function, a log-normal distribution is assumed and Petersen et al. [A-5] determined several alternative functional forms, bilinear, quadratic or elliptic. Furthermore, they derived expressions both for displacement as a function of magnitude, and one for normalized displacement, for a total of six possible equations.



**Note:** Black, red and blue lines show the models for normal [A-2], reverse [A-9] and Japanese [A-10] faults, respectively. Dashed, solid and dashed-dotted lines denote 95th, 50th and 5th percentiles, respectively.

FIG. A-3. Models of maximum displacement scaling.



**Note:** Black, red and blue lines show the models for normal [A-2], reverse [A-9] and Japanese [A-10] faults, respectively. Dashed, solid and dashed-dotted lines denote 95th, 50th and 5th percentiles, respectively.

FIG. A-4. Models of average displacement scaling.

In the normalized equations, the assumption is a slip distribution that is tapered at the end but is relative to the average slip ( $D_{\text{ave}}$ ) given by the Wells and Coppersmith [A-14] relationship for strike-slip earthquakes. Petersen et al. [A-5] expressed this term from a regression normalized on the average displacement as:

$$\ln\left(\frac{D}{D_{\text{ave}}}\right) = \frac{8.2525l}{L} - 2.3010 \quad (\text{A-12})$$

for  $\frac{l}{L} < 0.3008$

otherwise:

$$\ln\left(\frac{D}{D_{\text{ave}}}\right) = 0.1816 \quad (\text{A-13})$$

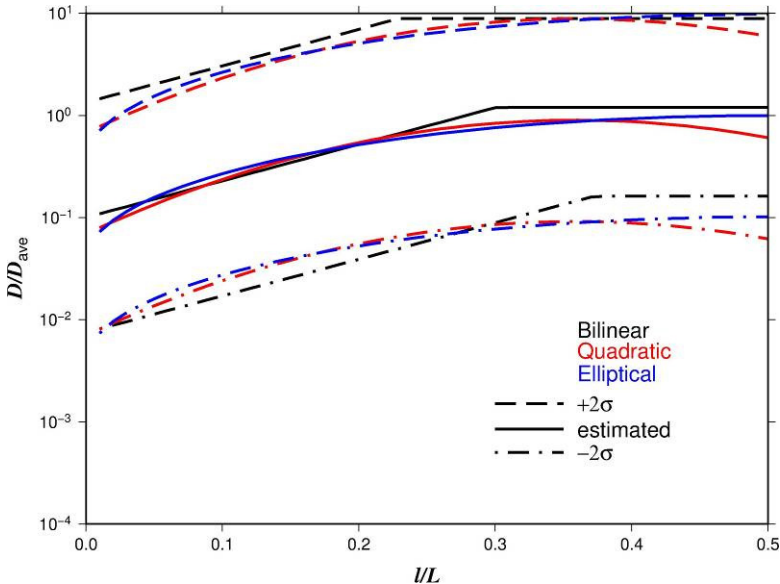
The quadratic and elliptic equations are:

$$\ln\left(\frac{D}{D_{\text{ave}}}\right) = \frac{14.2824l}{L} - 19.8833\left(\frac{l}{L}\right)^2 - 2.6279 \quad (\text{A-14})$$

and

$$\ln\left(\frac{D}{D_{\text{ave}}}\right) = 3.2699\sqrt{1 - 4\left(\frac{l}{L} - 0.5\right)^2} - 3.2749 \quad (\text{A-15})$$

This relationship is plotted in Fig. A-5. There is a considerable difference in slip distribution between the equations, especially close to the centre of the rupture.



**Note:** Black, red and blue solid lines are for the estimated bilinear model, quadratic model and elliptical model, respectively. Dashed and dashed-dotted lines denote  $\pm 2$  standard deviations, respectively.

FIG. A-5. Regression lines and uncertainties ( $\pm 2$  standard deviations) [A-5].

Abrahamson [A-13] adopted a uniform average displacement, from a global regression rather than a distributed slip model, and included the slip variability in an extra term in the sigma. Comparing this to site specific slip variability, he argued that the global model overestimates the variability by over a factor of two (0.17 vs 0.39 in log 10 units) and used this as argument against ergodicity. This conclusion is based on Hecker et al. [A-15], who demonstrated that the aleatory variability in slip from event to event at the same location is much smaller than the variability from global regressions, which emphasizes the importance of using local slip data over global models. However, unless local slip at a site is well constrained, the global relationships and their variability should be used as they include both the slip variability between earthquakes, slip variability between points on the rupture and variability between different faults.

Strom et al. [A-16] presented a similar methodology but unfortunately without specifying the functional form and parameters of their slip relationships. Todorovska and Trifunac [A-17] presented a very different approach to the slip

distribution function, by using an attenuation type equation for displacement and assuming that the slip across the fault is two times the maximum displacement predicted by the attenuation relation. The advantage of this approach is that it follows regular PSHA most closely, but they do not present any comparisons with field data to justify the use of the attenuation relation, which appears to be based on displacements taken from strong motion recordings.

## A-4.2. Distributed faulting

Most studies only consider the probability of surface rupture on the main fault strand, and data for distributed fault displacements are sparser [A-5]. Because distributed faulting is not constrained to singular rupture planes, the distribution functions are given relative to an area. It is expressed that [A-2]:

“...the conditional probability that surface (or near-surface) displacement occurs on a feature at location  $k$  due to an earthquake occurring on some other source. Distributed slip on both minor and major faults adjacent to the principal faulting rupture is presumed to be causally linked to the primary rupture, but the causal mechanism usually is not sufficiently understood, and there may be multiple mechanisms at work.”

Youngs et al. [A-2], Petersen et al. [A-5] and Takao et al. [A-10] “have taken an empirical approach to define this probability function, using data from historical ruptures” [A-2].

### A-4.2.1. Probability of surface rupture

As described in Ref. [A-2], the distributed fault data:

“...were digitized by constructing a raster scan of each map using a 0.5-km  $\times$  0.5-km pixel size. The number of pixels containing distributed faulting divided by the total number of pixels within the faulting area gives a measure of rate of occurrence of distributed rupture for each earthquake. The logistic regression model was used to compute the conditional probability of distributed rupture occurring at a point:

$$P(\text{distributed surface rupture}) = \frac{e^{f(x)}}{1 + e^{f(x)}} \quad (\text{A-16})$$

Youngs et al. [A-2] derived  $f(x)$  for normal faults as:

$$f(x) = 2.06 + (-4.63 + 0.118m + 0.682h)\ln(r + 3.32) \quad (\text{A-17})$$

where  $m$  is earthquake magnitude,  $r$  is the distance to the principal rupture (km), and  $h$  is an indicator variable taking the value of 1 for the hanging wall side of the rupture and 0 for the footwall side of the rupture.

For Japanese faults [A-10]:

$$f(x) = -3.839 + (-3.886 + 0.350m)\ln(r + 0.200) \quad (\text{A-18})$$

Figures A-6 and A-7 represent the probability of surface rupture for magnitude 5.5, 6.5 and 7.5.

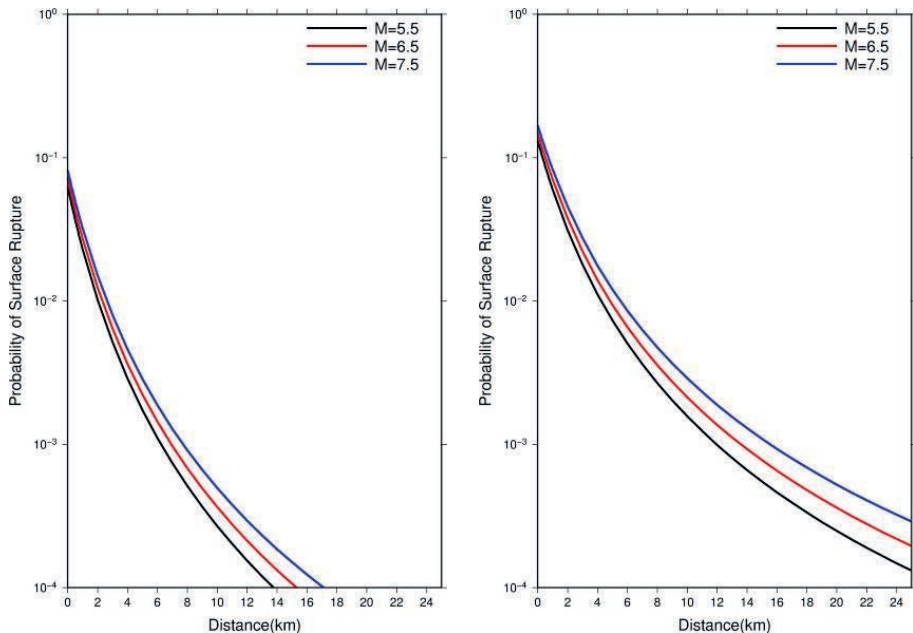


*FIG. A-6. Conditional probability of slip for distributed normal faulting colour coded by magnitude 5.5, 6.5 and 7.5 [A-2]: (left) foot wall; (right) hanging wall.*

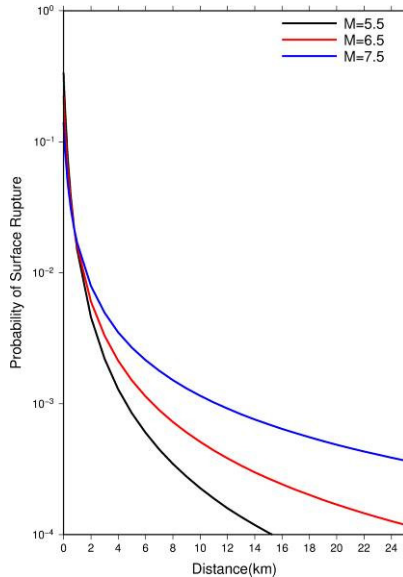


*FIG. A-7. Conditional probability of slip for distributed Japanese faulting colour coded by magnitude 5.5, 6.5 and 7.5 [A-10].*

Petersen et al. [A-5] examined the probability of ground rupture off the principal fault in areas of  $25\text{ m} \times 25\text{ m}$ ,  $50\text{ m} \times 50\text{ m}$ ,  $75\text{ m} \times 75\text{ m}$ ,  $100\text{ m} \times 100\text{ m}$ , and  $200\text{ m} \times 200\text{ m}$  (see Fig. A-8). The probability function for distributed faulting is given as:

$$\ln(P) = a(z)\ln(r) + b(z) \quad (\text{A-19})$$

where

- $a$  and  $b$  are parameters that depend on the area;
- $r$  is distance from the principal fault;
- $z$  is cell size of the area considered for calculating the probability of fault rupture;

and (see Fig. A-8):

- $a(200) = -1.1538$  and  $b(200) = 4.2342$  for  $200\text{ m}$  cells;
- $a(100) = -1.0114$  and  $b(100) = 2.5572$  for  $100\text{ m}$  cells;
- $a(25) = -1.147$  and  $b(25) = 2.1046$  for  $25\text{ m}$  cells.

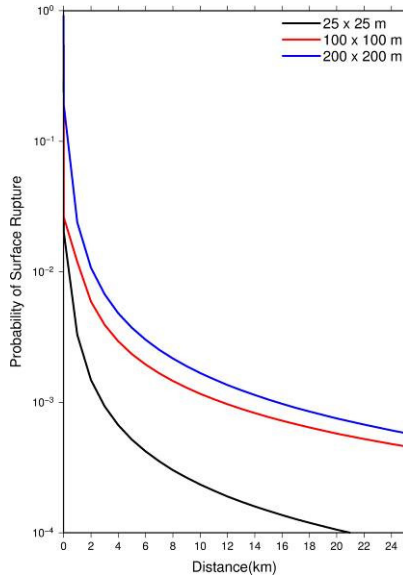


FIG. A-8. Probability of distributed-fault rupture displacement with regression equation colour coded by bins for 200 m × 200 m cells, 100 m × 100 m cells and 25 m × 25 m cells [A-5].

#### A-4.2.2. Probability of slip exceedance

As stated in Ref. [A-2]:

“Unlike principal faulting, there are very limited data for the amount of slip that occurs on the secondary features that move during distributed faulting. Typically, the principal rupture is mapped and described in much greater detail than the distributed ruptures, which are more numerous and widely dispersed, yet smaller in size, and unlikely to be preserved for older events.”

Displacement values of the distributed faults ( $D_{\text{distributed}}$ ) are normalized by the average displacement of the principal faults ( $AD_{\text{principal}}$ ) or the maximum displacement of the principal fault ( $MD_{\text{principal}}$ ). The distribution for  $D_{\text{distributed}}/MD_{\text{principal}}$  or  $D_{\text{distributed}}/AD_{\text{principal}}$  is defined by specifying a probability distribution form. The conditional probability of slip exceedance of distributed faults is then obtained by convolving the resulting gamma distribution for  $D_{\text{distributed}}/MD_{\text{principal}}$ , with a distribution for  $MD_{\text{principal}}$  of  $AD_{\text{principal}}$  in the same manner as was done for principal faulting [A-2].

The beta distribution is used for  $D_{\text{distributed}}/AD_{\text{principal}}$ . For normal faults, Youngs et al. [A-2] derived a power function as:

$$\frac{D_{\text{distributed}}(\text{hanging wall})}{MD_{\text{principal}}} = 0.35e^{-0.091r} \quad (\text{A-20})$$

$$\frac{D_{\text{distributed}}(\text{foot wall})}{MD_{\text{principal}}} = 0.16e^{-0.137r}$$

For Japanese faults, Takao et al. [A-10] derived a power function as:

$$\frac{D_{\text{distributed}}}{MD_{\text{principal}}} = 0.55e^{-0.17r} \quad (\text{A-21})$$

$$\frac{D_{\text{distributed}}}{AD_{\text{principal}}} = 1.9e^{-0.17r}$$

where  $r$  is the distance to the principal rupture (km). For strike-slip faults, Petersen et al. [A-5] derived the form as:

$$\ln\left(\frac{D_{\text{distributed}}}{AD_{\text{principal}}}\right) = -0.1826\ln(r) - 1.5471 \quad (\text{A-22})$$

where  $r$  is the distance to the principal rupture (m). Figures A-9 to A-12 represent the relationship between distance from principal fault and displacement of the distributed fault normalized by the maximum or average displacement of the principal fault.

## A-5. NUMERICAL SIMULATION

As described in the previous section, the relationship between evaluation of fault structure and surface displacement is not well enough understood. The data on displacement distribution and slip amount of distributed faults are very sparse. Numerical simulations help to understand the phenomena of the surface displacement, including distributed faults. One approach, which has not been investigated in detail, is to perform quasidynamic rupture modelling using suitable

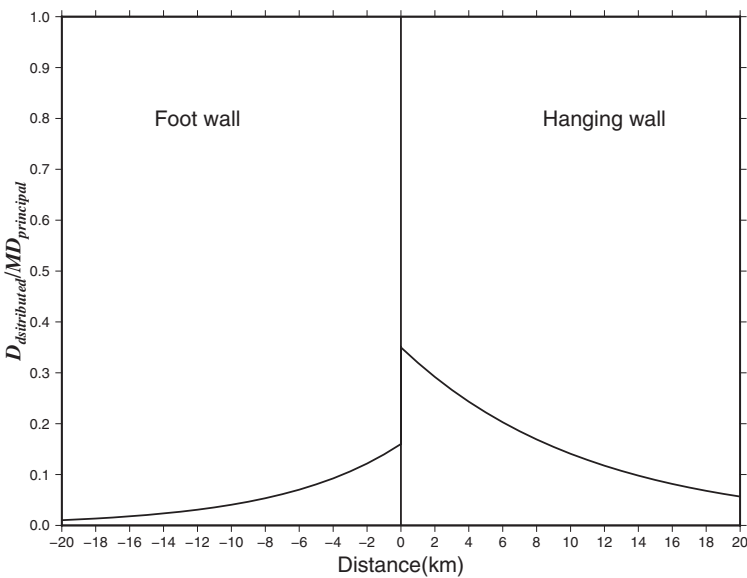


FIG. A-9. Relationship between distance from principal fault and the displacement normalized by the maximum displacement of the principal fault for normal faults [A-2].

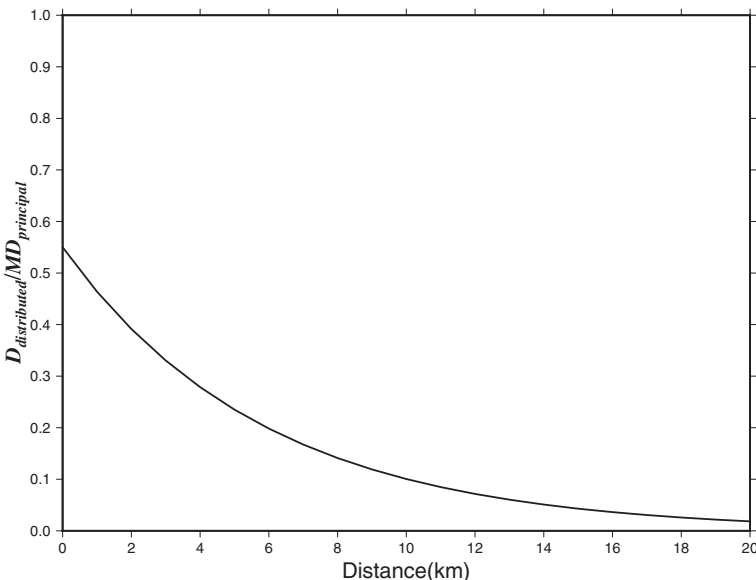


FIG. A-10. Relationship between distance from principal fault and displacement of distributed faulting normalized by the maximum displacements of the principal fault for Japanese faults [A-10].

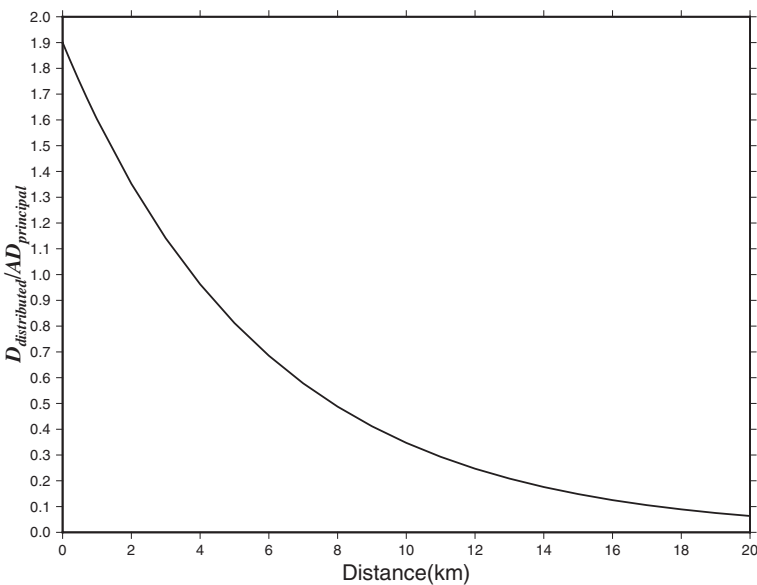


FIG. A-11. Relationship between distance from principal fault and displacement of distributed fault normalized by the average displacement of the principal fault for Japanese faults [A-10].

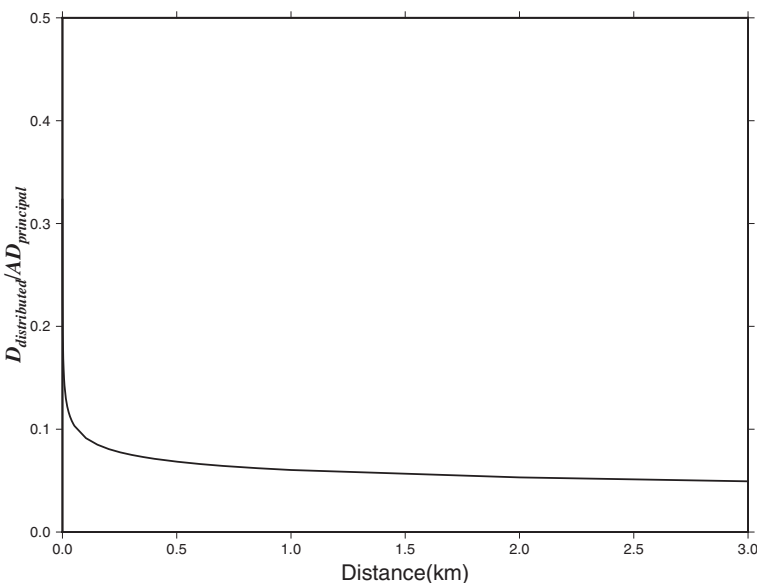


FIG. A-12. Relationship between distance from principal fault and displacement of the distributed faults normalized by the average displacement of the principal fault for strike-slip faults [A-5].

constitutive relationships for the shallow geology.<sup>1</sup> Aochi and Ando [A–18] reviewed the recent researches of numerical simulations on faulting. Dynamic rupture has also been studied especially for the effect on the fault geometry evolution or due to the existed fault structure (see Refs [A–19 to A–21]).

Another approach is to represent the shallow soil or rock behaviour using a continuum model or by a model consisting of small elements with properties constrained by data. Hori [A–22] introduced:

“...continuum modelling and granule material modelling as physical models of faulting. The resulting mathematical problems are difficult and sometimes do not have a unique solution even though the problems are posed for physical phenomena of faulting processes. This is the primary reason for the difficulty of faulting simulations using this approach.”

The simulation of strike-slip faults requires higher computational costs than that for normal or reverse faults because the strike-slip fault simulation should be performed as a 3-D model. The element size is important because it affects the results and computational cost. Two methods can be described: continuum and granule material modelling.

- (1) Continuum modelling: Several computer codes have been validated by carefully comparing their results with laboratory experiment results. The computational cost is lower than for granule material modelling. The model can include physical properties derived from laboratory experiments. However, this approach cannot deal with large displacements and discontinuous phenomena.
- (2) Granule material modelling: This approach can deal with large displacements and discontinuous phenomena. The physical parameters of this method are usually simple: the physical and mechanical parameters of the particles. However, the computational costs are high even for a 2-D simulation, the accuracy is lower than that of the continuum modelling, and it is difficult to define discrete element method (DEM) parameters from soil property parameters.

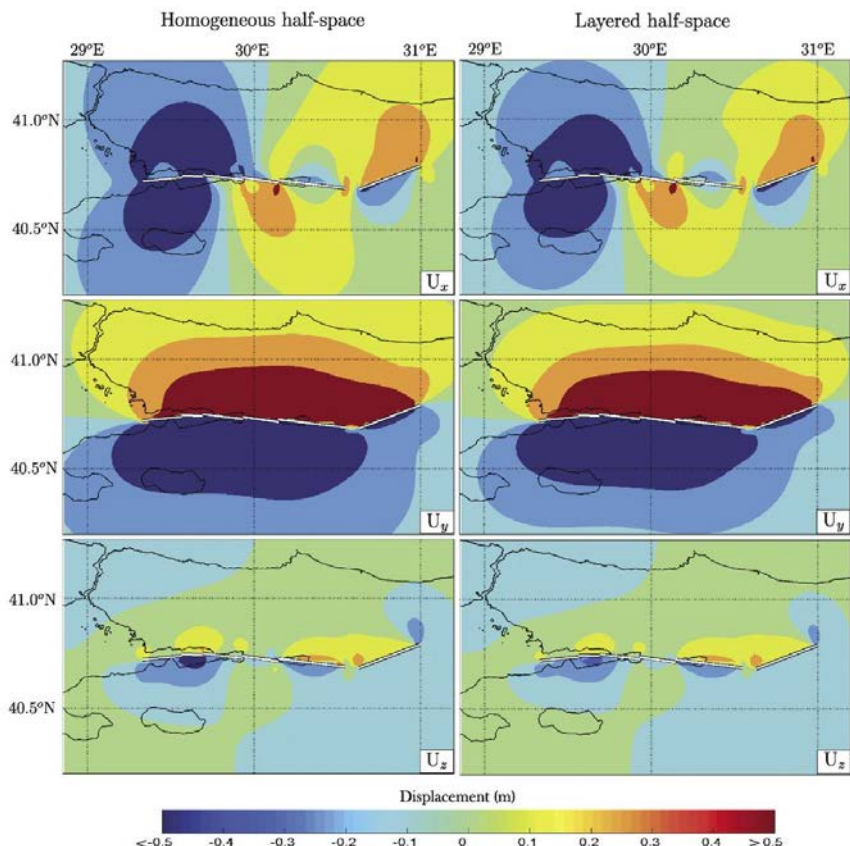
### A–5.1. Continuum modelling

Dislocation modelling requires lower computational costs than continuum modelling. The analytical solution of the dislocation theory was solved

---

<sup>1</sup> See [http://qdyn.googlecode.com/svn-history/r140/trunk/doc/QDYN\\_man.pdf](http://qdyn.googlecode.com/svn-history/r140/trunk/doc/QDYN_man.pdf).

by Mansinha and Smylie [A–23] and Okada [A–24]. The input parameters are fault model and material properties. This method is applied for simulating in a homogeneous medium the crustal movement measured by GPS or interferometric synthetic aperture radar (InSAR) data. This modelling cannot deal with complex initial conditions. Wang et al. [A–25] developed a dislocation computer code that deals with horizontally inhomogeneous models (see Fig. A–13).

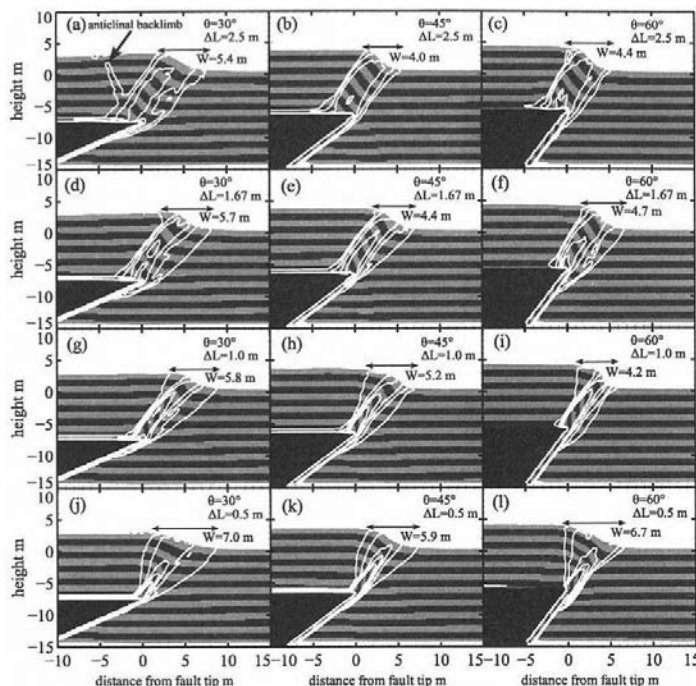


**Note:** The earthquake has an E–W trending fault and consists of six segments whose parameters are adopted from Ref. [A–26]. The homogeneous half-space model has the same elasticity parameters as the uppermost layer of the stratified model. The seismological convention for displacement components is used: that is,  $x$  is positive northwards,  $y$  is positive eastwards and  $z$  is positive downwards.

*FIG. A–13. Surface displacements (m) induced by 17 August 1999, Izmit earthquake, Turkey, computed using a numerical Green's function method (reproduced from Ref. [A–25] with permission).*

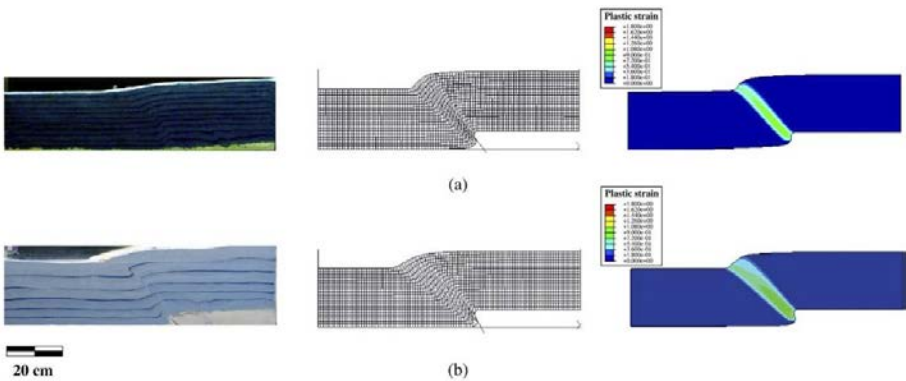
Finite difference methods (FDM) and finite element methods (FEM) are applied for the simulation of large fault displacement processes of complex visco-elastoplastic materials with strong lateral variations of physical properties and in the absence of constant predefined material interfaces. There are many computer codes that have been carefully validated by comparison with laboratory experiments in geotechnical engineering problems.

Ando and Yamazaki [A-27] performed the simulation of a 2-D reverse fault based on a constrained interpolation profile (CIP) method (a type of FDM). Their results indicated that fault related flexure is generated when shear-zone migration occurs in sand (see Fig. A-14).



**Note:** The white contour lines denote the shear strain on the layer. The values of the contour lines are 0.1, 0.25, 0.5, 0.75 and 1.0.  $W$  represents flexure width;  $\theta$  and  $\Delta L$  denote fault dip and fault displacement, respectively. (a)  $\theta = 30^\circ$  and  $\Delta L = 2.5$  m. (b)  $\theta = 45^\circ$  and  $\Delta L = 2.5$  m. (c)  $\theta = 60^\circ$  and  $\Delta L = 2.5$  m. (d)  $\theta = 30^\circ$  and  $\Delta L = 1.67$  m. (e)  $\theta = 45^\circ$  and  $\Delta L = 1.67$  m. (f)  $\theta = 60^\circ$  and  $\Delta L = 1.67$  m. (g)  $\theta = 30^\circ$  and  $\Delta L = 1.0$  m. (h)  $\theta = 45^\circ$  and  $\Delta L = 1.0$  m. (i)  $\theta = 60^\circ$  and  $\Delta L = 1.0$  m. (j)  $\theta = 30^\circ$  and  $\Delta L = 0.5$  m. (k)  $\theta = 45^\circ$  and  $\Delta L = 0.5$  m. (l)  $\theta = 60^\circ$  and  $\Delta L = 0.5$  m.

FIG. A-14. Influence of the fault angle and the unit displacement on the configuration of the fault related flexure (reproduced from Ref. [A-27] with permission).



**Note:** The contour in the right figures shows the magnitude of the plastic strain. The dark colour area has no plastic strain. The soil within the light colour zones has failed and thus experiences plastic strain. Therefore, the light colour zone represents the fault zone within the overburden soil. (a) Fault dip angle 60°. (b) Fault dip angle 50°.

FIG. A-15. Comparison of the fault generated by small scale physical (left) and numerical (centre and right) models (reproduced from Ref. [A-28] with permission).

In the study by Lin et al. [A-28] (see Fig. A-15), the processes of thrust faulting within overburden soil was explored, and they examined the influences of corresponding factors or parameters under a range of boundary conditions using physical models and numerical analysis for both small scale and full scale configurations.

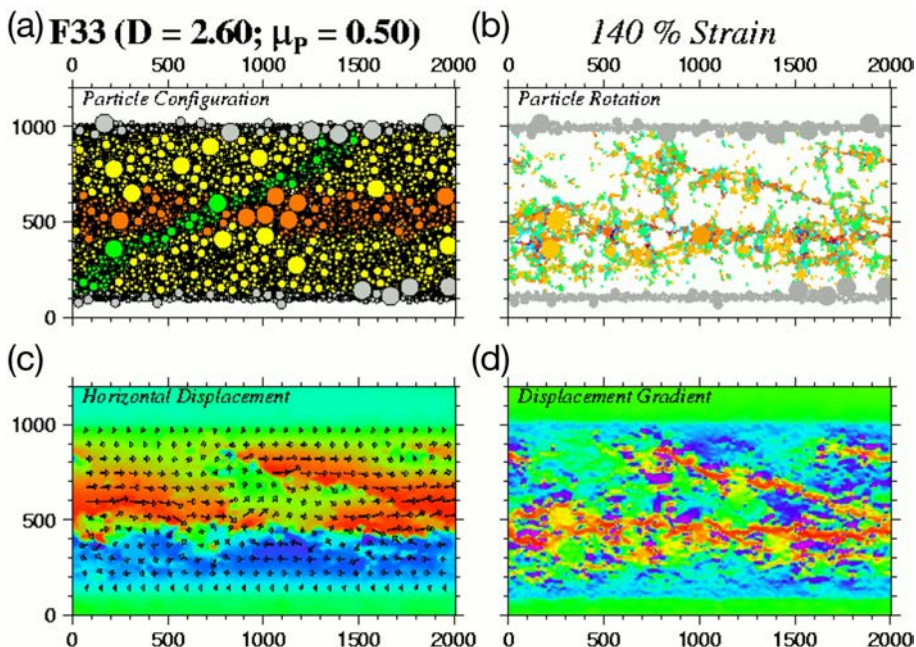
Sawada and Ueta [A-29] performed a strike-slip fault simulation with FEM. The result reproduced en echelon cracks, named Riedel shears, which were observed on the ground surface over strike-slip faults. The inhomogeneous model with a variability of about 20% in physical properties reproduced secondary cracks like Riedel shears and their associated 3-D structure.

### A-5.2. Granule material modelling

Granule material modelling can solve large deformation problem with simple modelling elements. A discrete element method (DEM), also called a distinct element method, is a numerical method for calculating the motion and effect of a large number of small particles. The parameters of DEM consist of physical parameters (particle size and shape) and mechanical interaction parameters between particles (contact friction and normal contact stiffness). However, it is difficult to determine the DEM parameters from soil properties. The parameters of DEM are determined by comparison of DEM and geotechnical laboratory experiments, such as uniaxial tests and triaxial tests.

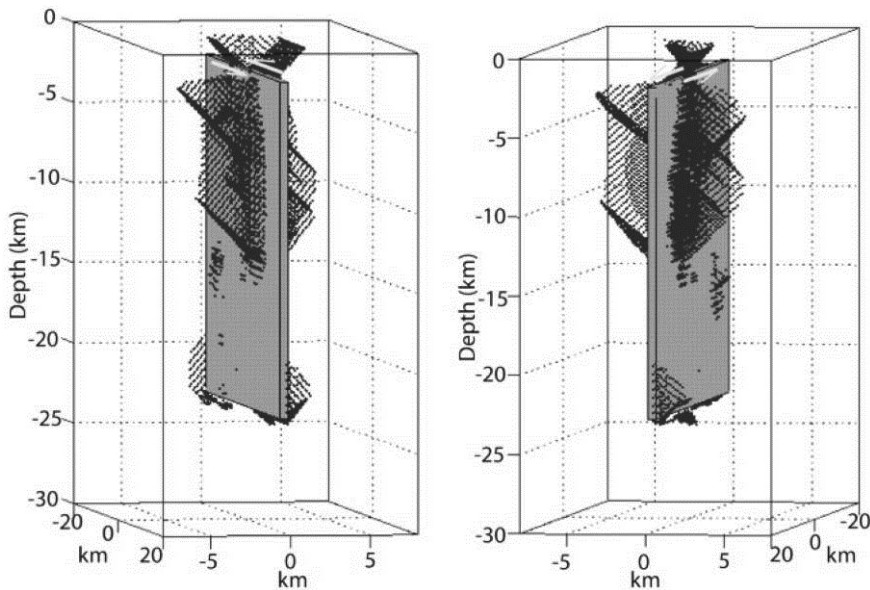
Morgan [A-30] and Morgan and Boettcher [A-31] carried out 2-D DEM simulation “to examine the influences of particle size distribution and interparticle friction on the nature of deformation in granular fault gouge”[A-30]:

“The simulated slip surfaces within the shear zone correspond in orientation and sense of shear to deformation structures observed in natural and experimental gouge zones in particular, Reidel shears ( $R_1$ ,  $R_2$ ) and Y-shears” [A-32] (see Fig. A-16).



**Note:** (a) Particle configuration — particles in walls are fixed relative to each other; upper wall is translated to the right; coloured particles within the shear zone are strain markers. (b) Particle rotations define oblique and fault parallel slip surfaces. (c) Horizontal displacements relative to homogeneous shear induced by wall displacement. (d) Gradient of horizontal displacements defines discontinuities or slip surfaces — low angle and oblique slip planes represent Y and R surfaces, respectively.

FIG. A-16. Snapshot of deforming assemblage,  $D$  (2-D power law exponent) = 2.60,  $\mu_i$  (interparticle friction) = 0.50, at 140% strain (100 plotted units = 1 mm) [A-32].



**Note:** The grey surface represents the shear crack on the pre-existing fault, and the dashed lines represent the tensile cracks.

*FIG. A-17. Two perspectives of the final stage of crack evolution for the 2000 Tottori earthquake dynamic simulation [A-35].*

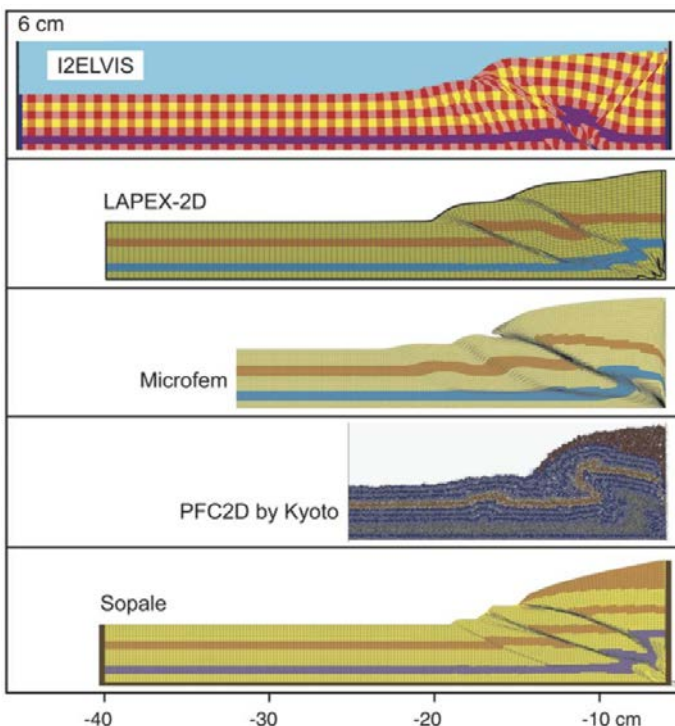
Saomoto et al. [A-33] performed 3-D DEM simulation of a strike-slip fault, clearly producing a shear band considered to be a Riedel shear band at the ground surface. Dalguer et al. [A-34] applied the 3-D DEM to simulate rupture propagation (see Fig. A-17) and showed that cracks develop a flower-like structure surrounding the pre-existing fault.

#### A-6. CONCLUDING REMARKS

Recent developments in PFDHA provide a framework for the evaluation of displacement hazard consistent with PSHA. The most significant difference between the various methods is the quantification of the surface slip distribution as a function of magnitude and location along the rupture. The variability in this function is large, and recent studies suggest that the most important factor in reducing this uncertainty is the use of actual slip data from the site [A-36 to A-40]. It appears that in such cases, when there is ample geological data from the site, a direct probabilistic method might be preferable to the more

frequently used earthquake method, but the sensitivity to epistemic uncertainties in this case needs to be fully explored.

The high performance computing environment has improved the performance of numerical simulations for fault displacement problems. The physical parameters of the subsurface materials based on laboratory experiments are required to validate the results of the numerical simulation and to determine input data for simulations. The comparison of resulting numerical simulations is also important. Buiter et al. [A-41] compared the results of several numerical tools (FEM and DEM) in sandbox type experiments. The results indicated that “numerical models using different solution techniques can to first order successfully reproduce structures observed in analogue sandbox experiments” [A-41] (see Fig. A-18).



**Note:** All quantities (including strain rates) are scaled down to the sandbox scale. Geometries after 6 cm. The grid of Abaqus/Standard is the calculation grid, while for LAPEX-2D, Microfem and Sopale the shown grid is (a subset of) the tracking grid.

FIG. A-18. Results for the shortening experiment (reproduced from Ref. [A-41] with permission).

## REFERENCES

- [A-1] INTERNATIONAL ATOMIC ENERGY AGENCY, Seismic Hazards in Site Evaluation for Nuclear Installations, IAEA Safety Standards Series No. SSG-9, IAEA, Vienna (2010).
- [A-2] YOUNGS, R.R., et al., A methodology for probabilistic fault displacement hazard analysis (PFDHA), *Earthq. Spectra* **19** (2003) 191.
- [A-3] LIU, A., CHEN, K., WU, J., State of art of seismic design and seismic hazard analysis for oil and gas pipeline system, *Earthq. Sci.* **23** (2010) 259–263.
- [A-4] HOFMANN, R.B., Probabilistic Fault Displacement and Seismic Hazard Analysis Literature Assessment, CNWRA 91-013, Centre for Nuclear Waste Regulatory Analyses, San Antonio, TX (1991).
- [A-5] PETERSEN, M.D., et al., Fault displacement hazard for strike-slip faults, *Bull. Seism. Soc. Am.* **101** (2011) 805–825.
- [A-6] COPPERSMITH, K.J., YOUNGS, R.R., Data needs for probabilistic fault displacement hazard analysis, *J. Geodyn.* **29** (2000) 329–343.
- [A-7] ANGELL, M., HANSON, K., SWAN, F., YOUNGS, R., ABRAMSON, H., “Probabilistic fault displacement hazard assessment for flowlines and export pipelines, Mad Dog and Atlantis field developments, deepwater Gulf of Mexico” (Offshore Technology Conf. Houston, 2003).
- [A-8] BRAUN, J.B., Probabilistic Fault Displacement Hazards of the Wasatch Fault, Utah, MSc Thesis, Univ. Utah (2000).
- [A-9] MOSS, R.E.S., ROSS, Z.E., Probabilistic fault displacement hazard analysis for reverse faults, *Bull. Seism. Soc. Am.* **101** (2011) 1542–1553.
- [A-10] TAKAO, M., TSUCHIYAMA, J., ANNAKA, T., KURITA, T., Application of probabilistic fault displacement hazard analysis in Japan, *J. Jpn. Assoc. Earthq. Eng.* **13** (2013) 17–32 (in Japanese).
- [A-11] CHEN, R., PETERSEN, M.D., Probabilistic fault displacement hazards for the Southern San Andreas Fault using scenarios and empirical slips, *Earthq. Spectra* **27** (2011) 293–313.
- [A-12] WELLS, D.L., COPPERSMITH, K.J., Likelihood of surface rupture as a function of magnitude, *Seism. Res. Lett.* **64** (1993) 54.
- [A-13] ABRAHAMSON, N., “Appendix C: Probabilistic fault rupture hazard analysis: San Francisco PUC”, General Seismic Requirements for the Design on New Facilities and Upgrade of Existing Facilities, San Francisco Public Utilities Commission, San Francisco, CA (2008) 1–7.
- [A-14] WELLS, D.L., COPPERSMITH, K.J., New empirical relationships among magnitude, rupture length, rupture width, rupture area, and surface displacement, *Bull. Seism. Soc. Am.* **84** (1994) 974–1002.
- [A-15] HECKER, S., ABRAHAMSON, N.A., WOODDELL, K., Variability of Displacement at a Point: Implications for Earthquake-Size Distribution and Rupture Hazard on Faults, *Bull. Seism. Soc. Am.* **103** (2013) 651–674.

- [A-16] STROM, A., IVASCHENKO, A., KOZHURIN, A., Assessment of the design displacement values at seismic fault crossings and of their excess probability, *J. Mt. Sci.* **8** (2011) 228–233.
- [A-17] TODOROVSKA, M., TRIFUNAC, M.D., “A note on probabilistic assessment of fault displacement hazard”, 100th Anniversary Earthquake Conference (Proc. 8th National Conf. Earthquake Engineering, San Francisco, 2006), Earthquake Engineering Research Institute, Oakland, CA (2006) Paper No. 8NCEE-001793.
- [A-18] AOCHI, H., ANDO, R., Numerical simulation on faulting: Microscopic evolution, macroscopic interaction and rupture process of earthquakes, *J. Seismol. Soc. Jpn.* **61** (2009) S403-S413 (in Japanese).
- [A-19] ANDO, R., YAMASHITA, T., Effects of mesoscopic-scale fault structure on dynamic earthquake ruptures: Dynamic formation of geometrical complexity of earthquake faults, *J. Geophys. Res.* **112** (2007) 1–15.
- [A-20] HARRIS, R.A., DAY, S.M., Dynamic 3D simulations of earthquakes on En Echelon Faults, *Geophys. Res. Lett.* **26** (1999) 2089–2092.
- [A-21] KAME, N., YAMASHITA, T., Dynamic branching, arresting of rupture and the seismic wave radiation in self-chosen crack path modeling, *Geophys. J. Int.* **155** (2003) 1042–1050.
- [A-22] HORI, M., Numerical simulation of faulting and fault-induced ground deformation, *Act. Fault Res.* **28** (2008) 65–70 (in Japanese).
- [A-23] MANSINHA, L., SMYLIE, D.E., The displacement fields of inclined faults, *Bull. Seism. Soc. Am.* **61** (1971) 1433–1440.
- [A-24] OKADA, Y., Surface deformation due to shear and tensile faults in a half-space, *Bull. Seism. Soc. Am.* **75** (1985) 1135–1154.
- [A-25] WANG, R., MARTÍN, F.L., ROTH, F., Computation of deformation induced by earthquakes in a multi-layered elastic crust-FORTRAN programs EDGRN/EDCMP, *Comput. Geosci.* **29** (2003) 195–207.
- [A-26] WRIGHT, T., FIELDING, E., PARSONS, B., Triggered slip: Observations of the 17 August 1999 Izmit (Turkey) earthquake using radar interferometry, *Geophys. Res. Lett.* **28** (2001) 1079–1082.
- [A-27] ANDO, K., YAMAZAKI, H., Evolving simulation of fault-related flexure using CIP-Method which makes consideration of dilatancy, *J. Seism. Soc. Jpn.* **65** (2012) 135–149 (in Japanese).
- [A-28] LIN, M.L., CHUNG, C.F., JENG, F.S., Deformation of overburden soil induced by thrust fault slip, *Eng. Geol.* **88** (2006) 70–89.
- [A-29] SAWADA, M., UETA, K., Numerical simulation for evaluation of fracture zone distribution due to strike-slip faulting, CRIEPI Report N08028 (2009) 19 (in Japanese).
- [A-30] MORGAN, J.K., Numerical simulations of granular shear zones using the distinct element method: II. The effect of particle size distribution and interparticle friction on mechanical behavior, *J. Geophys. Res. B.* **104** (1999) 2721–2732.
- [A-31] MORGAN, J.K., BOETTCHER, M.S., Numerical simulations of granular shear zones using the distinct element method: I. Shear zone kinematics and micromechanics of localization, *J. Geophys. Res. B.* **104** (1999) 2703–2719.

- [A-32] MORGAN, J.K., “Distinct element simulations of granular shear zones: Micromechanics of localization and frictional behavior”, 2nd ACES Workshop Proceedings (MATSU’URA, M., NAKAJIMA, K., MORA, P., Eds), APEC Cooperation for Earthquake Simulation, Brisbane (2001) 83–90.
- [A-33] SAOMOTO, H., YOSHIMI, M., KUNIMATSU, S., Discrete element simulation of shear band evolution caused by strike slip faulting, JSCE J. Earthq. Eng. **28** (2005) 179 (in Japanese).
- [A-34] DALGUER, L.A., IRIKURA, K., RIERA, J.D., Simulation of tensile crack generation by three-dimensional dynamic shear rupture propagation during an earthquake, J. Geophys. Res. **108** (2003).
- [A-35] DALGUER, L.A., IRIKURA, K., RIERA, J.D., Generation of new cracks accompanied by the dynamic shear rupture propagation of the 2000 Tottori (Japan) earthquake, Bull. Seism. Soc. Am. **93** (2003) 2236–2252.
- [A-36] ELLIS, S., SCHREURS, G., PANIEN, M., Comparisons between analogue and numerical models of thrust wedge development, J. Struct. Geol. **26** (2004) 1659–1675.
- [A-37] FULLSACK, P., An arbitrary Lagrangian-Eulerian formulation for creeping flows and its application in tectonic models, Geophys. J. Int. **120** (1995) 1–23.
- [A-38] GERYA, T.V., YUEN, D.A., Characteristics-based marker-in-cell method with conservative finite-difference schemes for modelling geological flows with strongly variable transport properties, Phys. Earth Planet. Inter. **140** (2003) 293–318.
- [A-39] BABEYKO, A.YU., SOBOLEV, S.V., TRUMBULL, R.B., ONCKEN, O., LAVIER, L.L., Numerical models of crustal scale convection and partial melting beneath the Altiplano-Puna plateau, Earth Planet. Sci. Lett. **199** (2002) 373–388.
- [A-40] ITASCA, PFC2D: Particle Flow Code in 2 Dimensions, User’s Guide Version 3.0, Itasca Consulting Group, Inc., Minneapolis, MN (1999).
- [A-41] BUITER, S.J.H., et al., “The numerical sandbox: Comparison of model results for a shortening and an extension experiment”, Analogue and Numerical Modelling of Crustal-Scale Processes (BUITER, S.J.H., SCHREURS, G., Eds), Geological Society Special Publication No. 253, The Geological Society, London (2006) 29–64.



## **CONTRIBUTORS TO DRAFTING AND REVIEW**

Berge-Thierry, C.	French Alternative Energies and Atomic Energy Commission, France
Biro, Y.	Swissnuclear, Switzerland
Cabanero, J.S.	Nuclear Safety Council, Spain
Dan, K.	Ohsaki Research Institute, Ltd., Japan
Ebisawa, K.	Central Research Institute of the Electric Power Industry, Japan
Fukushima, Y.	International Atomic Energy Agency
Gülen, L.	Sakarya University, Turkey
Inoue, N.	Geo-Research Institute, Japan
Irikura, K.	Aichi Institute of Technology, Japan
Kameda, H.	Kyoto University, Japan
My Thanh, T.	Institute of Geophysics, Viet Nam
Petersen, M.	United States Geological Service, United States of America
Pitarka, A.	Lawrence Livermore National Laboratory, United States of America
Renault, P.	Swissnuclear, Switzerland
Schmitt, T.	TÜV SÜD, Germany
Seber, D.	Nuclear Regulatory Commission, United States of America
Senfaute, G.	Électricité de France, France
Somerville, P.G.	AECOM, Australia
Thiry, J.M.	AREVA, France

Varpasuo, P.E.J.

PVA Engineering Services, Finland

Wu, C.J.

Nuclear Regulation Authority, Japan

### **Consultants Meetings**

Vienna, Austria: 11–13 July 2012; 13–17 May, 16–20 September 2013

Tokyo, Japan: 12–16 November 2012; 6–11 July 2013



## ORDERING LOCALLY

In the following countries, IAEA priced publications may be purchased from the sources listed below or from major local booksellers.

Orders for unpriced publications should be made directly to the IAEA. The contact details are given at the end of this list.

### BELGIUM

#### *Jean de Lannoy*

Avenue du Roi 202, 1190 Brussels, BELGIUM

Telephone: +32 2 5384 308 • Fax: +32 2 5380 841

Email: [jean.de.lannoy@euronet.be](mailto:jean.de.lannoy@euronet.be) • Web site: <http://www.jean-de-lannoy.be>

### CANADA

#### *Renouf Publishing Co. Ltd.*

22-1010 Polytek Street, Ottawa, ON K1J 9J1, CANADA

Telephone: +1 613 745 2665 • Fax: +1 643 745 7660

Email: [order@renoufbooks.com](mailto:order@renoufbooks.com) • Web site: <http://www.renoufbooks.com>

#### *Bernan Associates*

4501 Forbes Blvd., Suite 200, Lanham, MD 20706-4391, USA

Telephone: +1 800 865 3457 • Fax: +1 800 865 3450

Email: [orders@bernan.com](mailto:orders@bernan.com) • Web site: <http://www.bernan.com>

### CZECH REPUBLIC

#### *Suweco CZ, s.r.o.*

SESTUPNÁ 153/11, 162 00 Prague 6, CZECH REPUBLIC

Telephone: +420 242 459 205 • Fax: +420 284 821 646

Email: [nakup@suweco.cz](mailto:nakup@suweco.cz) • Web site: <http://www.suweco.cz>

### FRANCE

#### *Form-Edit*

5 rue Janssen, PO Box 25, 75921 Paris CEDEX, FRANCE

Telephone: +33 1 42 01 49 49 • Fax: +33 1 42 01 90 90

Email: [fabien.boucard@formedit.fr](mailto:fabien.boucard@formedit.fr) • Web site: <http://www.formedit.fr>

#### *Lavoisier SAS*

14 rue de Provigny, 94236 Cachan CEDEX, FRANCE

Telephone: +33 1 47 40 67 00 • Fax: +33 1 47 40 67 02

Email: [livres@lavoisier.fr](mailto:livres@lavoisier.fr) • Web site: <http://www.lavoisier.fr>

#### *L'Appel du livre*

99 rue de Charonne, 75011 Paris, FRANCE

Telephone: +33 1 43 07 43 43 • Fax: +33 1 43 07 50 80

Email: [livres@appeldulivre.fr](mailto:livres@appeldulivre.fr) • Web site: <http://www.appeldulivre.fr>

### GERMANY

#### *Goethe Buchhandlung Teubig GmbH*

Schweitzer Fachinformationen

Willstätterstrasse 15, 40549 Düsseldorf, GERMANY

Telephone: +49 (0) 211 49 874 015 • Fax: +49 (0) 211 49 874 28

Email: [s.dehaan@schweitzer-online.de](mailto:s.dehaan@schweitzer-online.de) • Web site: <http://www.goethebuch.de>

## **HUNGARY**

### ***Librotrade Ltd., Book Import***

Pesti ut 237. 1173 Budapest, HUNGARY

Telephone: +36 1 254-0-269 • Fax: +36 1 254-0-274

Email: books@librotrade.hu • Web site: <http://www.librotrade.hu>

## **INDIA**

### ***Allied Publishers***

1<sup>st</sup> Floor, Dubash House, 15, J.N. Heredi Marg, Ballard Estate, Mumbai 400001, INDIA

Telephone: +91 22 4212 6930/31/69 • Fax: +91 22 2261 7928

Email: alliedpl@vsnl.com • Web site: <http://www.alliedpublishers.com>

### ***Bookwell***

3/79 Nirankari, Delhi 110009, INDIA

Telephone: +91 11 2760 1283/4536

Email: bkwell@nde.vsnl.net.in • Web site: <http://www.bookwellindia.com>

## **ITALY**

### ***Libreria Scientifica "AEIOU"***

Via Vincenzo Maria Coronelli 6, 20146 Milan, ITALY

Telephone: +39 02 48 95 45 52 • Fax: +39 02 48 95 45 48

Email: info@libreriaaeiou.eu • Web site: <http://www.libreriaaeiou.eu>

## **JAPAN**

### ***Maruzen Co., Ltd.***

1-9-18 Kaigan, Minato-ku, Tokyo 105-0022, JAPAN

Telephone: +81 3 6367 6047 • Fax: +81 3 6367 6160

Email: journal@maruzen.co.jp • Web site: <http://maruzen.co.jp>

## **RUSSIAN FEDERATION**

### ***Scientific and Engineering Centre for Nuclear and Radiation Safety***

107140, Moscow, Malaya Krasnoselskaya st. 2/8, bld. 5, RUSSIAN FEDERATION

Telephone: +7 499 264 00 03 • Fax: +7 499 264 28 59

Email: secnrs@secnrs.ru • Web site: <http://www.secnrs.ru>

## **UNITED KINGDOM**

### ***The Stationery Office Ltd. (TSO)***

St. Crispins House, Duke Street, Norwich, NR3 1PD, UNITED KINGDOM

Telephone: +44 (0) 333 202 5070

Email: customer.services@tso.co.uk • Web site: <http://www.tso.co.uk>

## **UNITED STATES OF AMERICA**

### ***Bernan Associates***

4501 Forbes Blvd., Suite 200, Lanham, MD 20706-4391, USA

Telephone: +1 800 865 3457 • Fax: +1 800 865 3450

Email: orders@bernan.com • Web site: <http://www.bernan.com>

### ***Renouf Publishing Co. Ltd.***

812 Proctor Avenue, Ogdensburg, NY 13669-2205, USA

Telephone: +1 888 551 7470 • Fax: +1 888 551 7471

Email: orders@renoufbooks.com • Web site: <http://www.renoufbooks.com>

## **Orders for both priced and unpriced publications may be addressed directly to:**

IAEA Publishing Section, Marketing and Sales Unit

International Atomic Energy Agency

Vienna International Centre, PO Box 100, 1400 Vienna, Austria

Telephone: +43 1 2600 22529 or 22530 • Fax: +43 1 2600 29302

Email: sales.publications@iaea.org • Web site: <http://www.iaea.org/books>

## **SEISMIC HAZARDS IN SITE EVALUATION FOR NUCLEAR INSTALLATIONS**

### **IAEA Safety Standards Series No. SSG-9**

STI/PUB/1448 (56 pp.; 2010)

ISBN 92-0-102910-2

Price: €29.00

## **FUNDAMENTAL SAFETY PRINCIPLES**

### **IAEA Safety Standards Series No. SF-1**

STI/PUB/1273 (37 pp.; 2006)

ISBN 92-0-110706-4

Price: €25.00

## **SITE EVALUATION FOR NUCLEAR INSTALLATIONS**

### **IAEA Safety Standards Series No. NS-R-3**

STI/PUB/1177 (28 pp.; 2003)

ISBN 92-0-112403-1

Price: €15.00

This publication explains the principles which underlie strong ground motion simulation, describes various methods for simulating the motions and provides some examples using fault rupture modelling. The detailed guidelines and practical tools presented in this Safety Report will be of value to researchers, operating organizations, regulatory bodies, vendors and technical support organizations in the areas of seismic hazard evaluation of nuclear installations. The information provided will also be of great importance for seismic hazard assessments following the Fukushima Daiichi nuclear accident.

INTERNATIONAL ATOMIC ENERGY AGENCY  
VIENNA  
ISBN 978-92-0-102315-5  
ISSN 1020-6450